EMULSIFICATION WITH MICRO-ENGINEERED DEVICES

DISSERTATION

to obtain
the doctor's degree at the University of Twente,
on the authority of the rector magnificus,
prof. dr. W.H.M. Zijm,
on account of the decision of the graduation committee,
to be public defended
on Thursday 9th of November 2006 at 15.00

by

Maik Jörn Geerken

born 24th of May 1974

in Wilhelmshaven, Germany

This dissertation has been approved by:

Promotor:	Prof. Dr.-Ing. M. Wessling
Assistant-promotor:	Dr. Ir. R.G.H. Lammertink

“Man muss die Welt nicht verstehen. Man muss sich darin zurechtfinden.”
Albert Einstein (1879-1955)

Gewidmet meinem Groβvater Otto

This work was partly financially supported by the European Union (Thames Project; QRLT 2000-01228) and by the Dutch government in the framework of the BISK program MicroNed.

Emulsification with micro-engineered devices

Ph.D. Thesis, University of Twente

ISBN: 90-365-2432-6

Cover design by Maik J. Geerken

Printed by Wöhrmann Print Service, Zutphen

Content

Chapter 1

Introduction

1.1 Emulsions

What are emulsions? One simple example is milk. The main components are water, proteins and fat. The fat is dispersed in small droplets surrounded by water and stabilized by proteins. An emulsion is a two-phase system of two non-mixable liquids. In principle, the liquid with the lower mass fraction is divided into small droplets - called dispersed phase- surrounded by the so-called continuous phase. Milk for instance is an example of an oil-in-water emulsion and margarine is a water-in-oil emulsion.
Depending on the droplet size of the dispersed phase, emulsions can be divided into micro and macro emulsions. An emulsion is called macro if the droplet size is higher than 0.1 µm and a micro emulsion contains droplets of less than 300 nm [1]. Macro emulsions are less stable. Three destabilization mechanisms can be observed [2]:

1 Sedimentation and skimming due to density differences between the two phases
2 Droplet aggregation
3 Coalescence of the droplets

Due to this, it is necessary to use additives to improve the stability. To prevent coalescence, emulsifiers (surfactants) are used. Emulsifiers are molecules that adsorb at the oil-water interface and decrease the interfacial tension.
The drop size distribution of an emulsion depends on the process conditions and the used emulsification device. The National Institute of Standards and Technology

(NIST) defines a particle size distribution monodisperse if at least 90 % of particles are lying within 5 % of the median size [3]. To quantify how broad or narrow a drop size distribution is, the coefficient of variation (COV) or the span is given, and both values are commonly used in literature. The COV is the standard deviation of the measured drop sizes divided by the average drop diameter. The standard deviation of a population of values can be assumed to be equal to the inflection point of its distribution if the population exhibits a gaussian distribution. The span is obtained from the cumulative volume distribution shown in Figure 1 and calculated as follows:

$$span = \frac{\left(d_{90} - d_{10}\right)}{d_{50}} \tag{1}$$

In Equation 1 the diameters d_x are corresponding to the diameters which represent x percentage of the cumulative drop volume. Hence, the d_{90} is the diameter that covers 90 % of the dispersed phase drop volume as depicted in Figure 1. The COV and the span value are not equal, because the COV is based on the drop diameter and the span is weighted by the drop volume. But both give an indication of how broad a number of values are distributed.

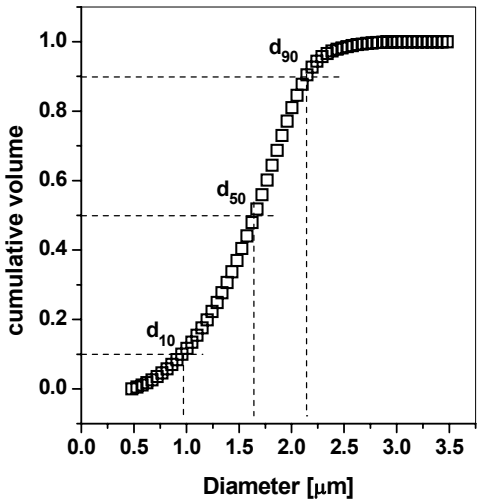

Figure 1: Example of the determination of the span value.

1.2 Emulsifications methods

To produce an emulsion of two immiscible liquids it is necessary to divide one phase into small droplets and stabilize them against coalescence. To disrupt the dispersed phase into droplets, a certain energy input to the system is required. The energy input in the dispersing zone is responsible for the resulting droplet sizes. The stabilization of the disrupted phase depends on how fast the used emulsifiers are able to occupy the newly created interfaces and how well they stabilize them.
Most common devices to produce emulsions are rotor-stator-systems, stirrers and high-pressure homogenizers. New methods, developed in the last decades, are based on single drop formation at micrometer sized pores and channels. Besides membrane emulsification using conventional and commercial available macro porous membranes, most of these techniques are using micro-engineered hole or channel structures.

1.2.1 Conventional methods

In rotor-stator-systems both liquids are flowing through a conical gap between a stator and a rotor usually rotating with a speed varying from 5 to 40 meters per second resulting in retentions times between 0.1 and 1 s [4]. Both surfaces are either smooth or toothed. The gap normally has a width between 100 to 3000 µm. The dispersed phase is disrupted in this gap due to high shear forces and turbulence [1].
In high-pressure homogenizers a premixed emulsions is pumped under high pressure (up to 4000 bar) through a narrow orifice [5] and the dispersed phase is disrupted due to high shear forces and turbulence but cavitation can also occur [6].
All these industrial methods are working with a high-energy input (10^6–10^8 J/m^3) to produce turbulences and shear forces in the dispersing zone [7]. A turbulent flow is coupled with energy dissipation resulting in a temperature increase. For example, in a high-pressure homogenizer about 99 % of the supplied energy is converted to heat [2,8]. To protect temperature sensitive emulsion ingredients like proteins, it is

necessary to cool the dispersing zone. Muschiolik et al. showed that whey proteins could change their physico-chemical properties due to a high pressure treatment [9]. The whey protein β-lactoglobulin for instance looses its emulsifying efficiency due to pressure-induced unfolding resulting in protein aggregation [10]. Emulsions prepared with the above mentioned methods are characterized by a broad drop size distribution.

1.2.2 New emulsification techniques

The droplet break-up mechanism of the to be dispersed phase can be divided into three different types. The first one use shear forces applied by a cross-flowing continuous phase. Drops are sheared off from the bulk of the dispersed phase. This droplet formation process is used in membrane emulsification and T-junction emulsification.

The second drop formation mechanism is called spontaneous drop break-up. Here, the dispersed phase is at first inflated into a disk-like shaped drop due to the geometrical restrictions of the emulsification device while surrounded by the continuous phase. After the drop has reached a certain volume and it is growing out of the restrictions it can form a spherical drop. The spherical shape is more favored than the flat geometry. Therefore, the drop tends to form a spherical shape. It flows out of the geometrical restrictions and detaches. Shear forces are not involved in this type of drop formation. This mechanism is applied in microchannel and straight-through microchannel emulsification.

The third type of emulsification devices makes use of a combination of the shear or drag induced and the spontaneous drop formation process. In literature these devices are called flow-focusing devices. In a flow-focusing device the continuous and the to be dispersed phase are flowing coaxial through a small orifice. The to be dispersed phase is the inner phase and flows with a lower velocity than the outer continuous phase. The drop break-up can occur in the orifice or downstream out of the orifice depending on the total flow rates and the flow ratio of the inner to the outer phase.

Membrane emulsification

Membrane emulsification has been developed in the last 20 years. The basic idea was to use macro porous membranes to generate drops by pressing the dispersed phase through the porous matrix of the membrane towards the continuous phase. At the interface, the dispersed phase forms drops at the pore openings, stabilized by surfactants and detached by the cross-flowing continuous phase. Compared to the mentioned conventional methods, membrane emulsification requires a lower energy input (10^5-10^6 J/m^3) to generate micron-sized drops [7].

Figure 2A shows a schematic representation of the cross-flow emulsification process. The final drop size is a result of the acting forces. The major forces are the drag forces generated by the flowing continuous phase, the interfacial tension force and the buoyancy or gravitational force as depicted in Figure 2B. A drop will be released from the pore if the detachment forces overcome the attachment forces.

The main parameters influencing the drop size, its distribution, and the disperse phase flux can be divided into process parameters (flow velocity of the continuous phase, disperse phase pressure and temperature), membrane parameters (mean pore size, pore size distribution, porosity, thickness and wettability) and the fluid properties (viscosity and dynamic interfacial tension).

The flow velocity of the continuous phase induces a certain wall shear stress at the membrane surface, which has a major influence on the drop size at otherwise constant conditions. Several author found a decreasing drop size with increasing cross-flow velocity [11-17].

The effective pressure difference determines the throughput and therefore, the productivity of the membrane emulsification system. It is determined by the pressure difference between the disperse phase and the continuous phase minus the critical pressure. The critical pressure is the minimum pressure to let the disperse phase permeate through the membrane. With increasing effective pressure the disperse phase flux increases linearly in accordance with Darcy's Law.

The magnitude of the flux depends strongly on the membrane properties [11,18-21]. Table 1 displays some flux data found in literature for different membranes applied for oil-in-water emulsification.

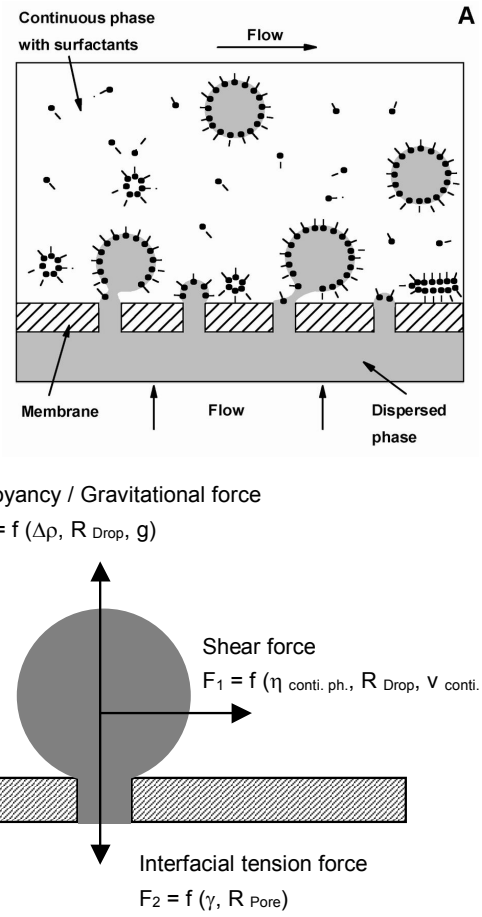

Figure 2: Schematic representation of the cross-flow membrane emulsification process (A) and the major forces acting on a droplet inflated from a pore (B).

Table 1: Dispersed phase fluxes of different membranes used for oil-in-water emulsification.

Type of membrane	Mean pore size [μm]	Δp [bar]	Dispersed phase	Flux [L $h^{-1}m^{-2}bar^{-1}$]	Ref.
Si_xN_y microsieve	7	0.09	hexadecane	21000	[8]
Al_2O_3 membrane	3	3	vegetable oil	367	[22]
SPG membrane	2.5	0.264	rape seed oil	11	[23]
Al_2O_3 membrane	0.8	1.3	vegetable oil	30.8	[18]
SPG membrane	0.57	1.3	corn oil	15.4	[11]
MPG membrane	0.5	2.2	soybean oil	7.6	[9]
Ceramic membrane	0.2	1.4	mineral oil	14	[12]

Van der Graaf et al. reported that the drop size increases at constant emulsifier concentration and constant cross-flow velocity if the pressure difference increases [24]. These observations can be related to the adsorption rate of the emulsifier on a growing droplet. Schröder et al. found that the influence of the dispersed phase pressure becomes less as the emulsifier adsorbs faster [14]. When the fast adsorbing emulsifier SDS is used, the drop diameter is nearly independent from the applied dispersed phase pressure [14,25].

The pore size and its distribution of a given macro porous membrane is one major parameter for the resulting drop size. Depending on the process conditions the mean drop size is linearly related to the mean pore size with a factor varying between 2 and 50 [26,27]. The pore size distribution of a given membrane influences the drop size distribution as well. Vladisavljević et al. investigated the structure and permeability of SPG-membranes. They found that the pore size distributions are reflected in the drop size distributions of emulsions prepared with SPG membranes [28].

A key issue in many studies is the resulting drop size distribution, expressed either by the span or by the coefficient of variation. For SPG membranes the COV varies between 5 and 40 % depending on the process conditions [29]. Kobayashi et al. report that the COV decreases with increasing cross-flow velocity and with

increasing dispersed phase contact angle on the membrane surrounded by the continuous phase [16]. Yasuno et al. found an increasing COV with increasing dispersed phase flow [25].

Most of the studies used conventional polymeric, ceramic or glass membranes. These membranes have a tortuous structure with a thickness ranging from 10 to several hundreds of micrometer, and a broad pore size distribution. Overall, this leads mostly to low dispersed phase fluxes and to broad drop size distributions. These disadvantages might be the reason why membrane emulsification has not found its way into large scale production of emulsions. To overcome these disadvantages, a micro-engineered membrane was adopted from microfiltration [30,31]. This microsieve membrane, fabricated out of silicon nitride with a silicon support, has a precisely defined pore size combined with a micron sized membrane thickness. Furthermore, the porosity can be optimized for emulsification to limit coalescence of neighboring drops. Some studies, emulsifying oil-in-water, already showed that these microsieve membranes have high dispersed phase flux at low pressure differences [8,24].

T-Junctions

Two microchannels are forming a T-junction as depicted in Figure 3 fabricated in PMMA, glass or silicon via micro-engineering tools for the production of monodispersed drops.

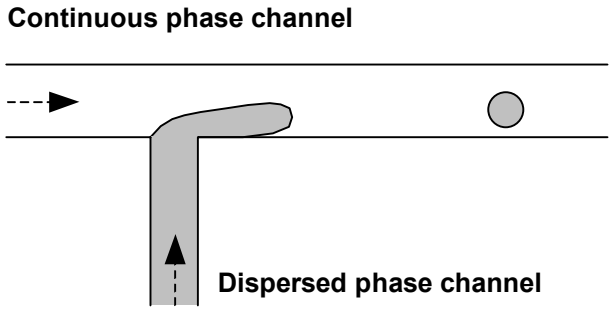

Figure 3: Schematic drawing of a T-junction emulsification device.

The to be dispersed phase flows in a channel which ends at the continuous phase flow channel. Typical dimensions of the channels are lying in the range of 100 μm in width and 10 to 100 μm in depth. The dispersed phase channel is mostly smaller in size than the continuous phase flow channel.

The drop formation process is mostly driven by shear and interfacial tension forces. The shear force generated by the flowing continuous phase tends to detach the forming drop whereas the interfacial tension force tries to keep the drop attached to the dispersed phase channel. Experiments and simulations have shown that the drop size decreases with increasing flow velocity of the continuous phase at constant dispersed phase flow, accounting for the influence of the applied shear forces [32,33]. Whereas the drop size increases with increasing disperse phase flow at constant continuous phase flow [34,35]. Decreasing interfacial tension leads to smaller drop sizes and increased drop formation rate. This was shown in simulations of water dispersed into tetradecane done by Liow et al. [36].

The most interesting observed feature is the monodispersity of the produced drops. T. Nisisako et al. could produce sunflower oil drops in 2 wt% Polyvinylalcohol (PVA) aqueous solution with diameters ranging from 153 μm to 87 μm with a COV below 2 %. In another study they showed that monodispersed drops could only be produced in small area of the process conditions [37]. This was demonstrated with an organic phase dispersed into a 2 wt% PVA aqueous solution. They found that a high productivity and a low COV was only achieved when the Capillary number (Ca) of the dispersed phase was between 8 and $9*10^{-3}$ and the Reynolds number (Re) of continuous phase was within a range of 4 – 10. In this region, drops with diameters from 125 μm down to 30 μm with a COV of 1-2 % were formed. The drop formation rate achieved was around 750 Hz. At higher Re-Numbers the productivity increases further but the drop size distribution becomes polydisperse. Inside this optimal production window the formation of satellite drops (diameter < 5μm) was observed.

The wetting property of the T-junction microfluidic device material is an important factor. The successful production of organic drops in water was only possible with T-junctions fabricated out of glass. The emulsification of water into an organic phase could only be demonstrated with T-junctions with PMMA as the base material [38]. In general, the to be dispersed phase should not wet the T-junction material.

Microchannel emulsification

The microchannel emulsification technique developed by T. Kawakatsu and co-workers was one of the first applications using micro-engineered devices to produce narrow drop size distributed emulsions [39]. In this technique, rectangular microchannels are etched into a silicon wall, which separates the dispersed phase from the continuous phase. Towards the continuous phase the microchannel ends in a terrace, where dispersed phase drops are inflated before they detach as depicted schematically in Figure 4. The whole microchannel plate is covered with a transparent glass or plexiglas cover to allow an optical observation of the drop formation process.

The hydraulic diameter of the microchannels fabricated in silicon varied between 4.2 and 9.6 μm and the aspect ratio from 1.2 to 3.6. The terrace length was mostly about 30 μm. In most of the studies, oil-in-water emulsification was performed due to the hydrophilic nature of silicon. Oil drops of 2.6 to 4.6 times the hydraulic diameter of microchannels were produce with coefficients of variation from 1.4 to 13 % [40-43]. The drop formation process is characterized by the spontaneous transformation of the disk-like drop between the terrace and the cover plate to a spherical drop when the edge of the terrace is reached. This transformation is driven by the Laplace pressure difference between the disk-shaped drop and the spherical shape. The latter one has a lower Laplace pressure, therefore the dispersed phase on the terrace flows faster into the spherical drop than the dispersed phase is supplied. Due to this, necking occurs between the disperse phase on the terrace and the growing spherical drop at the edge of the terrace until the neck ruptures and the spherical drop releases from the edge.

Recently, Liu et al. showed water-in-oil emulsification with acrylic polymer microchannels [44]. The design is similar to the silicon microchannels. It was fabricated by injection molding of the acrylic polymer into a nickel mould. The mould itself was produced by plaiting nickel on a structured glass/photo resist substrate. Water drops with COV values ranging from 5-10 % were formed.

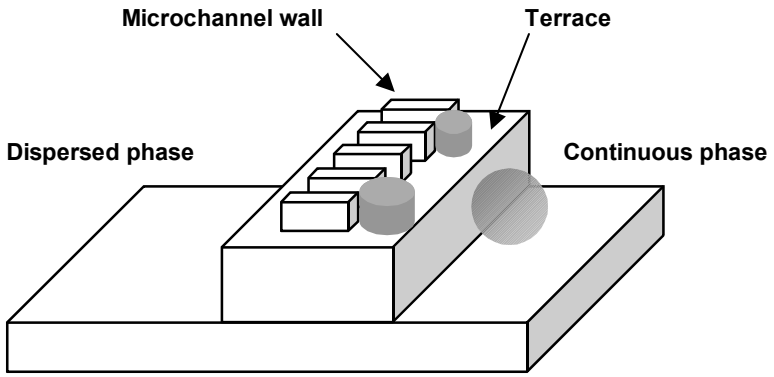

Figure 4: Schematic drawing of a microchannel emulsification device.

Kobayashi and co-workers developed a second design using the spontaneous drop formation process. Here, rectangular microchannels were etched vertically through a silicon plate with a thickness of 100 to 200 μm (see Figure 5). The slit-shaped channels had hydraulic diameters from 10.6 to 22.1 μm. The aspect ratio varied from 3.4 to 5.1. The formed oil drops were 1.9 to 3.5 times larger than the hydraulic diameters of the used microchannels and the coefficient of variations ranged between 1.4 and 10 % [45-48].

Recently, Kobayashi and co-workers designed a new straight-through microchannel emulsification device fabricated out of silicon via photolithography and deep-reactive-ion etching. This design, quite similar to the microchannel/terrace approach, consists of a circular dispersed phase supply channel ending in a high aspect ratio slit towards the continuous phase. The slits themselves have an aspect ratio of 9.5, a hydraulic diameter of 19.9 μm and a depth of 21 μm. With this design, the authors performed successful emulsification of a low viscosity dispersed phase (decane) into 1 wt% aqueous SDS solution. The decane drops had an average diameter of 40.9 μm and a COV of 1.3 % [49].

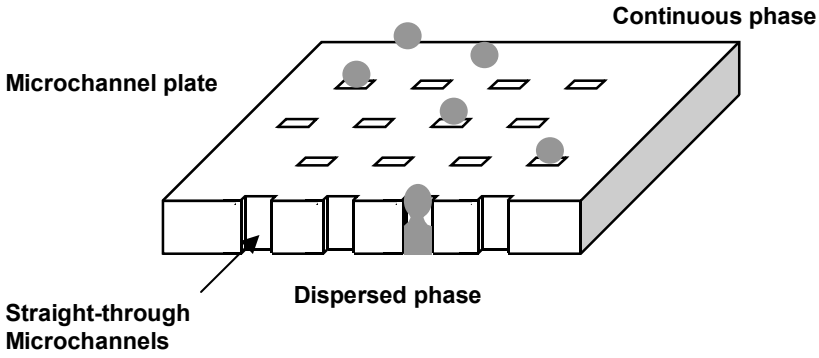

Figure 5: Schematic picture of a straight-through microchannel plate.

Flow-focusing Microfluidic devices

In a flow-focusing device the continuous and the to be dispersed phase are flowing coaxial through a small orifice as schematically shown in Figure 6. The outer continuous phase flows faster than the inner to be dispersed phase.

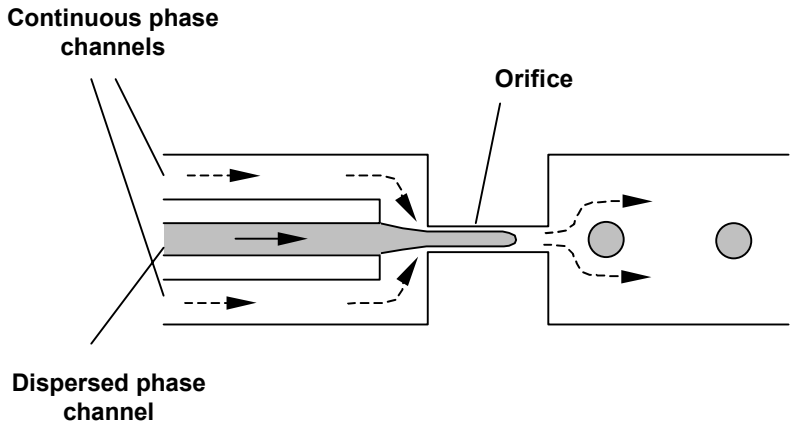

Figure 6: Schematic representation of the design and the drop break-up in a flow-focusing emulsification device.

The drop break-up can occur within the orifice or downstream out of the orifice depending on the total flow rates and the flow ratio of the inner to the outer phase. In flow focusing devices, drop formation occurs due to the competition of viscous

stresses induced by the flow field and capillary stresses due to the interfacial tension between the two phases [50].

Anna et al. showed the water drop formation in silicon oil containing 0.67 wt% Span 80 with an orifice of about 40 μm [51]. The flow-focusing device (FFD) was made out of PDMS using soft lithography fabrication methods. The drop break-up was studied over a wide range of continuous phase flows and volume flow ratios. At low flows of the outer phase and ratios of inner to outer phase of 0.25 to 0.025 the break-up occurs inside or at the exit of the orifice and the produced drops are regular in diameter. At higher flows and smaller ratios the inner phase starts to from jets and the break-up point moves downstream outside of the orifice. The produced drops are polydispersed in size and satellite drops are formed.

Davidson et al. have simulated the drop formation process with a numerical volume-of-fluid method based on the FFD shown by Anna et al. [52]. The results were compared with the drop formation pattern observed by Anna et al. Necking and break-up occurs inside the orifice for small Capillary numbers corresponding to low outer phase flows and relatively high flow ratios. At higher Capillary numbers and smaller flow ratios jetting and satellite drop formation occurs. Drop formation inside the orifice is a drag induced break-up. In this case the inner phase nearly fills-up the whole orifice. For the faster flowing outer phase only a thin annular region is available. This is attributed to a high axial drag, which accelerates the inner phase. The drop break-up at the exit or more downstream of the orifice occurs due to pinching and capillary wave instability. Pinching takes place when the inner phase thread exits the orifice. There, the drag force is reduced and due to the interfacial tension the inner phase forms a bulb. Between the bulb and the fluid thread or jet a waist is formed. The waist formation can be assumed to be a result of capillary wave instability. Further on the waist is thinned by liquid out-flow due to locally higher pressure inside the waist leading to drop break-up.

Anna et al. and Davidson et al. do not report exact drop sizes. In general, the drop sizes are approximately 2 times larger in diameter than the diameter of orifice in case of low Capillary numbers.

Drop sizes and the dependency of the drop size on the volume flow of the continuous phase are reported by Tackeuchi et al. [53]. They used a three-

dimensional flow-focusing device (FFD) made from PDMS with cylindrical geometries for the in- and outlet channels and for the orifice as well, which has a diameter of 250 μm. The former mentioned flow-focusing device had rectangular channels and are so called two-dimensional. In this 3D FFD the dispersion of water drops into 2 wt% Span 80 containing hexadecane was studied. At volume flows of 0.5 ml/h for the inner water phase and 5 ml/h for the outer hexadecane phase the generate drops had a mean diameter of 153 μm and with a COV of 2.5 % quite monodispersed. The diameter of the formed water drops decreases with increasing flow rate of the continuous phase.

1.3 Outline of the thesis

This thesis deals with the formation of emulsions using micro-engineered devices. The main part of the research was focused on the surface modification and wetting behavior of native and modified silicon nitride and on the water drop formation at silicon nitride micro-nozzle plates.
Further on, metal and polymeric micro-nozzle devices were fabricated and finally, a new technique for the generation of monodispersed drops is introduced.

In order to perform successful emulsification of water into oil a hydrophobic surface is needed. In **Chapter 2** different strategies to render the surface of silicon nitride hydrophobic are investigated in terms of hydrophobicity and stability. As hydrophobic coating materials alkyl-chloro silanes, plasma polymerized and dip-coated PDMS were researched.

Chapter 3 is fully dedicated to the interfacial properties of the different coating materials and silicon nitride as well. The researched materials were compared in terms of solid surface energy and wetting behavior in pure and surfactant containing liquids.

The emulsification performance of modified silicon nitride micro-nozzle plates was studied in **Chapter 4** by microscopic observation of the water drop formation

process under shear. The optical observation provided an insight into drop formation rate, number of active nozzles and drop formation time in relation to the applied pressure difference. From the obtained results a direct influence of the dynamic interfacial tension of the used surfactants on the drop formation process was found.

In contrast to the cleanroom-fabricated silicon nitride nozzle plates in **Chapter 5** the emulsification with laser-drilled nozzles with diameters down to 4 μm in aluminum and stainless steel foils are discussed. These metal nozzle plates were used for oil-in-water and for water-in-oil emulsification as well. Beside the nozzle plates a conventional stainless steel mesh was investigated.

Phase separation micromolding is used in **Chapter 6** to obtain perforated polymeric films. Within this technique a cleanroom-fabricated mould is used as a template for the structure of the polymeric film. Different polymers and phase inversion conditions are investigated to obtain perforated and stable films for emulsification experiments.

In **Chapter 7** the principle of a new drop generation method called porous channel emulsification is investigated. Within this technique drops are formed in microchannels embedded in a porous polymer matrix. This designed microfluidic chip allowed the microscopic observation of the formation of monodispersed oil drops.

To finalize this thesis **Chapter 8** summarizes briefly the main findings and conclusions. Further on, an outlook, some personal views and recommendations are given for future research.

1.4 Abbreviations

COV	Coefficient of variations
FFD	Flow-focusing device
MPG	Micro porous glass

PDMS	Polydimethylsiloxane
PMMA	Polymethmethylacrylate
SDS	Sodium dodecylsulfate
SPG	Shirasu porous glass

1.5 References

[1] H. Karbstein, H. Schubert, Chemical Engineering and Processing 34 (1995) 205-211

[2] H.P. Schuchmann, T. Danner, Chemie Ingenieur Technik 76 (2004) 364-375

[3] National Institute of Standards and Technology (NIST), Particle Size Characterisation, Special Publication 960-1 (2001)

[4] S. Schultz, G. Wagner, J. Ulrich, Chemie Ingenieur Technik 74 (2002) 901-909

[5] K. Urban, G. Wagner, D. Schaffner, D. Röglin, J. Ulrich, Chem. Eng. Technol. 29 (2006) 24-31

[6] J. Floury, J. Legrand, A. Desrumaux, Chem. Eng. Sci. 59 (2004) 1285-1294

[7] H. Schubert, K. Ax, O. Behrend, Trends in Food Sci. & Technol. 14 (2003) 9-16

[8] A.J. Abrahamse, R. van Lierop, R.G.M. van der Sman, A. van der Padt, R.M. Boom, J. Membr. Sci. 204 (2002) 125-137

[9] G. Muschiolik, S. Dräger, I. Scherze, H.M. Rawel, M. Stang, in Food Colloids; E. Dickinson, B. Bergeståhl, Eds.; The Royal Society of Chemistry; Cambrigde, 1997 No. 192 393-400

[10] V.B. Galazka, E. Dickinson, D.A. Ledward, Food Hydrocolloids 10 (2) (1996) 213-219

[11] R. Katoh, Y. Asano, A. Furuya, K. Sotoyama, M. Tomita, J. Membr. Sci. 113 (1996) 131-135

[12] R.A. Williams, S.J. Peng, D.A. Wheeler, N.C. Morley, D. Taylor, M. Whalley, D.W. Houldsworth, TransIChemE 76 Part A (1998) 894-901

[13] S.M. Joscelyne, G. Trägårdh, J. of Food Engineering 39 (1999) 59-64

[14] V. Schröder, H. Schubert, Colloids and Surfaces A 152 (1999) 103-109

[15] I. Scherze, K. Marzilger, G. Muschiolek, Colloids and Surfaces B 12 (1999) 213-221

[16] I. Kobayashi, M. Yasuno, S. Iwamoto, A. Shono, K. Satoh, M. Nakajima, Colloids and Surfaces A 207 (2002) 185-196

[17] M. Rayner, G. Trägårdh, Desalination 145 (2002) 165-172

[18] V. Schröder, O. Behrend, H. Schubert, J. Colloid Interface Sci. 202 (1998) 334-340

[19] H. Yuyama, T. Watanabe, G-H. Ma, M. Nagai, S. Omi, Colloids and Surfaces A 168 (2000) 159-174

[20] G.T. Vladisavljevic, S. Tesch, H. Schubert, Chemical Engineering and Processing 41 (2002) 231-238

[21] Y.K. Ha, H.J. Lee, J.H. Kim, Colloids and Surfaces A 145 (1998) 281-284

[22] V. Schröder, PhD Thesis 1999, Universität Karlsruhe (Germany)

[23] G.T. Vladisavljevic, H. Schubert, Desalination 144 (2002) 167-172

[24] S. van der Graaf, C.G.P.H. Schroën, R.G.M. van der Sman, R.M. Boom, J. Colloid Interface Sci. 277 (2004) 456-463

[25] M. Yasuno, M. Nakajima, S. Iwamoto, T. Maruyama, S. Sugiura, I. Kobayashi, A. Shono, K. Satoh, J. Membr. Sci. 210 (2002) 29-37

[26] S.M. Joselyne, G. Trägårdh, J. Membr. Sci. 169 (2000) 107-117

[27] C. Charcosset, I. Limayem, H. Fessi, J. Chem. Technol. Biotechnol.79 (2004) 209-218

[28] G.T. Vladisavljevic, M. Shimizu, T. Nakashima, J. Membr. Sci. 250 (2005) 69-77

[29] G.T. Vladisavljevic, R.A. Williams, Advances in Colloid and Interface Science 113 (2005) 1-20

[30] C.J.M. van Rijn, M.C. Elwenspoek, IEEE proc. MEMS 1995 83

[31] Nano and Micro-engineered Membrane Technology, Chapter 11: Membrane Emulsification, C.J.M. van Rijn, Elesevier Amsterdam, 2004, ISBN 0.444-41489-9

[32] T. Nisisako, T. Torii, T. Hoguchi, Lab Chip 2 (2002) 24-26

[33] S. van der Graaf, T. Nisisako, C.G.P.H. Schroën, R.G.M. van der Sman, R.M. Boom, Langmuir 22 (2006) 4144-4152

[34] J. Hunsy, H. Jin, E. Harvey, J. Cooper-White, 7th International Conference on Miniaturized Chemical and Biochemical Analysis Systems, October 5-9, 2003, Squaw Valley, California, USA

[35] P. Garstecki, M.J. Fuerstman, H.A. Stone, G.M. Whitesides, Lab Chip 6 (2006) 437-446

[36] J.L. Liu, 15th Australasian Fluid Mechanics Conference, University of Sydney, Australia, 2004

[37] T. Nisisako, T. Torii, T. Higuchi, Chemical Engineering Journal 101 (2004) 23-29

[38] T. Nisisako, T. Torii, T. Higuchi, SICE 2002, Aug. 5-7, 2002, Osaka

[39] T. Kawakatsu, Y. Kikuchi, M. Nakajima, JAOCS 74 (1997) 317-321

[40] S. Sugiura, M. Nakajima, J. Tong, H. Nabetani, M. Seki, J. Colloids Interface Sci. 227 (2000) 95-103

[41] T. Kawakatsu, G. Trägårdh, C. Trägårdh, J. of Food Engineering 50 (2001) 247-254

[42] S. Sugiura, M. Nakajima, S. Iwamoto, M. Seki, Langmuir 17 (2001) 5562-5566

[43] J. Tong, M. Nakajima, H. Nabetani, Eur. J. Lipid Sci. Technol. 104 (2002) 216-221

[44] H. Liu, M. Nakajima, T. Nishi, T. Kimura, Eur. J. Lipid Sci. Technol. 107 (2005) 481-487

[45] I. Kobayashi, M. Nakajima, K. Chun, Y. Kikuchi, H. Fuijata, AIChE Journal 48 (2002) 1639-1644

[46] I. Kobayashi, M. Nakajima, Eur. J. Lipid Sci. Technol. 104 (2002) 720-727

[47] I. Kobayashi, S. Mukataka, M. Nakajima, Ind. Eng. Chem. Res. 44 (2005) 5852-5856

[48] I. Kobayashi, S. Mukataka, M. Nakajima, Lamgmuir 21 (2005) 5722-5730

[49] I. Kobayashi, S. Mukataka, M. Nakajima, Langmuir 21 (2005) 7629-7632

[50] V. Cristini, Y.C. Tan, Lab Chip 4 (2004) 257-264

[51] S.L. Anna, N. Bontoux, H.A. Stone, Applied Physics Letters 82 No. 3 (2003) 364-366

[52] M.R. Davidson, D.J.E. Harvie, J.J. Cooper-White, ANZIM J. 46 (E) (2005) C47-C58

[53] S. Takeuchi, P. Garstecki, D.B. Weibel, G.M. Whitesides, Adv. Mater. 17 No. 8 (2005) 1067-1072

Chapter 2

Chemical and thermal stability of organic-silicon based coatings for membrane emulsification [1]

Abstract

Silicon nitride microsieves are excellent candidates for the membrane emulsification processes. These microsieves have well-defined pores with extremely narrow pore size distributions. To produce water-in-oil emulsions the surface of the microsieves has to be altered from a hydrophilic to a hydrophobic state. We establish this by applying a coating based on self-assembled monolayers of alkylchlorosilanes and by PDMS coatings. This paper focuses on the chemical and thermal stability of these coatings considering the cleaning procedures used in food and diary industry.

[1] This Chapter has been partly published as: M.J. Geerken, T.S. van Zanten, R.G.H Lammertink, Z. Borneman, W. Nijdam, C.J.M. van Rijn, M. Wessling, Adv. Eng. Mat. 6 (2004) 749-754

2.1 Introduction

Emulsification techniques are widely used in food, pharmaceutical and cosmetic industry to produce oil-in-water or water-in-oil emulsions. Commonly used emulsification techniques include rotor-stator systems, high-pressure homogenizers and ultrasound [1]. Due to high shear forces, the dispersed phase is divided into small droplets stabilized by surfactants. However, shear stress and thermo sensitive ingredients, such as proteins, may loose their bioactivity during this process [2].
Cross-flow membrane emulsification is a relative new emulsification process. This technique requires less energy, generates less stress to the ingredients and produces narrower drop size distributions [3]. In this process, the dispersed phase is forced through a porous membrane into the flowing continuous phase (see Figure 1).

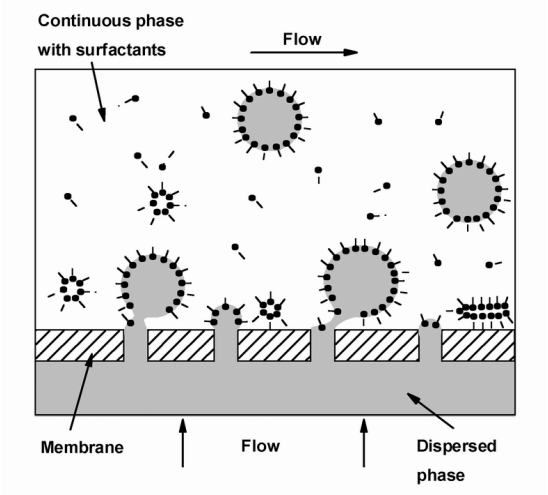

Figure 1: Membrane emulsification process for water-in-oil emulsions.

Droplet formation by macroporous membranes requires a surface, which is not wetted by the dispersed phase. In case the dispersed phase wets the membrane, spreading of the dispersed phase over the membrane surface will occur resulting in the production of big strings instead of droplets.

Table 1: Used membranes for cross-flow membrane emulsification.

Membrane material	Type of emulsions	References
Al_2O_3	Oil-in-water	[4,5]
Shirasu Porous Glass (SPG)	Oil-in-water	[6,7,8]
Polycarbonat	Oil-in-water	[9]
Polypropylene	Water-in-oil	[10]

Lately, in several studies on membrane emulsification, different types of microporous membranes were investigated. As Table 1 indicates, most of them were exploited for the production of oil in water emulsions requiring hydrophilic membranes.

Until now, membrane emulsification technology has not found its way to large-scale emulsion production. This is due to the fact that commercially available membranes possess some disadvantages; they require a high-pressure drop and consist of a highly porous and irregular morphology on a microscopic scale [11]. To overcome these disadvantages, a micro- engineered membrane was adopted from microfiltration [12]. This microsieve membrane, fabricated from silicon nitride with a silicon support, has a precisely defined pore size and a narrow pore size distribution as shown in Figure 2, combined with a micron-sized membrane thickness.

As previously mentioned, membrane emulsification requires a surface that is not wetted by the dispersed phase. A hydrophobic surface is required for producing water-in-oil emulsion whereas for oil-in-water emulsions a hydrophilic surface is needed. Due to the silicon nitride processing conditions, groups like silanol (SiOH), primary ($SiNH_2$), and secondary amino groups (Si_2NH) are present at the surface [13]. Overall, this results in a more hydrophilic than hydrophobic surface.

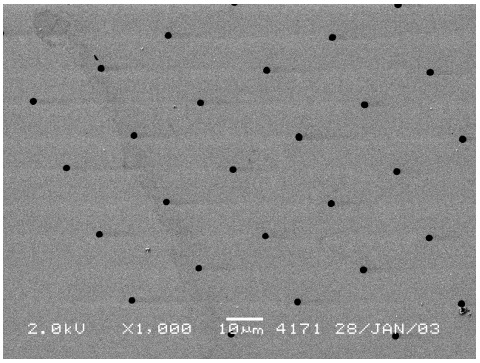

Figure 2: SEM picture of a silicon nitride microsieve with defined pore size (2 μm) and pore distribution (pore to pore distance 20 μm) designed for membrane emulsification.

In this paper, we discuss the results of modifying the surface properties of silicon nitride to a more hydrophobic state via self-assembled monolayers (SAMs) of organosilanes, plasma polymerized, and dip-coated PDMS coatings. We focus in particular on their chemical and thermal stability considering the rigorous cleaning procedures used in food and diary industry.

2.2 Self-assembly monolayers based on organosilanes

Self-assembled monolayers are well known as anti-sticking coatings for micro-electromechanical systems (MEMS). In these micro-scaled systems the adsorption of water from humid air onto the surface decreases their performance and lifetime. To prevent this negative effect, surface modifications are used to increase the hydrophobicity. The water contact angle can rise from below 30° on SiO_2 surfaces to 110° on SAM-coated surfaces [14].

The formation of silane based SAMs is described in literature for different silanes on silicon and silica substrates. Applied silanes for hydrophobization include alkyl-chlorosilanes (R_nSiCl_{3-n}), perfluorinated alkylchlorosilanes ($(CF_3(CF_2)_m(CH_2)_n)_pSiCl_{3-p}$) and alkylalkoxysilanes ($(CH_3(CH_2)_mO)_3$-Si-R). A variety of silanes, either alkylchloro or alkylalkoxy, with epoxy, amine or thiol terminated alkyl chains are exploited to create hydrophilic surfaces [15,16].

Due to the fact that chlorosilane coupling agents have a low affinity for the surface it is necessary to convert them into silanol groups [17]. By reacting with water the chlorine atoms split off and hydroxide head groups are formed, which have a higher affinity to the silicon surface. This leads to an adsorption of the hydroxysilanes on the surface (see Figure 3). The hydrolysis step is followed by the reaction between the hydroxide groups and the silanol groups present on the surface resulting in a covalent Si-O-Si bond. Ideally, the resulting SAM contains molecules that are both covalently linked to the substrate as well as to their neighbors.

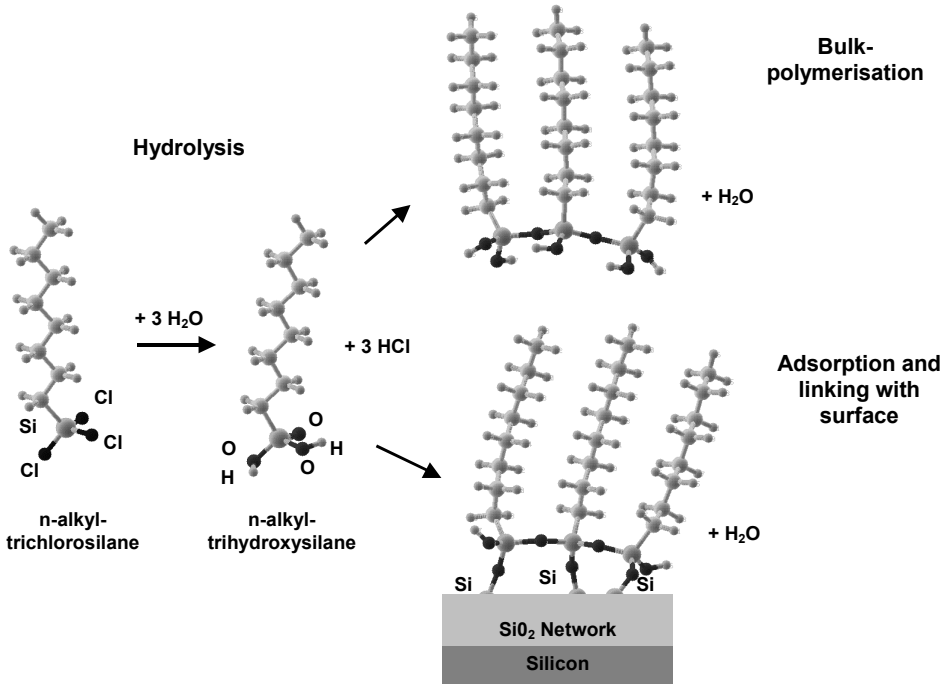

Figure 3: Schematic illustration of the SAM formation on silicon.

Preferably, hydrolysis takes place close to the silicon surface, but the presence of water in the coating solution can result in bulk-polymerization of the silanes before they react with the surface. On the one hand, water is absolutely necessary for SAM formation but on the other hand it is unwanted in the coating solution. To avoid bulk-polymerization, it is recommended to use solvents with a very low water content [17]. If the silicon substrate is exposed to humid air before immersing it into the

coating solution the desired water will be present on the surface as a thin adsorbed water layer [18,19].

Reported values for water contact angles as an indication for the quality of the silane based SAMs and their hydrophobicity range from 90° to 115° depending on the used coating agent (carbon chain length) [18,19,20]. The thermal stability in air, nitrogen and vacuum is well reported. For octadecyltrichlorosilane monolayers (ODTS) constant water contact angles are observed up to 200°C in air and up to 500°C in nitrogen for short annealing durations [19,21,22].

Less reported is the chemical stability of the silane based SAMs. Iimura et al. studied the chemical resistance of long chain tri-, di- and monochloroalkylsilanes under different conditions [23]. They found that the stability in organic solvents (e.g. benzene, ethanol, chloroform), in acidic (pH 1) and in alkaline solutions (pH 13) decreased from trichloro- to monochloroalkylsilanes. The best results were observed for octadecyltrichlorosilane (ODTS) based SAMs, which show no dramatic changes in the intensity of the observed CH_2 infrared stretching bands after being exposed to the mentioned conditions.

2.2.1 Experimental

For the SAM formation two types of alkyltrichlorosilanes were used. Octyltrichlorosilane (OTS) (Aldrich, 97 %) and a perfluorinated octyltrichlorosilane (FOTS) (Fluka, >97%) were used as received. For the preparation of the coating solutions n-hexadecane (Aldrich, >99 %, < 0.005 % H_20) and chloroform (Merck, 99 %, <0,01 % H_20) were used as solvents and dried with molecular sieves to water content below 0.002 %.

A single crystalline silicon wafer (type <100>) is coated with a thin layer (1.2 µm) of LPCVD silicon nitride (low pressure chemical vapor deposition, Tempress Omega junior system). At a temperature of 850°C, a gas mixture of dichlorosilane (SiH_2Cl_2) and ammonia (NH_3) reacts and will form silicon nitride. Using an excess of dichlorosilane (70sccm:18sccm), silicon rich nitride is formed that has less internal stress than stochiometric nitride [24]. Bare silicon wafers coated with a thin silicon nitride (Si_xN_y) layer were cleaned by using a reactive oxygen plasma (10 min, 500

W, pO_2 = 16 mbar) to remove adsorbed impurities. This method is one of the most efficient especially to remove organic contaminants [25].
The SAM formation took place in a solution of 2.5 mmol/l silane in a mixture of dried n-hexadecane and chloroform (4/1 v/v). The wafers were placed in the solution for one hour at room temperature and ambient pressure. Afterwards the wafers were removed from the solution and extensively rinsed first with iso-propanol, then with ultra pure water and dried with nitrogen. After the formation step a stabilization step followed. Following the procedure of Srinivasan et al. [18] the coated wafers were heated at 100°C for 1h in an oven flushed with nitrogen. It must be pointed out that use of dry equipment is required and that the SAM formation is carried out under a nitrogen atmosphere to prevent an increase of the water content.
The thermal and chemical stability was tested under different temperatures and pH-values adjusted with sodium hydroxide and nitric acid. The wafers were stored for several days under these conditions and the changes were observed by measuring the water contact angle in air using a Gonionometer from Dataphysics (OCA 15+).

2.2.2 Results

SAM-Formation

Table 2 depicts the results of the static water contact angle measurements in air and hexadecane. Figure 4 shows the corresponding images of water drops on silicon nitride, FOTS and OTS coated silicon nitride while immersed in hexadecane. FOTS shows somewhat lower water contact angles in hexadecane compared to OTS. This can be explained by the lower hexadecane-OTS interfacial energy compared to hexadecane-FOTS (Chapter 3). Fluorocarbons are known to have lower critical surface tensions compared to hydrocarbons and perfluorinated trichlorosilanes are the most effective chlorosilane reagents to produce hydrophobic coatings [14]. In general, perfluorinated SAMs are known to have a higher hydrophobicity compared to hydrocarbon SAMs [26].

Table 2: Results contact angle measurements.

	FOTS	OTS
Water/air [°]	112 ± 4.0	104.9 ± 2.0
Water/hexadecane [°]	148.9 ± 3.9	163.6 ± 1.1

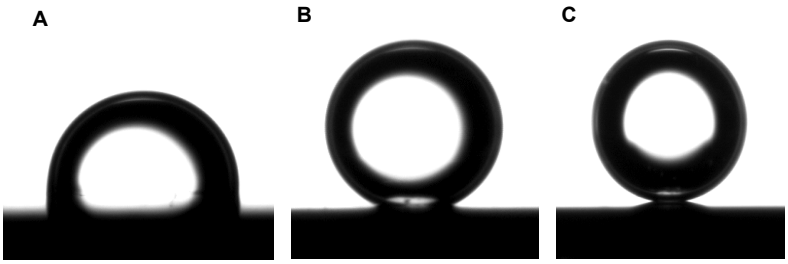

Figure 4: Water drops in hexadecane on untreated silicon nitride (A), FOTS coated (B) and OTS coated silicon nitride (C).

Stability

Following the surface modification the stability under various conditions was studied. Trichlorosilane coatings are bonded to a silicon surface via Si-O-Si bonds as mentioned before. The alkyl chains are, from a chemical point of view, very stable and in case of fluorocarbons even inert. The weak point of these coatings is the substrate bonding part of the molecules. It is known, that the silicon-oxygen bond is susceptible towards hydrolysis under basic conditions [27]. To increase the stability under alkaline conditions it is necessary to form a well-ordered and dense monolayer that prevents the penetration of OH^- ions and water through the monolayer to the bonding part [23].

At first the chemical stability was studied. Coated wafers were exposed to different aqueous solutions with varying pH-values for several days. It was found, that coatings are stable from pH 2 to 11.5 for FOTS and to pH 10 for OTS during the observed time scale (see Figure 5). When treated with a sodium hydroxide solution of pH 13 the contact angle decreases in both cases very dramatically to values typical for oxidized silicon.

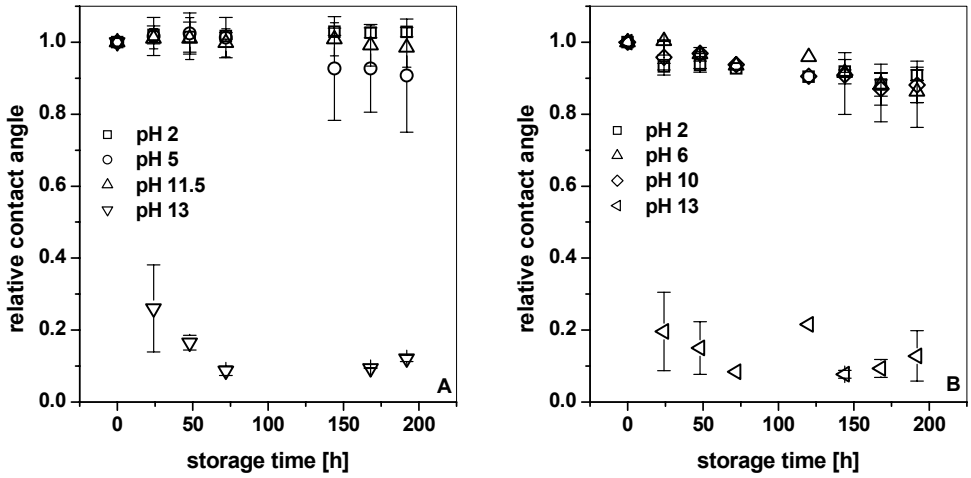

Figure 5: Chemical stability of FOTS (A) and OTS (B) coatings on silicon nitride wafers.

Next, the thermal stability in water was studied. Figure 6 shows the changes of the relative water contact angles for three different temperatures. It can be seen that the thermal stability of FOTS coatings is at all temperatures superior compared to OTS. This corresponds with the limited water penetration through the FOTS layer compared to OTS.

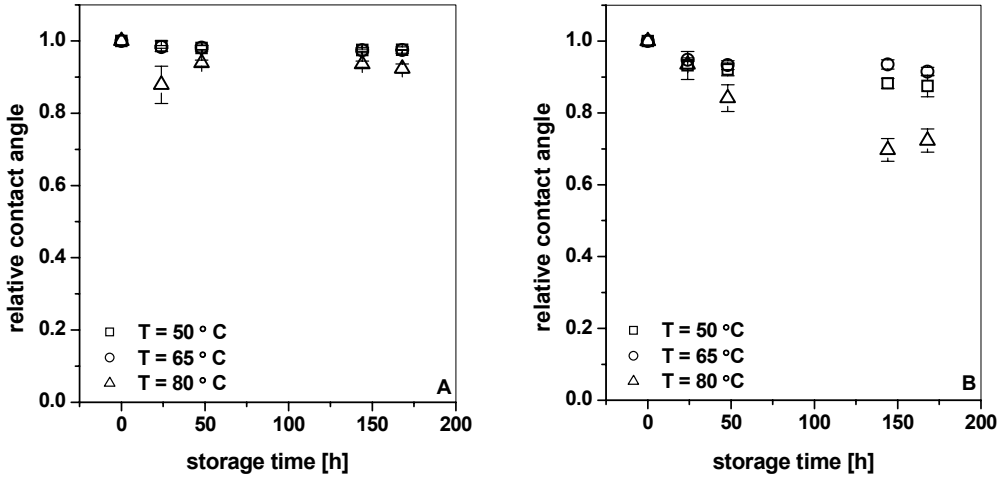

Figure 6: Thermal stability of FOTS (A) and OTS (B) coatings on silicon nitride wafers.

However, literature only reports on thermal stability in vacuum, nitrogen and air. Sirnivasan et al. compared the thermal stability of ODTS and perfluorinated ODTS (FODTS) in air with a humidity not specified and in nitrogen [18]. In air and up to 400°C, FODTS is more stable compared to ODTS and in nitrogen both show the same stability decrease with increasing temperature. In inert environments like vacuum and nitrogen the thermal stability is determined by splitting the Si-C or C-C bonds [19]. In reactive environments like hot air the C-F bond, which is difficult to polarize, shields the C-C bonds of the backbone leading to increased stability for the perfluorinated compared to the corresponding hydrocarbons. In hot water the hydrolization of the Si-O-Si bond determines the thermal stability.

Cleaning procedures used in food industry combine heat and chemical treatments. Figure 7 depicts the results of FOTS coatings treated with hot nitric acid solutions (pH 5) and with hot sodium hydroxide solutions (pH 10) for nearly 180 h. After this treatment the coating remains hydrophobic. The initial water contact angle decreases less than 5 percent at pH 10 and less than 10 percent at pH 5 for all temperatures studied.

Figure 8 shows the results for OTS. When exposed to pH 5 at 50 and 65°C, the water contact angle only decreased to about 90 percent of the initial value. At 80°C, however, it decreased to half of its initial value. An even more dramatic loss of hydrophobicity can be observed in case of hot sodium hydroxide solutions.

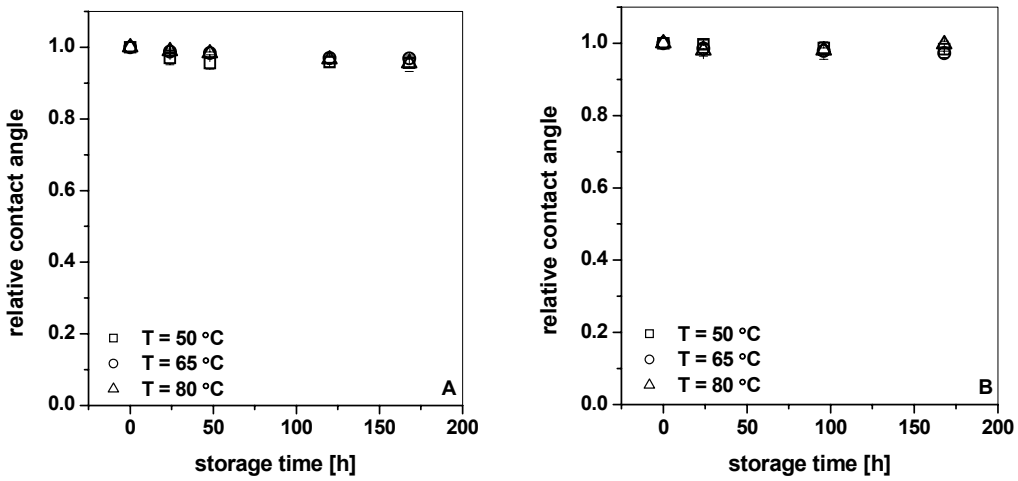

Figure 7: Stability of FOTS coatings at different temperatures and pH-values (A: pH 5, B: pH 10).

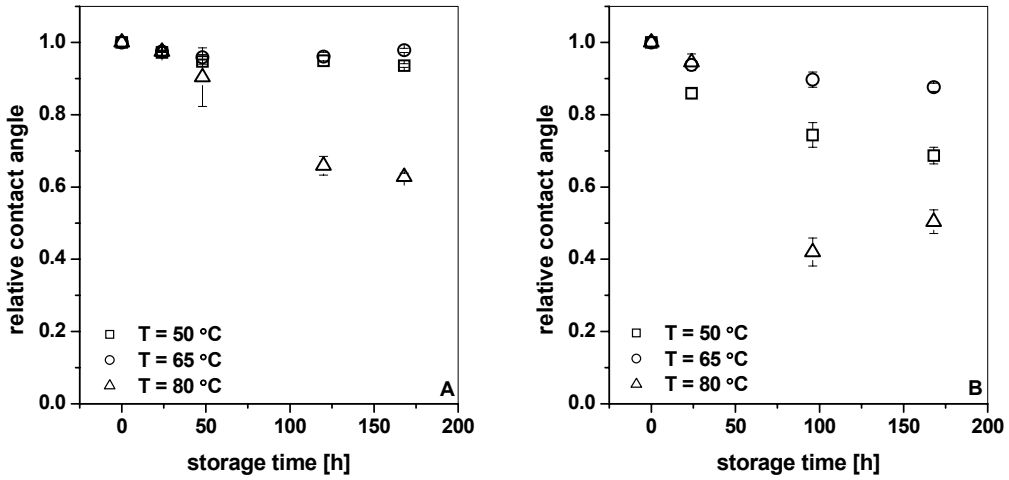

Figure 8: Stability of OTS coatings at different temperatures and pH-values (A: pH 5, B: pH 10).

2.2.3 Conclusions

Several methods using alkylsilanes on silicon are described and can be adopted to render Si_xN_y microsieves hydrophobic. A key factor is the stability. In food, diary, and

pharmaceutical industry equipment is cleaned by using hot alkaline and acidic solutions. Surface modifications have to withstand these conditions. Most often, the reported stability studies of alkylsilane based surface modifications describe the thermal stability in hot air, nitrogen or vacuum.
The perfluorinated coating is more stable than the corresponding hydrocarbon coatings. It withstands acidic and alkaline conditions in a range from pH 2 to 11.5, it is thermally stable in hot water up to 80 °C and it also withstand hot nitric acid and hot sodium hydroxide solutions in the time scale of the experiment. The OTS coating cannot perform these features in all cases.
The produced FOTS coatings seem to have a better ordered and denser structure than OTS, which causes a better protection against the hydrolysis of the Si-O-Si bonds. Main differences between both coatings are different polarities, different structure and density. From polymer science it is known that polytetrafluoroethylene (PTFE) has a two times denser crystal structure combined with a much higher melting temperature compared to polyethylene (PE) [28]. Besides that, PTFE is more resistant towards acidic and alkaline environments compared to PE. These properties are reflected in the stability of the studied SAMs, which clearly favor the perfluorinated one.

2.3 PDMS based coatings

PDMS films and coatings are widely used in many fields and applications. PDMS offers good chemical and thermal resistance, good mechanical properties and water repellency as well. In soft lithography, PDMS is the major material to fabricate micro- and nano-structured surfaces and devices because of its excellent properties [29].
In the biomedical field, PDMS films made by plasma polymerization of mostly hexamethyldisiloxane (HMDSO) are used to enhance the biocompatibility of implants [30]. Thin PDMS films are applied in the semiconductor industry as low dielectric films. In this field the plasma polymerization of HMDSO in combination with low molecular organic materials like methane or toluene and gases like oxygen or argon is also quite often performed [31,32].

HMDSO as a precursor for plasma polymerized PDMS films and coatings has the benefit that it is safe and easily to handle, it provides high deposition rates and the film properties are adjustable over a wide range by changing the deposition conditions [30]. The plasma polymerization process itself offers the ability to cover micro-structured surfaces without changing the structure geometry significantly. The thickness of the films is easy to adjust and can be varied in range of some nanometers to micrometers.

Beside plasma deposition, spin- and dip-coating processes can be used to form thin films of PDMS. The thickness of films formed by dip- or spin-coating of PDMS/cross-linker solutions in various organic solvents are also tunable in the same range as plasma deposited films depending on the spin-coating conditions [33,34]. But it does not work for structured substrates. In case of silicon nitride microsieves this will negatively influence the emulsification performance. Gironès et al. spin-coated thin polyethersulfone (PES) films on silicon nitride microfiltration sieves. Even at low concentrations of PES, ensuring low viscosity, blockage of pores still occurred [35].

The degradation of PDMS by water, acids and base is a result of cleavage of the silicon-oxygen-silicon bonds in the backbone of PDMS creating silanol groups. This results in a loss of hydrophobicity and weight over the exposure time to these environments. After the exposure, the hydrophobicity can be recovered by aeration, which is caused by a rearrangement of methyl side groups towards the surface enabled by the high mobility of the PDMS chains. A second effect is the recondensation of adjacent silanol groups [36].

Here, we chose two different ways to obtain thin PDMS coatings on silicon nitride; plasma polymerized PDMS and dip-coated PDMS films.

2.3.1 Plasma polymerized PDMS coatings

Two different types of PDMS were obtained from an external supplier (The Fraunhofer Institute for Manufacturing and Applied Materials Research, Bremen, Germany).

Both coatings were produced by plasma polymerization of HMDSO mixed with different ratios of oxygen. The thickness is 87 nm for PDMS 14 and 94 nm for PDMS

18. The PDMS 14 is used as an “easy-to-clean” coating for baking trays, commercialized under the trade mark ”Best Skin” and patented (WO 03/002269 A2). PDMS 18 is used as permanent mold release layer and patented (DE 10034737 A1).

2.3.1.1 Results

Contact angles

Water contact angles in air for plasma polymerized PDMS are shown in Table 3. These values are comparable with reported values ranging from 75 to 105° depending on polymerization parameters and conditions [37,30]. It is known that the water contact angle of PDMS decreases with increasing amount of oxygen. Surface oxidation by UV/ozone showed that the contact angle of untreated PDMS could be stepwise decreased from above 100° to 20° by increasing the oxidation time [38].

Table 3: Contact angles of plasma polymerized PDMS.

	PDMS 14	PDMS 18
Water/air [°]	93.5 ± 0.9	103.4 ± 1.8
Water/hexadecane [°]	137.0 ± 5.7	153.0 ± 0.5

The water/hexadecane contact angle of PDMS 14 is lower compared to both silane monolayers. In contrast, PDMS 18 shows a higher water/hexadecane contact angle than the perfluorinated silane monolayer but lower then the alkyl silane monolayer. This can be explained by different interactions between the medias, which will be discussed in Chapter 3 in detail.

Stability

Both types of the high cross-linked PDMS were tested in the same way as the silane based coatings. A combination of different chemical environments with different

temperatures was used. At first, the results for PDMS 14 stored in hot acidic (HNO_3, pH 5) and hot alkaline (NaOH, pH 10) are shown in Figure 9.

Obviously, the resistance against acidic conditions is better than against an alkaline environment. The silicon-oxygen-silicon bond, which forms the backbone of any siloxane, is quite sensitive to hydrolysis by hydroxide ions. This will locally crack the backbone. Only for 80ºC the contact angle decrease very significantly, indicating a high degree of hydrolysis and oxidation of the coating. This was not observed for the lower temperatures. Even if cracking of the backbone occurs to a certain extent and silanol groups are formed, which will render the surface hydrophilic, methyl side groups are still present. And due to a high cross-linked network, an orientation of the silanol groups towards the surface might be restricted by steric hindrance.

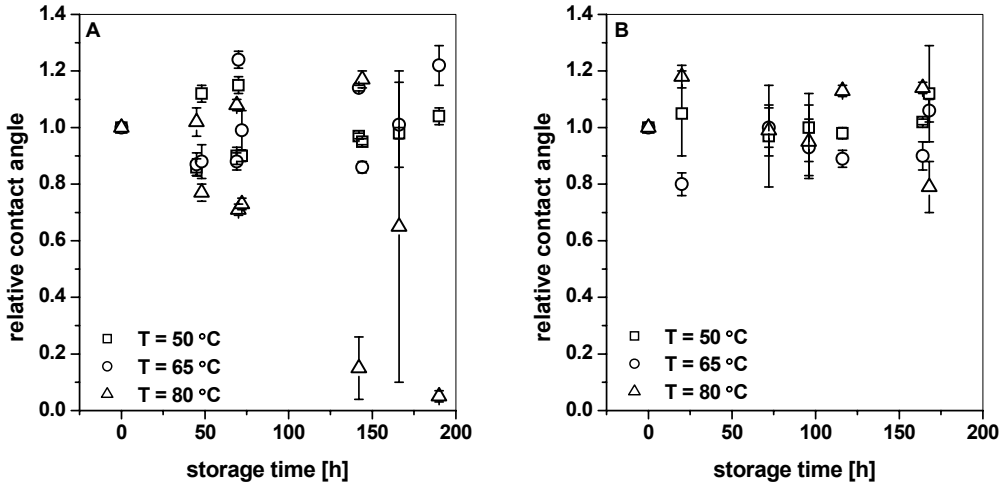

Figure 9: Chemical and thermal stability of PDMS 14 in hot sodium hydroxide (A) and hot nitric acid (B).

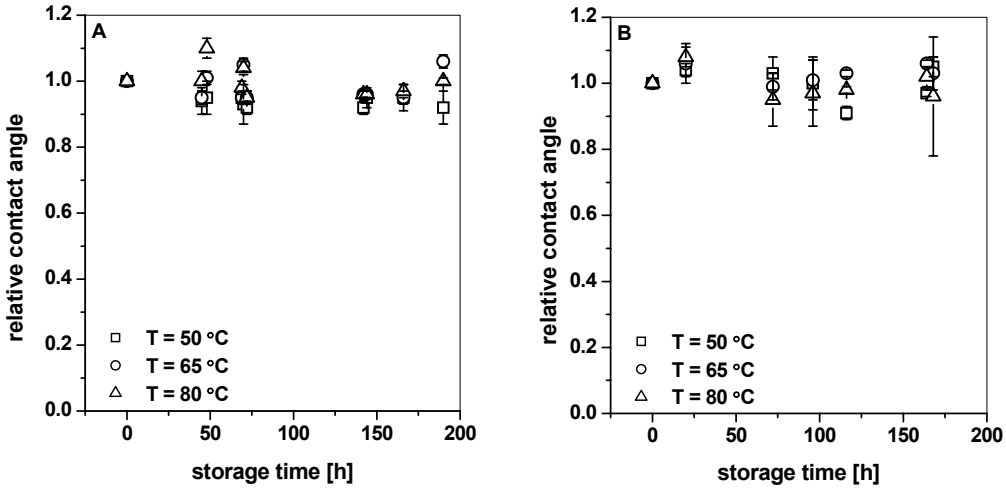

Figure 10: Chemical and thermal stability of PDMS 18 in hot sodium hydroxide (A) and hot nitric acid (B).

Compared to experimental data found for PDMS 18 the data points in case of PDMS 14 are very broad distributed. These scattering values indicate that the degradation of the PDMS 14 layer results in quite inhomogeneous surface. The stability of PDMS 18 in hot acid is quite good as well as in hot sodium hydroxide solution as. Figure 10 shows the results for PDMS 18. The contact angles only decrease 10 to 15 percent in the observed time scale and therefore it provides superior stability compared to PDMS 14.

2.3.1.3 Conclusions

We could show that plasma polymerized HMDSO films with low oxygen content have high water/air and water/hexadecane contact angles. Beside the excellent hydrophobicity, they provide a good chemical and thermal stability in acidic and alkaline environments. Together with the fact that pore blocking cannot occur during the coating process, the coatings are suitable for modifying silicon nitride microsieves.

2.3.2 Dip-coated PDMS coatings

2.3.2.1 Experimental

Here, a commercial available PDMS/water emulsion (Silfar, Wacker Chemie – Germany) is used to produce a hydrophobic surface on silicon nitride. In general, it is used for the hydrophobization of food and pharmaceutical glassware. For this use it is FDA approved.
Before use the PDMS emulsion was diluted with Milli-Q water from 35 vol% to 0.5 – 1.5 vol% PDMS. The silicon nitride or pure silicon samples were cleaned and oxidized by oxygen plasma. The plasma treated samples were dipped in a diluted PDMS emulsion. Due to the oxidized surface the samples are completely wetted after the dipping step. The wetted samples were cured at different temperatures (200–350°C) for different periods of time (15–60 min) to establish a covalent bonding between the oxidized silicon nitride surface and the PDMS chains. Superfluous PDMS is rinsed away with iso-propanol and water after the curing step. This procedure was adapted from T. Mundry et al. [40]. The thickness of the resulting PDMS layers was measured to be around 5 nm by elipsometry.

2.3.2.2 Results

Film formation and contact angles

The films obtained by this method were apparently smooth and homogenous after the final washing step. In Figure 11, optical microscope pictures show the surface of the coated silicon nitride at different steps of the film formation process with a 1 vol% PDMS emulsion.

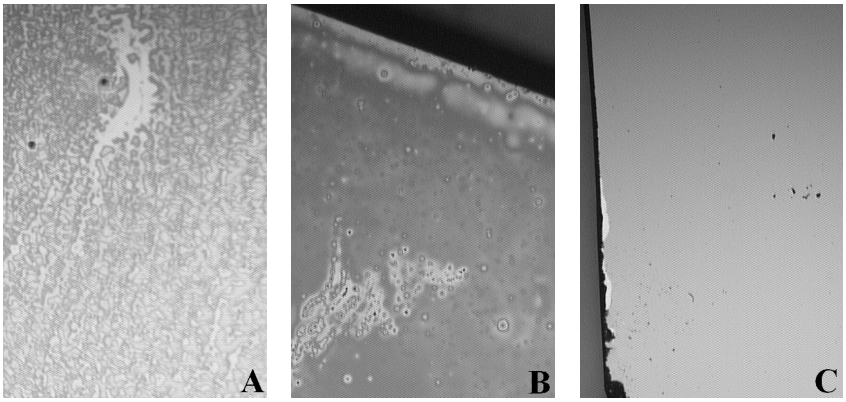

Figure 11: Optical microscope pictures of the substrate surface at different steps of the coating procedure (1 vol% PDMS, 250°C, 15 min). After coating and drying (A), after curing (B) and after the final washing step (C).

The first picture was taken after dip-coating and drying showing a quite inhomogeneous film. The second picture shows the same sample after curing at 250°C for 15 min. The surface still looks inhomogeneous and apparently not smooth. In the last picture, after final washing step, the surface is quite homogeneous.

To achieve high contact angles the influence of different PDMS concentrations, annealing temperatures and annealing periods were investigated. The concentration was varied from 0.5 to 1.5 vol%. The range of the annealing temperature was fixed between 250 and 350°C. The annealing time was set in a range from 15 to 60 min.

From Figure 12 it can be seen that increasing the concentration leads to an increasing contact angle. The high value for 1.5 vol% PDMS might not only be a result of the chemical modification. Roughness can also be accounted here, which is known to enhance the hydrophobicity. The hydrophobicity is comparable to the silane-modified surfaces.

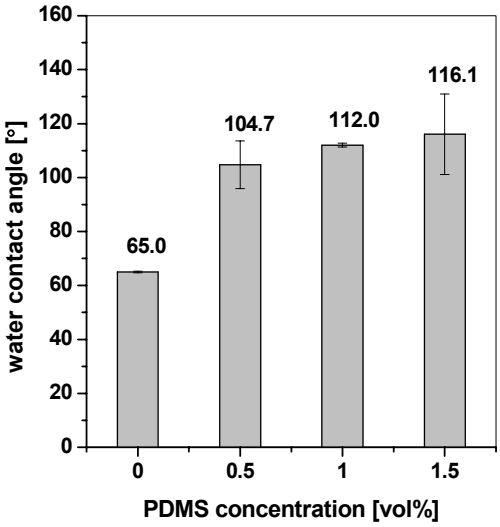

Figure 12: Effect of different PDMS concentrations on the water/air contact angle. Samples were cured at 250ºC for 15 min. The zero denotes a bare silicon nitride sample.

In Figure 13, the influence of different annealing temperatures and durations is shown. The contact angles are increasing with increasing curing time and temperature. In case of 0.5 vol% and 250°C the effect of the curing time is very significant. Increasing the annealing temperature to 300 or 350°C improves the hydrophobicity only slightly. Changing to a PDMS concentration of 1.5 vol% at a constant temperature of 350°C does not have a great influence. The contact angles only increase a few degrees compared to using 0.5 vol% PDMS. From an optical observation by light microscopy, the surface of the samples modified with 1.5 vol% PDMS at 350°C appears quite rough even after rinsing and washing several times with iso-propanol. In this case, the superfluous PDMS cannot be removed probably due to a cross-linking between PDMS chains.

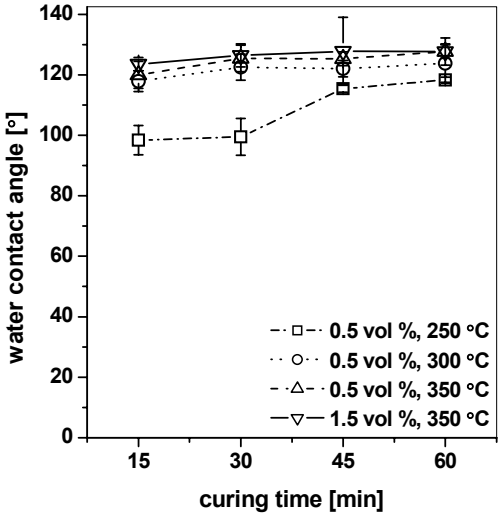

Figure 13: Effect of different annealing temperatures and times.

Stability

As mentioned before, the weak points of this coating are the Si-O-Si bonds in the backbone and between the backbone and the surface. The main task is to protect these bonds against hydrolysis.

The curing temperature and curing time can influence the chemical and thermal stability of these PDMS coatings. For different formation conditions, different stability against sodium hydroxide solution was observed in the experiments. Increasing the curing temperature from 250°C to 350°C leads to an increasing stability (see Figure 14). For the highest curing temperature, the samples show after 150 h of exposure to a hot alkaline solution (pH 10, 50°C) still a quite high water contact angle. For lower curing temperatures, the water/air contact angles decrease noticeable in time to values between 60 and 70°.

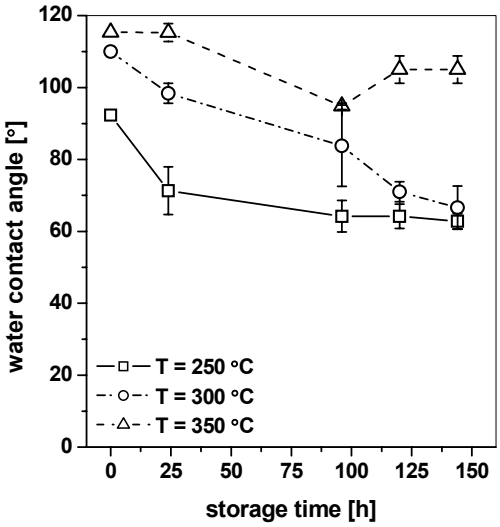

Figure 14: Effect of curing temperature on the chemical stability (PDMS conc. = 1 vol%, curing time = 15 min, NaOH solution pH = 10 & 50°C).

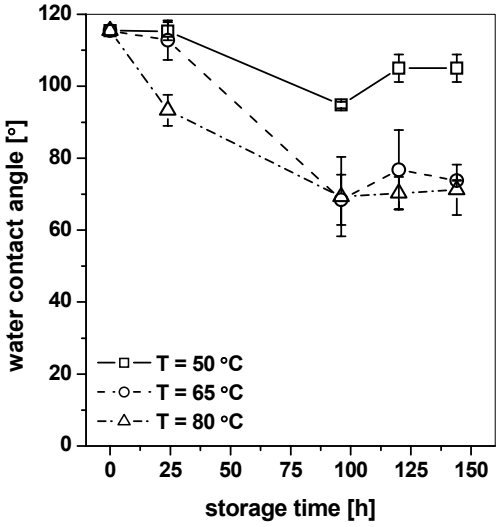

Figure 15: Effect of different sodium hydroxide solution temperatures (PDMS conc. = 1 vol%, curing time = 15 min, curing temperature = 350°C).

When increasing the sodium hydroxide solution temperatures to 65 and 80°C the samples prepared under the same conditions (1 vol% PDMS, 15 min curing time,

350°C curing temperature) show a decreasing stability as depicted in Figure 15. For both temperatures, the water contact angles are reaching values between 70 and 80°. By also increasing the curing time the stability can be improved. Table 4 summarized the results for increasing the curing time to achieve an improvement of the stability.

Table 4: Effect of curing time (1 vol% PDMS, curing temperature 350°C).

Alkaline solution temperature [°C]	Long-term stability (CA > 100°)
50	For all curing times stable for nearly 200 h
	Increasing stability with increasing curing time
65	Curing time 45 min: stable for nearly 120 h
	60 min: stable for nearly 175 h
80	Curing time 30 min: stable for nearly 150 h
	45 min: stable for nearly 175 h
	60 min: stable for nearly 175 h

The reason for this improvement might be that with increasing curing temperature more PDMS chains are covalently bonded to the surface and that the cross-linking degree increases.

2.3.2.3 Conclusions

Best results concerning hydrophobicity and stability were found for 1 vol% PDMS, 350°C and curing times above 30 min. The superfluous PDMS could be easily washed off with iso-propanol resulting in very thin films, which also prevents the blockage of pores. Most likely, linkage to the oxidized silicon nitride surface occurred until a concentration of 1 vol%. At higher concentrations the linkage between PDMS chains took place resulting in a rough and inhomogeneous film.

In general, this method provides smooth and relatively stable films. The coating material itself is food compatible. The process is easy to perform and does not require expensive equipment.

2.4 Summary

Three different types of organic-silicon based coatings were investigated and evaluated considering their hydrophobicity and stability in different aggressive environments by water contact angle measurements. Beside these features, the ability of pore blocking was considered as well. For all coatings and coating procedures the probability of pore blocking was found to be very low. Compared to the micrometer sized pores of the microsieves the coated films are extremely thin ranging from single molecular layers to several tens of nanometers.

All coatings display sufficiently high water contact angles in air as well as in hexadecane, as expected from the coating base materials.

The performed stability measurements, which are summarized in Table 5, showed an excellent stability against all used environments for the perfluorinated alkyl silane monolayer (FOTS) followed by PDMS 18, which demonstrates a sufficient resistance against hot nitric acid and hot sodium hydroxide solution. The results from the dip-coated PDMS (1 vol%, 350°C, 60 min) are comparable to the stability of PDMS 18 in hot sodium hydroxide solution. The resistance against nitric acid was not tested. However, the results from the other coatings clearly showed, that the stability in acidic environments is higher then in alkaline solutions. The OTS coating has a limited stability and performs well only under low temperatures and acidic conditions. The results for PDMS 14 are not clear. The wide scattering of the data points inhibits a clear statement about its stability.

Table 5: Summarized results of the stability evaluation.

Coating	Nitric Acid pH 5			Sodium Hydroxide pH 10		
	50°C	65°C	80°C	50°C	65°C	80°C
FOTS	++	++	++	++	++	++
OTS	+	+	-	+	-	-
PDMS 14	o	o	o	o	o	-
PDMS 18	+	+	+	+	+	+
Dip-coated PDMS	n.m.	n.m.	n.m.	+	+	+

++ : very stable; + : stable; o : medium stable; - : not stable; n.m. : not measured

2.5 Abbreviations

FODTS	perfluorinated octadecyltrichlorosilane
FOTS	perfluorinated octyltrichlorosilane
HMDSO	Hexamethyldisiloxane
ODTS	Octadecyltrichlorosilane
OTS	Octyltrichlorosilane
PES	Polyethersulfone
PDMS	Polydimethylsiloxane

2.6 References

[1] S. Schultz, G. Wagner, J. Ulrich, Chemie Ingenieur Technik 74 (2002) 901-909

[2] V. Schröder, H. Schubert, Colloids and Surfaces A 152 (1999) 103-109

[3] S.M. Joscelyne, G. Trägårdh, J. Membr. Sci. 169 (2000) 107-117

[4] V. Schröder, O. Behrend, H. Schubert, J. Colloid Interface Sci. 202 (1998) 334-340

[5] S.M. Joscelyne, G. Trägårdh, J. of Food Engineering 39 (1999) 59-64

[6] K. Kandori, in Food Processing: Recent Developments (Ed.: A.G. Ganokar), Elsevier Science (1995), Chapter 7 113-142

[7] N.C. Christov, D.N. Ganchev, N.D. Vassileva, N.D. Denkov, K.D. Danov, P.A. Kralchevsky, Colloids and Surfaces A 209 (2002) 83-104

[8] G.T. Vladisavljevic, H. Schubert, Desalination 144 (2002) 167-172

[9] I. Kobayashi, M. Yasuno, S. Iwamoto, A. Shono, K. Satoh, M. Nakajima, Colloids and Surfaces A 207 (2002) 185-196

[10] G.T. Vladisavljevic, S. Tesch, H. Schubert, Chemical Engineering Processing 41 (2002) 231-238

[11] A.J. Abrahamse, R. van Lierop, R.G.M. van der Sman, A. van der Padt, R.M. Boom, J. Membr. Sci. 204 (2002) 125-137

[12] C.J.M. van Rijn, M.C. Elwenspoek, IEEE proc. MEMS (1995) 83-87

[13] B.V. Zhmud, J. Sonnefeld, L. Bergström, Colloids and Surfaces A 158 (1999) 327-341

[14] R. Maboudian, W.R. Ashurst, C. Carraro, Tribol. Lett. 12 (2002) 95-100

[15] M.H. Hu, S. Noda, T. Okubu, Y. Yamaghuchi, H. Komiyama, Appl. Surf. Sci. 181 (2001) 307-316

[16] V.V. Tsukruk, I. Luzinov, D. Julthongpiput, Langmuir 15 (1999) 3029-3032

[17] B.C. Bunker, R.W. Carpick, R.A. Assink, M.L. Thomas, M.G. Hankins, J.A. Voigt, D. Sipola, M.P. de Boer, G.L. Gulley, Langmuir 16 (2000) 7742-7751

[18] U. Srinivasan, M.R. Houston, R.T. Howe, R. Maboudian, J. Microelectromech. S. 7 (1998) 252-260

[19] G.J. Kluth, M.M. Sung, R. Maboudian, Langmuir 13 (1997) 3775-3780

[20] M.M. Sung, G.J. Kluth, R. Maboudian, J. Vac. Sci. Technol. A 17 (1999) 540-544

[21] W.R. Ashurst, C. Carraro, R. Maboudian, W. Frey, Sens. Act. A 104 (2003) 213-221

[22] B.H. Kim, T.D. Chung, C.H. Oh, K. Chun, J. Microelectromech. S. 10 (2001) 33-40

[23] K. Iimura, T. Kato, Colloids and Surfaces A 171 (2000) 249-264

[24] M.-W. Tsao, J.F. Rabolt , H. Schönherr, D.G. Castner, Langmuir 16 (2000) 1734-1743

[25] S.R. Wasserman, Y.-T. Tao, G.M. Whitesides, Langmuir 5 (1989) 1074-1087

[26] M. D. Lechner, K. Gehrke, E. H. Nordmeier, Makromolekulare Chemie, Birkhäuser Verlag, 1993

[27] Nano and Micro Engineered Membrane Technology, Chapter 11: Membrane Emulsification, C.J.M. van Rijn, Elsevier Amsterdam, 2004 ISBN 0.444-51489-9

[28] L. Baberi, G. Kulik, H.-J. Mathieu, P. Hoffmann, Presentation, Euromat 2003, Lausanne

[29] Y.N. Xia, G.M. Whitesides, Annu. Rev. Mater. Sci. 28 (1998) 153-184

[30] T. Hayakawa, M. Yoshinari, K. Nemoto, Biomaterials 25 (2004) 119-127

[31] G. Borvon, A. Goullet, X. Mellhaoui, N. Charrouf, A. Granier, Material Science in Semiconductor Processing 5 (2003) 279-284

[32] T. Fujii, M. Hiramatsu, M. Nawata, Thin Solid Films 343-344 (1999) 457-460

[33] R.A. Lawton, C.R. Price, A.F. Runge, W.J. Doherty III, S.S. Saavedra, Colloids and Surfaces A 253 (2005) 213-215

[34] G.K. Toworfe, R.J. Composto; C.S. Adams, I.M. Shapiro, P. Ducheyne, Journal of Biomedical Materials Research A 71A (2004) 449-461

[35] M. Grionès, Inorganic and Polymeric Microsieves, PhD Thesis, University of Twente, The Netherlands, 2005

[36] H. Hillborg, U.W. Gedde, IEEE Transactions on Dielectrics and Electrical Insulations Vol. 6 No. 5 (1999) 703-717

[37] B. Janocha, D. Hegemann, C. Oehr, H. Brunner, F. Rupp, J. Geis-Gerstorfer, Surface and Coatings Technology 142 (2001) 1051-1055

[38] A. Olàh, H. Hillborg, G, Vancso, Applied Surface Science 239 (2005) 410-423

[39] A. Nakajima, K. Hashimoto, T. Watanabe, Monatshefte für Chemie 132 (2001) 31-41

[40] T. Mundry, Einbrennsilikonisierung bei pharmazeutischen Glaspackmitteln, Dissertation (1999), Humboldt Universität Berlin, Germany

Chapter 3

Tailoring surface properties to controlling droplet formation at microfluidic membranes [2]

Abstract

The preparation of water-in-oil emulsions with silicon nitride microfluidic nozzle arrays requires a surface, which is not wetted by the continuous water phase. Hence, we deposited several hydrophobic coatings on silicon nitride and studied the wetting behavior of water in pure and emulsifier containing hexadecane.

In pure medias we could demonstrate that an octyl-chain terminated is the optimal hydrophobic coating. It has a high affinity to hexadecane, due to its similar chemical nature expressed, by a very low solid/liquid interfacial tension and a low affinity to water resulting in the highest measured water in hexadecane contact angle of 164°. Unmodified silicon nitride in contrast has the highest affinity to water and the lowest to hexadecane resulting in a contact angle of 97°. Based on the determination of the solid/liquid interfacial tensions in pure liquids we found for several hydrophobic coatings and for unmodified silicon nitride a deviation from Youngs equation, which can be related to negative Hamaker constants of the studied systems.

With the soybean based emulsifier BolecMT we observed for several coatings no negative influence of the adsorbed emulsifier on the hydrophobicity. In fact, the water/hexadecane contact angles increased in time. In case of unmodified silicon nitride the surface was rendered into a more hydrophobic state. For low surface energy coatings, we observed a dramatic time dependent change of the wetting characteristics. After a certain period of time water drops collapsed and wetted the

[2] This chapter has been published as: M.J. Geerken, R.G.H. Lammertink, M. Wessling, Colloids and Surfaces A (2006) doi:10.1016/j.colsurfa.2006.06.30

surface. The time scales of the different observed wetting behaviors are several magnitudes larger than the drop formation process itself. Therefore, its relevance for the drop formation process could be neglected.

With the unmodified silicon nitride surface successful drop formation was not possible and the low surface energy coating performed successfully in membrane emulsification experiments.

3.1 Introduction

Emulsification with silicon nitride based microfluidic nozzle arrays offers the possibility to precisely control the droplet size and its distribution. These nozzle arrays – we refer to them as microsieve membranes - have a precisely defined pore size and a narrow pore size distribution, combined with a micron-sized channel length (membrane thickness) [1]. So far, silicon nitride microsieves have been used for oil-in-water emulsification [2,3]. The native hydrophilic material is wetted by the continuous phase, allowing stable emulsification.

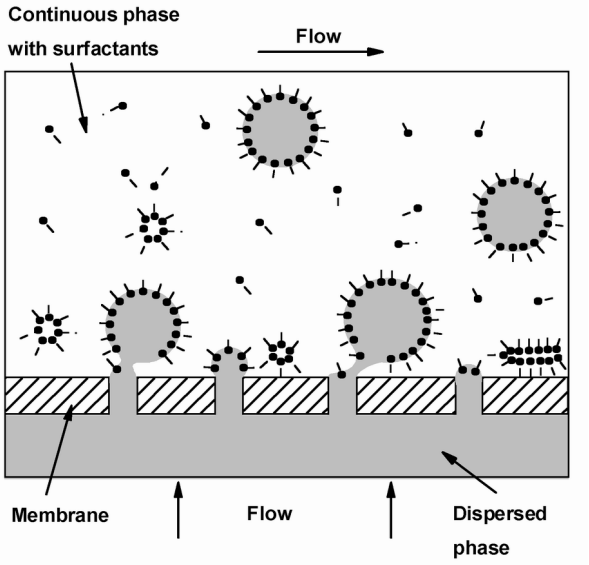

Figure 1: Schematic illustration of emulsifying water into oil with a porous membrane.

In order to produce water-in-oil emulsions with microsieves as depicted schematically in Figure 1, the surface properties need to be modified. This is illustrated in Figure 2, where water-in-oil emulsification is attempted with a hydrophobized (A) and an unmodified (B) microsieve under otherwise equal conditions. The surface (A) was hydrophobized with a perfluorinated octyltrichlorosilane (FOTS), which caused stable droplet formation at each pore. The produced drops have an average diameter of 129 ± 12 μm independent from the applied pressure. Also for an octyltrichlorosilane-modified surface the average drop

size of 113 ± 16 μm is independent from the pressure. Whereas the unmodified nozzle array (B) suffers from creeping of the dispersed phase along the solid surface, resulting in an uncontrolled droplet formation process.

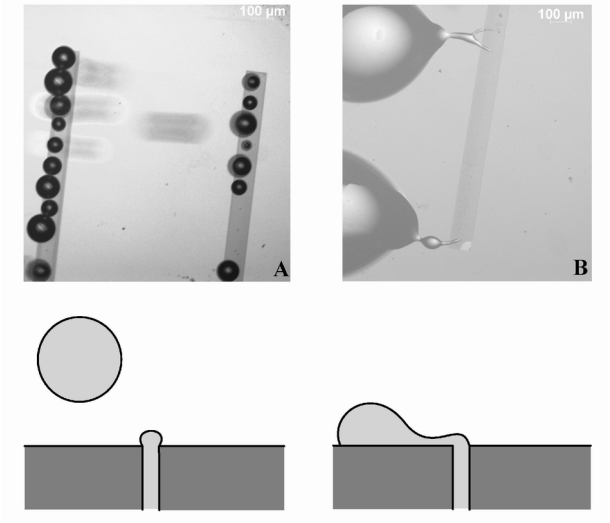

Figure 2: Emulsifying water into hexadecane containing BolecMT with a modified (A) and with an unmodified Si_xN_y microsieve (B) under the same process conditions. Below, schematic representations of the drop formation processes are shown.

It is yet unknown how exactly the interfacial properties of unmodified and hydrophobized silicon nitride in relation to the fluid properties influence the droplet formation process. The contact angle of the dispersed phase measured on the microsieve material while immersed into the continuous phase containing the relevant emulsifiers is a relevant factor. For instance, a critical contact angle necessary for a controlled emulsification is sometimes reported in literature. However, surface energies and interfacial tension phenomenas often remain unexplored. Kawakatsu et al. have reported that a successful production of water-in-oil emulsion with silicon microchannels (MC) was only possible when the water contact angle measured in the used continuous phase was higher than 120° [4].
Studies with different charged surfactants (SDS, Tween20, CTAB, TOMAC) in straight-through microchannel emulsification experiments of soybean oil in water done by Kobayashi et al. have shown that successful drop formation could only be

achieved if the static contact angle was higher than 135° [5]. In another paper, Kobayashi and co-workers showed results from the visual observation of oil droplet formation from a polycarbonate track-etch membrane in water using different emulsifiers (SDS, PGFE, Tween20, TOMAC) and at different cross-flow velocities [6]. Here, they found that at constant cross-flow velocity the oil drop size increases with decreasing contact angle. This corresponds with theoretical considerations from Christov et al. They found that at lower contact angles the three phase contact line and therefore the drop base is always larger compared to higher contact angles [7]. Thus, the drop contacts a larger area before it detaches from the membrane surface. This drop base enlargement can reach an extent that two neighboring pores feed a single droplet during the droplet formation process. This phenomenon was observed in the study of Kobayashi et al. [6]. At low cross-flow velocities the oil drop size increased from a SDS containing aqueous phase over a PFGE containing, to a Tween20 containing water phase. The contact angles of these systems decreases respectively from 106° to 102° to 95°. Stable emulsification producing oil drops in a range of 2 to 5 times the pore diameter was not possible without SDS. With the cationic surfactant TOMAC dissolved in the oil phase the membrane was fully wetted by the oil phase, also indicated by a low contact angle of 27°, and no emulsification could be achieved over the entire cross-flow velocity range. The fact that a successful emulsification could be performed with a rather low contact angle of 106° (with SDS as emulsifier) compared to the reported values mentioned above is based on the different droplet break-up mechanisms. In microchannel emulsification the droplet breaks-up is based on Laplace pressure differences and not due to shear forces as in cross-flow emulsification.

To comprehend the formation mechanism, one requires to quantify the influence of the emulsifier on both the liquid-solid and oil-water interface. For instance the use of lecithin in the production of oil-in-water emulsions with silicon based microchannel emulsification devices may turn the surface hydrophobic due to the adsorption of lecithin [8,9]. Also the use of cationic emulsifiers like TOMAC or CTAB leads to a dramatic change of the membrane wettability in case of negatively charged membrane materials like silicon or polycarbonate [5,6].

Next to the static interfacial properties, the drop formation process in microfluidic emulsification devices may be even more complex, due to its dynamic nature as interfacial properties might be differ for different time scales. Therefore, the contact angle determination in a static system might be an insufficient tool to assess whether a certain contact angle value of a given system allows successful emulsification or not. Thus, it is important to consider the dynamic interfacial tension within the system. Van der Graaf et al. reported that an increasing emulsifier bulk-concentration (Tween20) causes the drop size to decrease at constant cross-flow velocity and pressure. The drop size also increases at constant emulsifier concentration if the pressure increases [3]. These observations can be related to the adsorption rate of the emulsifier on a growing droplet. Schröder et al. found that the influence of the dispersed phase pressure becomes less as the emulsifier adsorbs faster [10]. When SDS is used as emulsifier, which is one of the fastest emulsifiers, the drop diameter is nearly independent from the applied dispersed phase pressure [10,11].

In summary, the interfacial tensions ($\gamma_{solid/continuous\ phase}$, $\gamma_{solid/dispersed\ phase}$ and $\gamma_{continuous/dispersed\ phase}$) are time dependent due to adsorption of emulsifiers on the three different interfaces. These three interfacial tensions are acting at the three phase contact point and they determine the contact angle to be formed.

In this chapter, we focus on the detailed characterization of hydrophobic coatings on silicon nitride in terms of water contact angles in air, in n-hexadecane and in emulsifier containing n-hexadecane and its time dependency. The solid surface energy of the coatings were determined and related to wetting characteristics of water/oil/emulsifier systems as well as to the emulsification performance.

3.2 Materials and Methods

Materials

N-alkanes and glycerol were purchased from Merck. Granular lecithin (> 97 % Phospholipids) was obtained from Acros Organics. The industrial soybean based emulsifier BolecMT was received from Loders Croklaan B.V., which is reported to contain approximately 40 wt% mono-, di- and tri-glycerides, 36 wt% phospholipids,

18 wt% free fatty acids and 6 wt% proteins, polysaccharides and seed residues. Water was obtained from a MilliQ® system.

For the SAM formation two types of alkyltrichlorosilanes were used. Octyltrichlorosilane (OTS) (Aldrich, 97 %) and a perfluorinated octyltrichlorosilane (FOTS) (Fluka, >97%) were used as received. For the preparation of the coating solutions, n-hexadecane (Aldrich, >99 %, < 0.005 % H_20) and chloroform (Merck, 99 %, <0,01 % H_20) were used as solvents and dried before use with molecular sieves to water content below 0.002 %.

Two different types of PDMS coatings on silicon nitride substrates were achieved from an external supplier (The Fraunhofer Institute for Manufacturing and Applied Materials Research, Bremen, Germany). Both coatings were produced by plasma polymerization of hexamethyldisiloxane (HMDSO) mixed with oxygen in different ratios. The thickness is 87 nm for PDMS 14 and 94 nm for PDMS 18, respectively. The PDMS 14 is used as an “easy-to-clean” coating for backing trays, commercialized under the trade mark ”Best Skin” and patented (WO 03/002269 A2). PDMS 18 is used as permanent mold release layer and patented (DE 10034737 A1).

Teflon like coatings were achieved from Aquamarijn Micro Filtration B.V. produced via plasma polymerization of trifluoromethane on silicon nitride substrates.

Surface modification

The SAM formation from solution took place in a mixture of dried n-hexadecane and chloroform (4/1 v/v) containing 2.5 mmol/l silane. The wafers, cleaned and oxidized using a reactive oxygen plasma (Plasmafab 508, Electrotech; 10 min, 500 W, pO_2 = 16 mbar) to remove adsorbed impurities, were placed in the solution for one hour at room temperature and ambient pressure. Afterwards the wafers were removed from the solution and extensively rinsed first with iso-propanol, then with ultra pure water and dried with nitrogen. After the formation step a stabilization step followed. Following Srinivasan et al. [12] the coated wafers were heated at 100°C for 1h in an oven flushed with nitrogen. It must be pointed out that use of dry equipment is required and that the SAM formation is carried out under a nitrogen atmosphere to

limit the water content. The same procedure was used to produce mixed monolayers of OTS and FOTS.

For the chemical vapor deposition of silane monolayers, plasma oxidized silicon nitride substrates were stored together with a few microliters of FOTS or OTS in a dry sealed glass box. The heat treatment was carried out at 120°C for 5.5 hours in a nitrogen flushed oven. Afterwards the coated samples were allowed to cool down in a desiccator.

Static contact angles

Before each measurement the substrates were washed first with tap water containing a detergent, followed by tap water, Milli-Q water, and finally with 2-propanol. After the washing step the substrates were dried first in a nitrogen stream and then at 80°C.

Static liquid/air contact angles were measured with a goniometer (OCA 15, Data Physics). Drops of one microliter Milli-Q water were formed at the needle tip and contact angles were measured 10 s after placing the drop on the substrate.

Measurements of static water/hexadecane contact angles were exploited in a self-made glass box, which was cleaned following the same procedure as used for the substrates. A one microliter Milli-Q water drop was formed at the needle tip while the needle was immersed in the hexadecane phase. To detach the water drop from the tip, the needle was moved upwards to the hexadecane/air interface. While crossing the interface the water drop detached, fell down and settled on the substrate. During a period of at least 2 hours, contact angles values were taken at defined time steps.

To observe the wetting behavior of water drops in hexadecane containing emulsifier the same procedure was used as for measuring in pure liquids. The substrates themselves were placed into the hexadecane phase at least 20 minutes before starting the observation.

Surface energy determination

The equilibrium contact angle (θ) of a liquid with a solid substrate is determined by the interfacial tensions $\gamma_{\text{liquid/vapor}}$ (γ_{LV}) - which is the surface tension of that liquid -,

$\gamma_{solid/vapor}$ (γ_{SV}) and $\gamma_{solid/liquid}$ (γ_{SL}) acting at the three phase contact point as depicted in Figure 3.

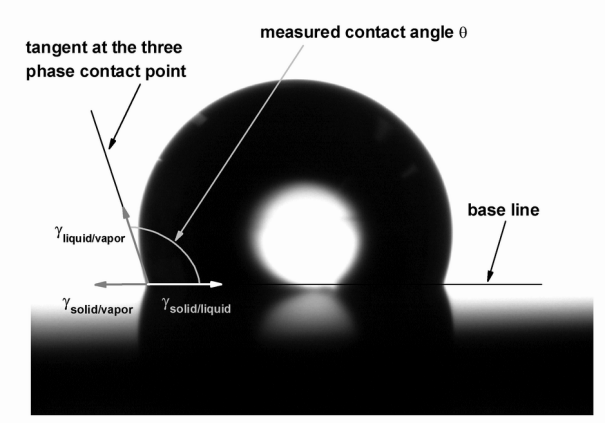

Figure 3: Image of a sessile water drop on a hydrophobic surface and the corresponding interfacial tensions forming the contact angle.

The relationship between these three interfacial tensions is given by Youngs equation (Eq. 1).

$$\cos\theta = \frac{\gamma_{solid/vapor} - \gamma_{solid/liquid}}{\gamma_{liquid/vapor}} \quad (1)$$

According to Fowkes the surface energy consists out of several additive terms representing different intermolecular forces between matters.

$$\gamma = \gamma^d + \gamma^i + \gamma^p + \gamma^\pi + \gamma^{AB} + \gamma^h + \gamma^e \quad (2)$$

The index d refers to dispersion (London), i to induced dipole-dipole (Debye), p to dipole-dipole (Keesom), π to π-bonding, AB to electron acceptor-donor, h to hydrogen bonding and e to electrostatic interactions. The first three terms being electrodynamic interactions can be combined into so-called Lifshitz-van der Waals

interactions, γ^{LW}. The other terms mainly γ^{AB} and γ^{h} are combined to Lewis acid-base interactions, γ^{AB} [13]. Equation 2 can now be rewritten into:

$$\gamma^{Total} = \gamma^{LW} + \gamma^{AB} \tag{3}$$

In order to get the surface energy of a solid surface from contact angle measurements the equation of Young and Dupré is needed, which combines the work of adhesion (W_{SL}) with measured contact angles:

$$W_{SL} = \gamma_{LV}\left(1 + \cos\theta\right) \tag{4}$$

From Berthelot's geometric mean combing rule for the work of adhesion between a solid and liquid the following expression is obtained:

$$W_{SL} = 2\left(\gamma_{LV}\ \gamma_{SV}\right)^{1/2} \tag{5}$$

Combining equation 3 to 5, an expression is obtained, which allows the calculation of solid surface energy and its components, the so-called extended Fowkes equation:

$$\gamma_{LV}\left(1 + \cos\theta\right) = 2\left(\gamma_{LV}^{LW}\ \gamma_{SV}^{LW}\right)^{1/2} + 2\left(\gamma_{LV}^{AB}\ \gamma_{SV}^{AB}\right)^{1/2} \tag{6}$$

Dividing equation 6 with $2\left(\gamma_{LV}^{LW}\right)^{1/2}$ one obtains the following equation:

$$\left(1 + \cos\theta\right)\frac{\gamma_{LV}}{2\left(\gamma_{LV}^{LW}\right)^{1/2}} = \left(\gamma_{SV}^{AB}\right)^{1/2}\left(\frac{\gamma_{LV}^{AB}}{\gamma_{LV}^{LW}}\right)^{1/2} + \left(\gamma_{SV}^{LW}\right)^{1/2} \tag{7}$$

Measuring the contact angles of two or more liquids with known Lifshitz-van-der-Waals and acid-base components on a solid, its surface energy is obtained by

plotting $\left(\frac{\gamma_{LV}^{AB}}{\gamma_{LV}^{LW}}\right)^{1/2}$ versus the left side of equation 7. From the slope one gets the acid-base component of the solid surface energy from and from the intercept the LW part.

Now, the solid/liquid interfacial tension can be calculated from the corresponding surface tensions of pure matters:

$$\gamma_{12} = \gamma_1 + \gamma_2 - 2\sqrt{\gamma_1^{AB}\gamma_2^{AB}} - 2\sqrt{\gamma_1^{LW}\gamma_2^{LW}} \tag{8}$$

Interfacial tension determination from drop shape

The so-called Bashfourth-Adams equation (9) combines the effects of gravity and interfacial tension on the shape of liquid drop [14,15]. In this equation the differential quotient $d\phi/ds$ represents the change of the angle of the tangent at a point (x_i,z_i) with the x-axis if the arc length s is changed as depicted in Figure 4. Bo is the Bond number, which represents the ratio of gravity force to interfacial force.

$$\frac{d\phi}{ds} = 2 + Bo\, z - \frac{\sin\phi}{x} \tag{9}$$

$$Bo = \frac{\Delta\rho\ \ g\ R_{Apex}^2}{\gamma} \tag{10}$$

Unfortunately, the Bashfourth-Adams equation has no analytical solution and a numerical solution pathway has to be used. With the obtained Bond-Number the actual interfacial tension of the experimental drop shape can be calculated. Experimental drop coordinates were achieved by using the imaging program Scion Image®. The Bashfourth-Adams equation was numerically solved for each drop shape using MathLab®.

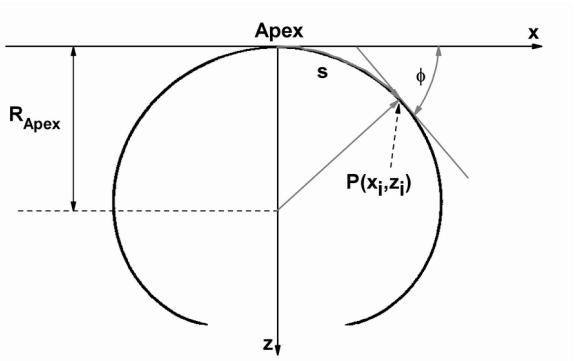

Figure 4: Parameters and drop coordinates of a sessile drop needed for using the Bashfourth-Adams equation. The shown drop profile is an experimental one extracted from a drop image.

3.3 Results and Discussion

Contact angles in pure liquids

Table 1 displays the water/air and water/hexadecane contact angles for the different substrates used in this study. The most hydrophobic coatings here are the fluorinated silane monolayers (FOTS), followed by the corresponding alkyl silane monolayer (OTS). From PDMS 18 to PDMS 14 the amount of oxygen used during the coating deposition is higher for the latter one. This results obviously in a lower water/air contact angle. The measured water/air contact angles for both PDMS types are comparable with reported values ranging from 75 to 105° depending on polymerization parameters and conditions [16,17].

The contact angle for the “Teflon-like” coating is quite low. Teflon (Polytetrafluoroethylene) is known to be a hydrophobic material. Commercial Teflon shows water/air contact angles from 100 to 115° [18-20], which corresponds to own measurements done on a commercial, hot-pressed PTFE plate. Plasma polymerized fluorocarbon films based on tetrafluoroethylene (TFE) or trifluoromethane (TFM) showing water contact angles between 100 and 110° [21,22].

The order found for water/air contact angles (see Table 1) is not observed for water/hexadecane contact angles. Here, the alkyl silane monolayer and PDMS18

have higher contact angles compared to both fluorinated monolayers. This can only be explained if all three interfacial tensions are known, which is the issue in the following section.

Table 1: Results of the contact angle measurements in air and in n-hexadecane as the surrounding phase.

Surface	Water/air CA [°]	Water/n-hexadecane CA [°]
Silicon nitride	65.1 ± 4.3	97.0 ± 1.4
Teflon A	89.1 ± 4.3	132.5 ± 0.4
PDMS 14 [1]	93.5 ± 0.9	137.0 ± 5.7
PDMS18 [1]	103.4 ± 1.8	153.0 ± 0.5
CVD-OTS	104.0 ± 2.3	163.6 ± 1.1
S-FOTS	112.0 ± 4.0	148.9 ± 3.9
CVD-FOTS	114.0 ± 1.2	144.9 ± 0.4
PTFE [2]	114.5 ± 0.9	160.4 ± 2.2

S-: solution made; CVD-: chemical vapor deposition; 1: plasma deposited PDMS; 2: hot-pressed PTFE plate

Surface energy of the solids

In order to obtain the solid free energy of each substrate, contact angles of liquids with known surface tensions (taken from [13]) were measured. From equation 7 the surface free energy and its AB and LW parts can be obtained. The results for Teflon A are shown in Figure 5. For all evaluated coatings the results are shown in Table 2.

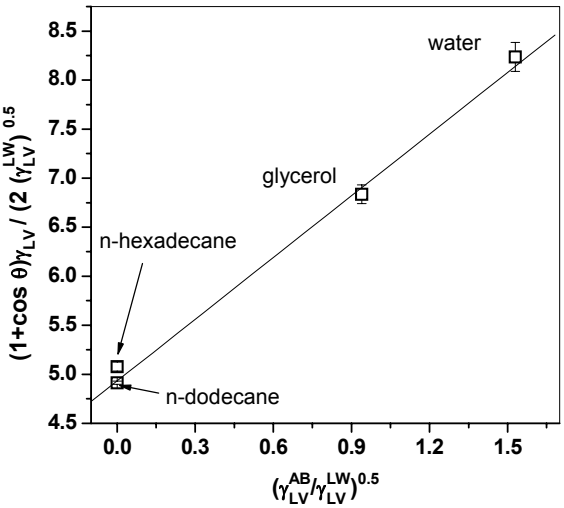

Figure 5: Determination of the surface energy and its components of Teflon A using water, glycerol, n-dodecane and n-hexadecane as test liquids.

Table 2: Detailed results of the surface energy determination.

Substrate	γ^{LW} [mN/m]	γ^{AB} [mN/m]	γ^{Total} [mN/m]	Surface Polarity [%]
S-FOTS	10.11 ± 0.84	0.62 ± 0.13	10.73 ± 1.36	5.80
CVD-FOTS	11.49 ± 1.02	0.51 ± 0.15	12.0 ± 1.65	4.22
PTFE	19.17 ± 0.23	0.02 ± 0.01	19.18 ± 0.24	0.10
PDMS 18	22.84 ± 0.26	0.88 ± 0.03	23.72 ± 0.42	3.70
PDMS 14	24.89 ± 0.35	2.36 ± 0.07	27.25 ± 0.59	8.65
CVD-OTS	26.17 ± 0.29	0.18 ± 0.02	26.35 ± 0.43	0.70
Teflon A	24.33 ± 0.6	4.45 ± 1.16	28.78 ± 2.48	15.47
Si_xN_y	11.72 ± 2.29	28.92 ± 4.12	40.63 ± 1.89	71.19

For CF_3 terminated surfaces reported values for the surface energy are in the range of 6 to 13 mN/m [23-25]. Based on the contact angle data of water, hexadecane and methylene iodide on OTS coated surfaces from Fadeev et al. the total surface

energy is calculated to 27.15 mN/m (γ^{AB} = 0.31 mN/m) for CVD-OTS and 29.36 mN/m (γ^{AB} = 1.70 mN/m) for a solution-made OTS [26]. In literature the total surface energy reported for PDMS varies in a range from 20 to 27 mN/m, which fits well to the data measured here [27,28]. The wide range of surface energies reported for PDMS is probably due to different oxygen contents in different PDMS solid surfaces. Surface oxidation experiments showed that the total surface energy increases with increasing amount of oxygen present as silanol groups (Si-OH) at the surface [29].
The surface energy of Teflon A (27.93 mN/m) is higher than expected. However, this coating is a “Teflon like” coating produced by plasma polymerization of trifluoro-methane. The structure should not be necessarily the same as PTFE having CF_2-CF_2 repeat units. The total surface energy is more comparable with the one of Polytrifluoroethylene (PTriFE), which is approximately 28 mN/m [30]. For PTFE the surface energy of 19.18 mN/m fits to reported values.
From the solid surface energies and the surface tensions of water and hexadecane the interfacial tension between solid/water and solid/hexadecane were calculated using equation 8. Table 3 shows the obtained values. Now, the influence of the surrounding media on the water contact angle (Table 1) can explained by the quite different interfacial tensions between the coatings and hexadecane. OTS shows a very small $\gamma_{\text{solid/hexadecane}}$ of 0.2 mN/m whereas the value for FOTS is twenty times larger. The OTS coating is an octyl-chain terminated surface and thus chemically similar to hexadecane. The solid/water interfacial tensions of both coatings are nearly equal. According to the theory this must result in a higher contact angle on OTS. All measured water/air contact angles are in agreement with Youngs equation as depicted in Figure 6 as well as with the approach of Kwok et al. [30].
A similar approach was applied to the measured water/hexadecane contact angles. Theoretical contact angles were obtained by calculations according to equation 8, using the interfacial tension of water/hexadecane and the values for the solid/liquid interfacial tensions from Table 3. Here, the agreement with Youngs equation was poor as depicted in Figure 7. Only the data points for PTFE and CVD-FOTS are in agreement with the theory.

Table 3: Interfacial tensions of the studied surfaces with n-hexadecane and water calculated via equation 8.

Solid substrate	γ_{SL} [mN/m] hexadecane	γ_{SL} [mN/m] water
CVD-OTS	0.20 ± 0.03	45.26 ± 0.36
PTFE	0.73 ± 0.03	49.41 ± 0.82
PDMS 18	1.08 ± 0.08	38.52 ± 0.40
PDMS 14	2.41 ± 0.12	31.54 ± 0.53
CVD-FOTS	3.91 ± 0.99	43.12 ± 2.85
Teflon A	4.54 ± 1.58	25.65 ± 3.90
S-FOTS	4.84 ± 0.95	42.67 ± 2.42
Si_xN_y	32.15 ± 1.62	4.66 ± 5.59

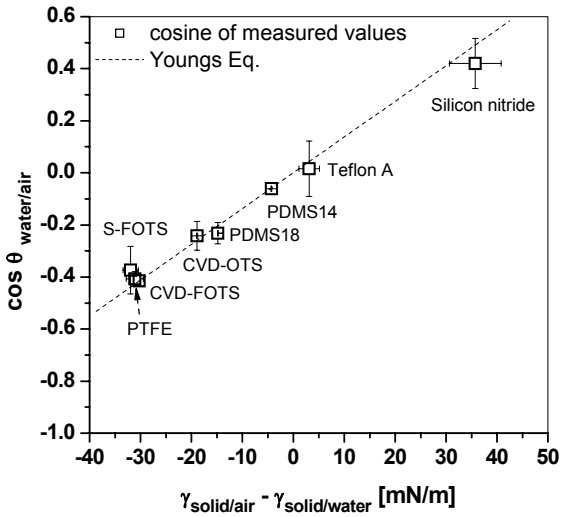

Figure 6: Comparison of measured and calculated water/air contact angles. The solid/water tensions are taken from Table 3 and the solid/air tensions are taken from Table 2. The water surface tension was assumed to be 72.8 mN/m.

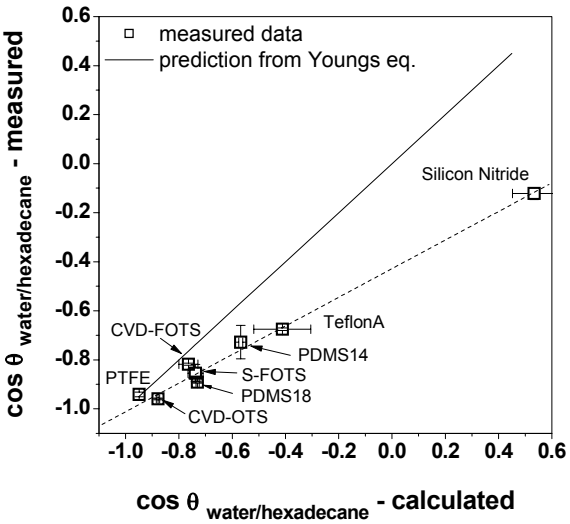

Figure 7: Comparison of measured and calculated water/hexadecane contact angles. The water/hexadecane interfacial tension was assumed to 51.3 mN/m.

A thin hexadecane film between the water drop and the solid surface can explain the mismatch between the theoretical and measured water/hexadecane/solid contact angles. If this is the case the interaction between the water and the solids across the hexadecane must be repulsive. To prove this hypothesis we apply the theory of van-der-Waals surface forces. Within this framework, the Hamaker constant A_{132} quantifies if two bodies in a given system are attracting or repulsing each other. In case of repulsion A_{132} must be negative and a stable thin film can be present. In principle the Hamaker constant of a three phase system A_{132} can be obtained by either using the approach of Hamaker, which uses a combining rule to obtain A_{132} from the Hamaker constants of the pure phases A_{ii} or by the Lifshitz theory [31]. The first one should not be used when liquids with high dielectric constants like water are involved [32]. Within the latter the A_{132} is obtained from the bulk properties refractive index (n_i) and dielectric constant (ε_i) of the involved materials. An approximate value of A_{132} can be achieved with equation 11. In this equation k is the Boltzman constant ($1.38066*10^{-23}$ J K^{-1}), h is the Planck constant ($6.626 * 10^{-34}$ J s) and $\nu_{e,i}$ is the main

adsorption frequency of UV-light (s^{-1}). The index 1 refers to the solid substrate, 2 to the drop phase (water) and 3 to the intermediate phase (n-hexadecane).

$$A_{132} \approx \frac{3}{4}kT\left(\frac{\varepsilon_1-\varepsilon_3}{\varepsilon_1+\varepsilon_3}\right)\left(\frac{\varepsilon_2-\varepsilon_3}{\varepsilon_2+\varepsilon_3}\right)+ \frac{3h\upsilon_e}{8\sqrt{2}}\frac{\left(n_1^2-n_3^2\right)\left(n_2^2-n_3^2\right)}{\left(n_1^2+n_3^2\right)^{1/2}\left(n_2^2+n_3^2\right)^{1/2}\left\{\left(n_1^2+n_3^2\right)^{1/2}+\left(n_2^2+n_3^2\right)^{1/2}\right\}} \quad (11)$$

For the calculation of A_{132} the refractive indices and dielectric constants are needed. In Table 4 the used data and the calculated Hamaker constants are shown as well as the differences between the calculated and measured cosine of the water/hexadecane contact angles.

Table 4: Calculated Hamaker constants and the corresponding data.

	Refractive Index n_i	Dielectric Constant ε_i	Adsorption Frequency [10^{15} 1/s] $\nu_{e,i}$	A_{132} [10^{-20}J]	Δ cosine water/n-hexadecane CA
water	1.333[a]	80[a]	3[a]		
n-hexadecane	1.423[a]	2.05[a]	2.9[a]		
PTFE	1.359[a]	2.1[a]	2.9[a]	0.158	0.007
CVD-OTS[b]	1.5[a]	2.25[a]	3[a]	-0.168	0.081
PDMS 18	1.5[c]	3.1[c]	3	-0.123	0.161
PDMS 14	1.47[c]	3[c]	3	-0.057	0.16
Si_xN_y	2.01[d]	6.5[d]	3	-1.093	0.656

a) data taken from [32]; b) assumed to be equal to crystal hydrocarbon; c) data taken from [34]; d) data taken from [33]

For PTFE and silicon nitride the refractive indices and the dielectric constants were available from literature. Unfortunately, for CVD-OTS and both PDMS coatings the values were not known. Nevertheless, for CVD-OTS both were assumed to be equal to a crystal hydrocarbon surface. For PDMS coatings produced via plasma polymerization of HMDSO calculations were carried out for two cases based on literature values for the refractive index and dielectric constant [34].
Table 4 indeed relates the discrepancy of the measured contact angles from Youngs equation to negative Hamaker constants, suggesting repulsive systems. Hence, a thin films of n-hexadecane can be present between the water drop and the solid substrate. An attractive system having a positive A_{132} should give no mismatch between measured and calculated values like represented by PTFE.

Wetting behavior of the substrates in emulsifier containing environments

Beside the surface properties in pure environments, it is important to study the wetting behavior of hydrophobic substrates in an emulsifier containing continuous oil phase. It is essential to determine the effects of adsorbed emulsifiers on the wettability of the hydrophobic substrates and to which extend a change of the hydrophobicity still allows successful emulsification.
Here, we show at first the results of water contact angle studies on CVD-OTS, PDMS 14, PDMS 18 and silicon nitride in 0.1 wt% BolecMT containing hexadecane. The contact angles are not negatively changed due to the presence of the used emulsifier. In fact, the contact angles of both PDMS coatings and for silicon nitride even increased by the adsorption of the emulsifier. From the contact angles of the pure liquids (see Table1) the contact angles increase in the first 2 minutes by 12 %, 24 %, 37 % for PDMS18, PMDS14 and silicon nitride. After 10 to 20 minutes the water CA stays constant at 170.4 ± 1.9° for CVD-OTS, 169.2 ± 2° for PDMS14 and 171.2 ± 0.9° for PDMS 18. For silicon nitride in contrast, the CA increases from around 130° to 160° reached after more than 2 hours. In general, the wetting properties are now defined by the adsorbed emulsifier and not by the underlying solid surface.

One can also observe a significant drop flattening as shown by drop profiles in Figure 8 for proceeding time. Figure 9 plots the drop aspect ratio, which is the ratio of the drop height to the maximum drop diameter, as a function of time. Initially, the drop shape remains constant for approximately 30 minutes and then decreases.

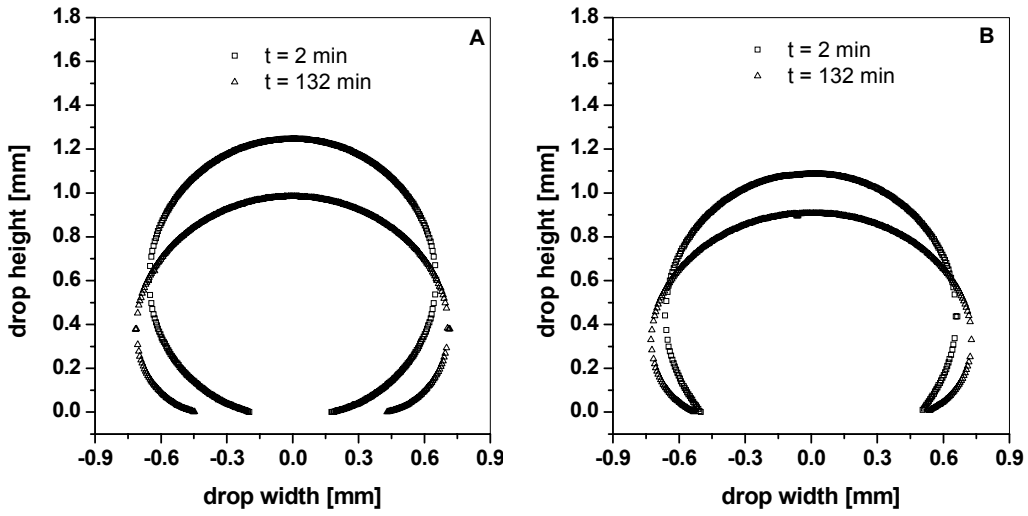

Figure 8: Profiles of 1μl drops of MilliQ-water on two different substrates (A: CVD-OTS, B: Si_xN_y) and at different time steps in hexadecane containing 0.1 wt% BolecMT.

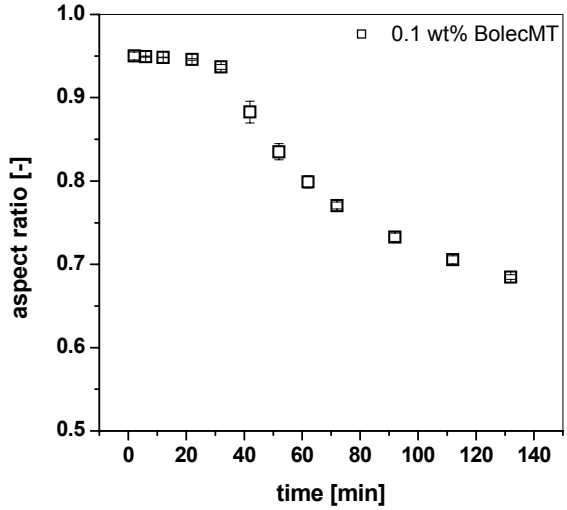

Figure 9: Aspect ratio evolution of water drops placed on CVD-OTS substrate surrounded by hexadecane containing 0.1 wt% BolecMT.

The reason for the drop flattening is the decrease of the water/oil interfacial tension in time. This can be calculated from the drop shape solving the Bashfourth-Adams equation. At relative high interfacial tensions the drop shape is stabilized against the gravity force. After the interfacial tension has reached a certain value the effect of the gravity starts to act. In Figure 10 the interfacial tension decline is shown for water drops on CVD-OTS and on both PDMS coatings in hexadecane containing 0.1 wt% BolecMT. A significant drop deformation sets in after 30 min corresponding to an interfacial tension of around 10 mN/m and is independently from the used substrates.

The interfacial tension decline shows a two-step behavior. The curve shows an S-shape rather than a “normal” dynamic interfacial tension decline curve for low molecular weight surfactants. Similar S-shaped dynamic interfacial tension curves can be found for protein-lipid mixtures. Miller et al. reported this for β-lactoglobuline adsorbed from aqueous solution and α-dipalmitoyl phosphatidylcholine from chloroform at the water/chloroform interface [35]. Wu et al. observed the same for several other proteins and phospholipids [36]. Beside this, it can be seen that

BolecMT is a very slow adsorbing emulsifier. The equilibrium interfacial tension is reached after more than 90 minutes.

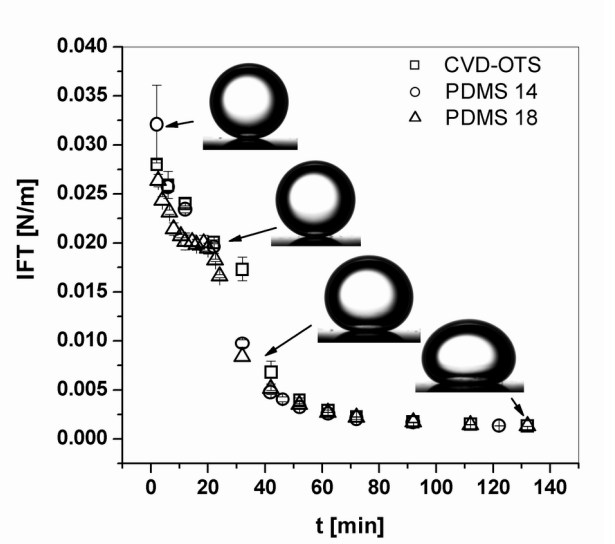

Figure 10: Dynamic interfacial tension of water/hexadecane + 0.1 wt% BolecMT determined via drop shape analysis of sessile water drops on three different substrates.

During this flattening process, the drop/solid contact area changes in case of the hydrophobic coatings whereas for silicon nitride almost no change can be seen. In the beginning the radius of the contact area on silicon nitride is 2.5 times larger than on all other tested substrates, which is the consequence of the lower contact angle. Figure 11 depicts the relative change of the drop base radius in time. The rate of the increasing drop base radius goes down from PDMS18 over CVD-OTS and PDMS 14 to silicon nitride. This order corresponds to the solid surface energy of the substrates (see Table 2).

Water drops on modified substrates often moved during the measurements at tilt angles below 1 degree. This movement was independent from the actual drop shape and was observed for round and flat drops as well. Either extreme low adhesion forces are present or a thin film of hexadecane as a lubricant is in between the drop and the substrate. Water drops placed on silicon nitride under the same conditions were not moving. Even at a tilt angle of 9 degree the drops did not slide.

Here, the adhesion between the water drops and the solid surface seem to be higher.

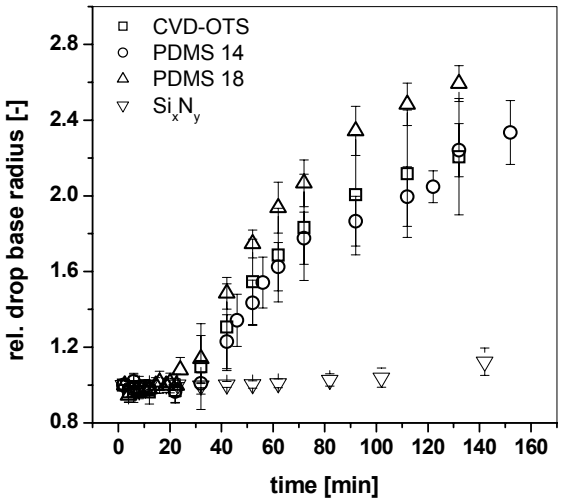

Figure 11: Relative radius of the drop/solid contact area versus time.

We further observed the phenomenon of total water drop collapse on FOTS coated substrates. As for the other coatings the contact angle stayed constant in the first minutes, but then the drops suddenly started to spread over the surface resulting in a very low contact angle in a range of 20 to 40° as it is shown in Figure 12. This behavior was observed in several experiments with different emulsifier concentrations. Without emulsifier the contact angle remained constant over the full experimental time scale.

The collapse mostly occurred after 20 to 30 minutes. The process itself was quite fast and took place within a few seconds. In contrast to the flat drops, the collapsed ones were not moving when the substrate was tilted or moved. They stuck to the surface and could only be removed by washing with water and cleaning solutions. Here, a strong adhesion between the collapsed water drops and the FOTS coated surface is present, which is promoted by one or more of the adsorbed ingredients of BolecMT.

The collapse of water drops in a BolecMT containing environment was also observed on mixed monolayers of different FOTS and OTS molar ratios. The solid

surface energy of these mixed silane monolayers was lower than 15 mN/m. The next substrate tested was commercial PTFE (γ_{sv} = 19 mN/m), which was hot-pressed before used in order to obtain a smooth surface. Here, no drop collapse was observed, even not at a six times higher BolecMT concentration.

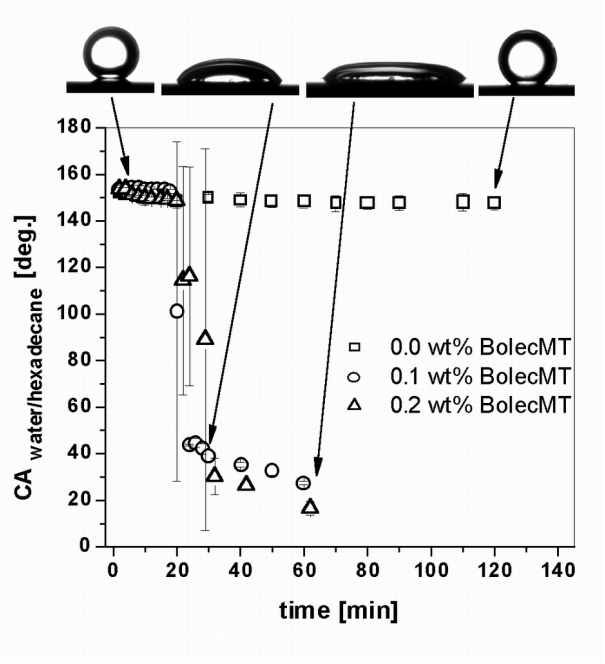

Figure 12: Collapsing water drops on a FOTS coated surface in hexadecane with different concentrations of BolecMT.

Similar experiments were carried out with lecithin containing solutions. No sudden drop collapse was observed. Figure 13 presents the results of the contact angle measurements, the drop flattening expressed by the aspect ratio and the interfacial tension decrease for lecithin dissolved in the n-hexadecane phase. The evolution of the CA is comparable to results achieved with BolecMT on OTS and PDMS. A different behavior can be observed for the aspect ratio. Here, a significant drop deformation can already be seen after 10 minutes due to a faster interfacial tension decline.

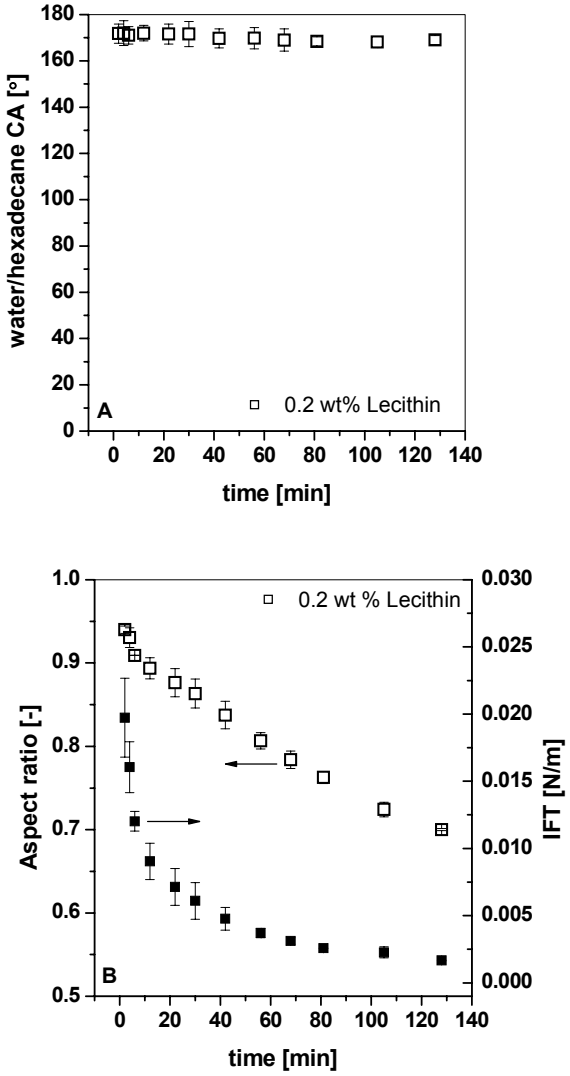

Figure 13: Contact angle evolution (A), aspect ratio evolution of water drops (open symbol) and interfacial tension decline (filled symbols) on FOTS (B) if lecithin dissolved in n-hexadecane is used.

The shape of the interfacial tension development is different compared to BolecMT. To illustrate this more in detail, Figure 14 depicts a plot of $IFT_{(t)} - IFT_{(eq.)}$ versus $t^{-1/2}$ showing the decrease of the interfacial tension for 0.2 wt% lecithin and 0.6 wt% BolecMT. The latter has approximately the same phospholipid content as 0.2 wt%

lecithin. In case of lecithin the decline follows a square root relationship according to equation 12 over all data points whereas BolecMT does not.

$$\gamma(t) - \gamma_{eq.} = \frac{RT\,\Gamma_c^2}{C_0}\sqrt{\frac{\pi}{4D\,t}} \qquad (12)$$

Equation 12 is a simplified version of the equation of Ward and Tordai relating the interfacial tension decline with the surfactant bulk concentration C_0, the adsorbed emulsifier density Γ_c and the diffusion coefficient D [37]. The non-linearity of the dynamic interfacial tension of the emulsifier BolecMT is due to the complex mixture of BolecMT resulting in a competitive adsorption at the liquid-liquid interface.

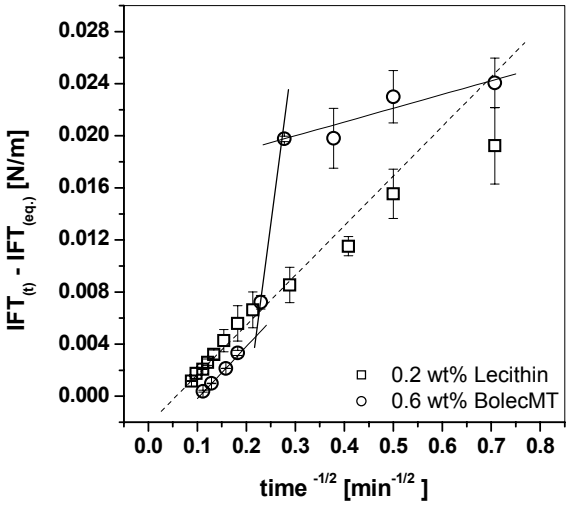

Figure 14: Dynamic interfacial tension of 0.2 wt% Lecithin and 0.6 wt% BolecMT in n-hexadecane plotted according to equation 12. The equilibrium interfacial tension was assumed to be 0.0005 N/m.

At this point, we summarize that the collapse only occurs if BolecMT is used as an emulsifier in combination with substrates having a solid surface energy up to 15

mN/m and it is assumed that the proteins present in BolecMT are responsible for the change of the wetting behavior.

In the literature, only the adsorption of proteins from aqueous solutions on various solid surfaces is reported. In general, the adsorption of proteins is strongly related to the hydrophobicity of the solid substrates. According to the adsorption behavior proteins can be distinguish into “hard” and “soft” proteins. So-called “soft” proteins, like BSA, IgG, and alpha-lactoalbumine, have less internal stability and they adsorb nearly on all solid surfaces. On hydrophobic substrates this type of proteins show a change of their conformation to a great extend [38]. “Hard” proteins (lysozyme, beta-lactoglobuline), which have a higher internal stability, adsorb weakly on hydrophilic substrates but strongly on hydrophobic ones while undergoing structural changes [39,40].

The mechanism of the drop collapse is assumed to be an unfolding process of the adsorbed proteins combined with the penetration of hydrophilic chains of the unfolded protein into the water phase. The ability of proteins to penetrate into adsorbed lipid layers is a known process [41]. In a lipid-protein system one observable effect of penetrating proteins is the formation of aggregates on water/oil interfaces. In literature, Zhao et al. and Heertje et al. observed the formation of aggregates in protein-phospholipid containing systems. The latter one used a similar emulsifier named BolecZ [42]. Zhao et al. stated that the aggregates are condensed phospholipids formed under the action of proteins penetrating into the phospholipid monolayers present at the interface. A distinguishing condition between their work and the one presented here is that in this work the phospholipids and the proteins are present in the same phase and not in two separated phases [43]. Pautot et al. also observed spontaneous emulsification and formation of aggregates at the interface of a water/dodecane/phospholipid system [44].

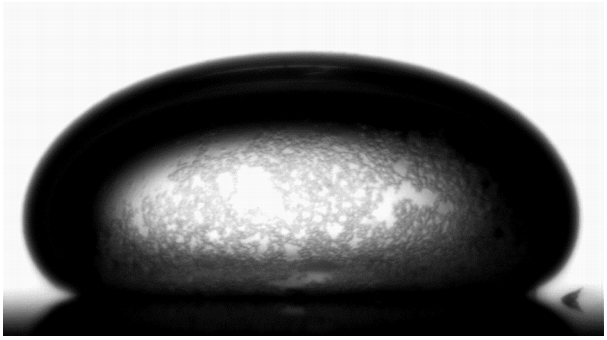

Figure 15: Aggregates on the water/hexadecane interface.

In Figure 15 a picture of water/hexadecane interface after 16 hours is shown. It can be clearly seen, that aggregates have been formed on the interface. First aggregates were observed after approx. 90 minutes.

3.4 Conclusions

A variety of hydrophobic coatings on silicon nitride were studied. All coatings showed high water contact angles if measured in air, n-hexadecane, and emulsifier containing n-hexadecane. The highest water/air contact angle was achieved with the fluorinated alkylsilane FOTS followed by the non-fluorinated OTS. If measured in n-hexadecane the order is changed. Here, OTS showed a higher value than the fluorinated alkylsilane. This could be explained by the solid surface energies and the interfacial tensions between the coatings and both liquids.

The contact angles measured in air have the same values and the same order as predicted by Youngs equation. Whereas the theoretical water/hexadecane contact angles are lower than the experimental ones. The disagreement between the measured values and the calculated values is explained with the existence of a thin hexadecane film between the water drop and the solid surface. A stable thin film can be formed if the interaction in the three-phase system is repulsive. The Hamaker constant showed that in case of silicon nitride, CVD-OTS and PDMS a repulsive system is present indicated by a negative Hamaker constant. A positive constant is

obtained for PTFE, indicating a stable PTFE/water interface, and resulting in a correct prediction by Youngs equation.

The wetting studies with the emulsifier BolecMT showed that the hydrophobicity is negatively influenced for FOTS. Here, the adsorbed phospholipids and proteins generate a hydrophilic contact area resulting in an abrupt water drop collapse. We attribute this to the ability of proteins to unfold and present their hydrophilic parts towards the water. The unfolding process itself might be induced by the very low surface energy of FOTS. In fact we found the drop collapse on several coatings that have a surface energy below 15 mN/m.

The determination of the dynamic interfacial tension showed that BolecMT is a very slow adsorbing emulsifier and that the interfacial tension decline is somehow a two stage process similar to observation for the adsorption of proteins and phospholipids at water/oil interfaces.

The drop formation in membrane emulsification is a quite fast process and takes place in milliseconds. This is indeed faster than all dynamic wetting processes shown here, where the first contact angle measurements are conducted after 2 minutes. To relate results of emulsification experiments to static contact angles it would be more appropriate to correspond to contact angles measured with pure phases. This situation seems to be closer to the real system of a drop inflating from a pore. The emulsifier will not significantly affect the continuous/dispersed and dispersed/solid interfaces as long as its adsorption rate is rather slow compared to the drop formation time. The interfacial tension between the solid and the continuous phase, however, is affected because it is a stationary interface saturated with emulsifiers. Reducing this interfacial tension can only result in an increased contact angle.

We could demonstrate successful water-in-oil emulsification with hydrophobized silicon nitride microsieves. Additionally, we found that the changes of the wetting characteristic under the action of a slow adsorbing emulsifier are not relevant for the emulsification performance.

3.5 Acknowledgements

The work was sponsored by the European Union (Thames Project; QLRT 2000-01228). Microsieve membranes were kindly provided by Aquamarijn B.V.

3.6 Abbreviations

CA	Contact angle
CTAB	Cetyltrimethylammonium bromide
CVD	Chemical vapor deposition
FOTS	perfluorinated octyltrichlorosilane
HMDSO	Hexamethyldisiloxane
IFT	Interfacial tension
MC	Microchannel
OTS	Octyltrichlorosilane
PDMS	Polydimethylsiloxane
PGFE	Polyglycerol fatty acid ester
PTFE	Polytetrafluoroethylene
PTriFE	Polytrifluoroethylene
SAM	Self-assembled monolayer
SDS	Sodium dodecylsulfate
TFE	Trifluoroethylene
TFM	Trifluoromethane

3.7 References

[1] C.J.M. van Rijn, W. Nijdam, WO0218058, Publication date: 7 March 2002

[2] A.J. Gijbersten-Abrahamse, A. van der Padt, R.M. Boom, J. Membr. Sci. 230 (2004) 149-159

[3] S. van der Graaf, C.G.P.H. Schroën, R.G.M. van der Sman, R.M. Boom, J. Colloid Interface Sci. 277 (2004) 456-463

[4] T. Kawakatsu, G. Trägårdh, Ch. Trägårdh, M. Nakajima, N. Oda, T. Yonemoto, Colloids and Surfaces A 179 (2001) 29-37

[5] I. Kobayashi, M. Nakajima, S. Mukataka, Colloids and Surfaces A 229 (2003) 33-41

[6] I. Kobayashi, M. Yasuno, S. Iwamoto, A. Shono, K. Satoh, M. Nakajima, Colloids and Surfaces A 207 (2002) 185-196

[7] N.C. Christov, D.N. Ganchev, N.D. Vassileva, N.D. Denkov, K.D. Danov, P.A. Kralchevsky, Colloids and Surfaces A 209 (2002) 83-104

[8] S. Sugiura, M. Nakajima, J. Tong, H. Nabetani, M. Seki, J. Colloid Interface Sci. 227 (2000) 95-103

[9] J. Tong, M. Nakaijma, H. Nabetani, Eur. J. of Lipid Sci. Technol. 104 (2002) 216-221

[10] V. Schröder, H. Schubert, Colloids and Surfaces A 152 (1999) 103-109

[11] M. Yasuno, M. Nakajima, S. Iwamoto, T. Maruyama, S. Sugiura, I. Kobayashi, A. Shono, K. Satoh, J. Membr. Sci. 210 (2002) 29-37

[12] U. Srinivasan, M. R. Houston, R. T. Howe, R. Maboudian, J. Microelectromech. S. 7 (1998) 252-260

[13] B. Janczuk, T. Bialopiotrowicz, A. Zdziennicka, J. Colloid Interface Sci. 211 (1999) 96-103

[14] O.I. del Rio, A.W. Neumann, J. Colloid Interface Sci. 196 (1997) 136-147

[15] C. Huh, R.L. Reed, J. Colloid Interface Sci. 91 (1983) 472-484

[16] B. Janocha, D. Hegemann, C. Oehr, H. Brunner, F. Rupp, J. Geis-Gerstorfer, Surface and Coatings Technology 142 (2001) 1051-1055

[17] T. Hayakawa, M. Yoshinari, K. Nemoto, Biomaterials 25 (2004) 119-127

[18] D. Gan, W. Cao, Z. Wang, J. of Fluorine Chemistry 116 (1) (2002) 59-63

[19] Y. Inoue, Y. Yoshimuro, Y. Ikeda, A. Kohno, Colloids and Surfaces B 19 (2000) 257-261

[20] J.C. Caro, U. Lappan, F. Simon, D. Pleul, K. Lunkwitz, European Polymer Journal 35 (6) (1999) 1149-1152

[21] R. Prat, Y.J. Koh, Y. Babukutty, M. Kogoma, O. Okazaki, M. Kodama, Polymer 41 (20) (2000) 7355-7360

[22] B.K. Smith, J.S. Sniegowski, G. LaVigne, C. Brown, Sensors and Actuators A 70 (1998) 159-163

[23] S-H. Lee, M-J. Kwon, J-G. Park, Y-K. Kim, H-J. Stin, Surface and Coatings Technology 112 (1999) 48-51

[24] G. Jaenchen, L. Barbieri, P. Hoffmann, Imaging and Applied Optics, DMT-IOA, EPFL Lausanne, May 2002

[25] M.K. Chaudhury, Materials Science and Engineering R16 (1996) 97-159

[26] A.Y. Fadeev, T.J. McCarthy, Langmuir 16 (2000) 7268-7274

[27] H. Hillborg, N. Tomczak, A. Olah, H. Schönherr, G.J. Vansco, Langmuir 20 (2004) 785-794

[28] A. Galliano, S. Bistac, J. Schultz, J. Colloid Interface Sci. 265 (2003) 372-379

[29] V.M. Graubner, R. Jordan, O. Nuyken, B. Schnyder, T. Lippert, R. Kötz, A. Wokaun, Macromolecules 37 (2004) 5936-5943

[30] D.Y. Kwok, A.W. Neumann, Adv. Colloid Interface Sci. 81 (1999) 167-249

[31] R. Correa, B. Saramago, J. Colloid Interface Sci. 270 (2004) 426-435

[32] Jacob Israelachvili, Intermolecular & Surface Forces, 2nd Ed., Academic Press, 1991

[33] L. da Silva Zambom, R. Domingues Mansano, R. Furlan, Vaccum 65 (2002) 213-220

[34] G. Borvon, A. Goulet, X. Mellhaoui, N. Charrouf, A. Granier, Material Science in Semiconductor Processing 5 (2003) 279-284

[35] R. Miller, V.B. Fainerman, A.V. Makievski, J. Krägel, D.O. Grigoriev, V.N. Kazakov, O.V. Sinyachenko, Adv. Colloid and Interface Sci. 86 (2000) 39-82

[36] J. Wu, J.B. Li, J. Zhao, R. Miller, Colloids and Surfaces A 175 (2000) 113-120

[37] B.B. Niraula, T.K. Chun, H. Othman, M. Misran, Colloids and Surfaces A 248 (2004) 157-166

[38] T. Maruyama, S. Katoh, M. Nakajima, H. Nabetani, T.P. Abbott, A. Shono, K. Satoh, J. Membr. Sci. 192 (2001) 201-207

[39] K. Nakanishi, T. Sakiyama, K. Imamura, J. of Bioscience and Bioengineering 91(3) (2001) 233-244

[40] J.R. Lu, T.J. Su, P.N. Thirtle, P.K. Thomas, A.R. Rennie, R. Cubitt, J. Colloid Interface Sci. 206 (1998) 212-223

[41] D. Vollhardt, V.B. Fainerman, Adv. Colloid and Interface Sci. 86 (2000) 103-151

[42] I. Heertje, H. van Aalst, J.C.G. Blonk, A. Don, J. Nederhof, E.H. Lucassen-Reynders, Lebensm.-Wiss. und Technol. 29 (1996) 217-226

[43] J. Zhao, D. Vollhardt, G. Brezesinski, S. Siegel, J. Wu, J.B. Li, R. Miller, Colloids and Surfaces A 171 (2000) 175-184

[44] S. Pautot, B.J. Frisken, J.X. Cheng, X.S. Xie, D.A. Weitz, Langmuir 19 (2003) 10281-10287

Chapter 4

Interfacial aspects of water drop formation at micro-engineered orifices

Abstract

The formation of emulsions with micro-engineered silicon based arrays of micro-orifices is a relatively new technique. Until now, only the preparation of oil-in-water emulsion was studied due to the hydrophilic nature of silicon. This work evaluates the emulsification of water drops into n-hexadecane with hydrophobized arrays of micro-orifices. We have studied the drop formation rate, the number of active pores and the drop size. In contrast to conventional macroporous membranes used for membrane emulsification, we observed high dispersed phase fluxes up to 4600 L $h^{-1}m^{-2}bar^{-1}$ while all pores being active at applied pressures below 2 times the critical pressure. The drop diameter was independent from the applied pressure difference. We observed a pressure dependent lag time between drop formations at low emulsification pressures. The lag time is related to the rate of surfactant diffusion to the water-oil interface causing a reduction of the interfacial tension. A significant influence of the used hydrophobization agents, perfluorinated octyltrichlorosilane (FOTS) and octyltrichlorosilane (OTS), was found for the resulting drop sizes and the number of active pores.

4.1 Introduction

Emulsification techniques are widely used in food, pharmacy, and cosmetic industry to produce oil-in-water or water-in-oil emulsions. Commonly used techniques include rotor-stator systems, high-pressure homogenizers, and ultrasound [1]. Due to high shear forces, the dispersed phase is divided into small droplets, stabilized by surfactants. However, shear stress and thermo sensitive ingredients, such as proteins, may loose their bioactivity during this process [2]. Muschiolik et al. showed that whey proteins could change their physico-chemical properties due to a high pressure treatment [3]. The whey protein β-lactoglobulin for instance looses its emulsifying efficiency due to pressure-induced unfolding resulting in protein aggregation [4].

Cross-flow membrane emulsification is a relative new emulsification process. This technique requires less energy, generates less stress to the ingredients and produces narrow drop size distributions [5]. In this process, the dispersed phase is forced through a porous membrane into the flowing continuous phase (see Figure 1).

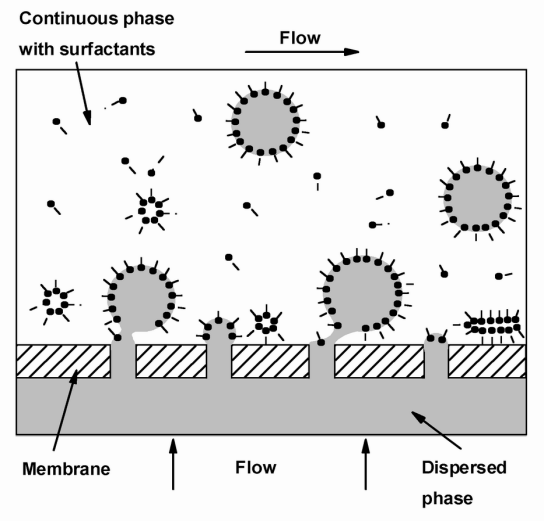

Figure 1: Schematic drawing of the emulsification process with porous membranes to produce water-in-oil emulsions.

Table 1: Membranes used for cross-flow membrane emulsification.

Membrane material	Type of emulsions	References
Al_2O_3	Oil-in-water	[6,7]
Shirasu Porous Glass (SPG)	Oil-in-water	[8-10]
Polycarbonate (PC)	Oil-in-water	[11]
Polypropylene (PP)	Water-in-oil	[12]

Lately, different types of membranes were employed for membrane emulsification having pore sizes in the micrometer range. As Table 1 indicates, most of them were exploited for the production of oil-in-water emulsions requiring hydrophilic membranes.

Until now, membrane emulsification technology has not found its way to large-scale manufacturing, because commercially available membranes possess some disadvantages. They require a high-pressure drop and consist of a highly porous and irregular morphology on a microscopic scale [13]. To overcome these disadvantages, a micro-engineered membrane was adopted from microfiltration [14,15]. This microsieve membrane, fabricated out of silicon nitride with a silicon support, has a precisely defined pore size and a narrow pore size distribution, combined with a micron-sized membrane thickness. Furthermore, the porosity can be optimized for emulsification to limit coalescence of neighboring drops as displayed in Figure 2.

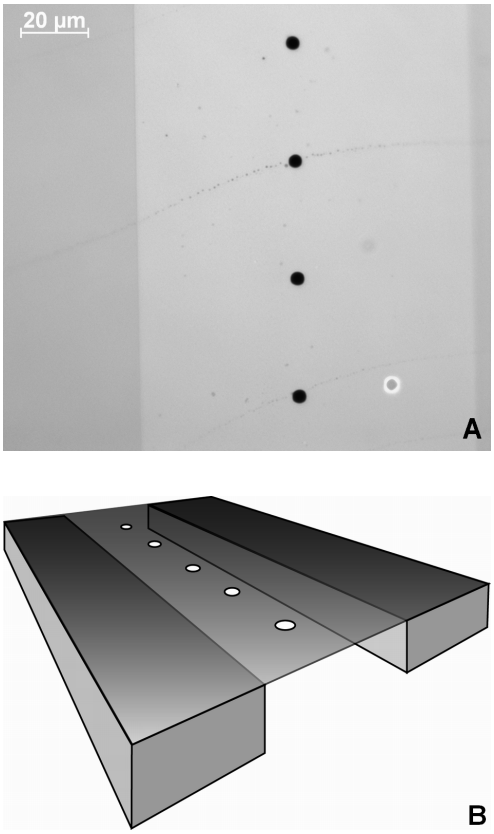

Figure 2: Optical image of a 3.5 µm micro-orifices (A) and a schematic representation of the micro-orifice array designed for membrane emulsification application (B). Further details can be found in section 2.

It is frequently stated, that membrane emulsification needs a surface that is not wetted by the dispersed phase. To our knowledge, only the work of Kobayashi et al. clearly shows for different emulsifiers that successful emulsification of oil into water only occurs if the oil phase does not wet the membrane surface [11]. In our recent paper we proved that a hydrophobic surface is required for producing water-in-oil emulsion [16]. Due to the silicon nitride processing conditions, groups like silanol (SiOH), primary ($SiNH_2$), and secondary amino groups (Si_2NH) are present [17]. Overall, this results in a relatively hydrophilic surface with water/air contact angles of 65°.

To perform successful emulsification of water into an oil phase, the surface properties of silicon nitride have to be changed into a hydrophobic state. A possible way to achieve surface hydrophobicity is the deposition of self-assembled monolayers of alkyltrichlorosilanes. These kinds of monomolecular coatings are hydrophobic and they show a good thermal and chemical stability [18].
In this paper we discuss interfacial aspects of water drop formation at silicon nitride micro-orifices to produce water-in-oil emulsions. Until now, only oil-in-water emulsification with silicon nitride arrays of micro-orifices was investigated. Within these studies, it was found that only a few percentages of the nozzles were active and that the drops were not formed continuously at the single nozzles [13]. A physical reason for this period of inactivity was not given. Here, we will show that the nozzle activity reaches 100 percent at relatively low pressures and that the discontinuity of the drop formation is related to the dynamic interfacial tension of the used water-oil-surfactant system.

4.2 Materials and Methods

Chemicals

N-hexadecane (Merck) was used as the continuous phase containing either 1 wt% BolecMT (Loders Croklaan B.V.) or 1 wt% Span85 (sorbitan-trioleate; Merck). BolecMT is a soybean based industrial emulsifier containing approximately 40wt% mono-, di-, and tri-glycerides, 36 wt% phospholipids, 18 wt% free fatty acids and 6 wt% proteins, polysaccharides and seed residues. For the dispersed phase MilliQ-water was used.
For the self-assembled monolayer formation two types of alkyltrichlorosilanes were used. Octyltrichlorosilane (OTS) (Aldrich, 97 %) and perfluoro-octyltrichlorosilane (FOTS) (Fluka, >97%) were used as received.

Micro-nozzle plates

Two types of silicon nitride micro-orifice arrays received from Aquamarijn Micro Filtration B.V. were used. The first one had pores with 2.5 μm in diameter arranged in three single row pore fields with distances of 100 μm between the pores.
The second used micro-orifice array (see Figure 2) had pores with a diameter of 3.5 μm arranged in one single row and two double row pore fields. The distance between the pores in all fields was 35 μm. The pores fields were separated by several hundreds of micrometer. The backsides of the pore fields for both arrays were fully open to guarantee a high accessibility for the dispersed phase without generating additional flow resistances.

Surface modification

As a pre-treatment, the micro-orifice arrays were cleaned and oxidized using a reactive oxygen plasma (Plasmafab 508, Electrotech; 10 min, 500 W, pO_2 = 16 mbar).
For the chemical vapor deposition of silane monolayers plasma oxidized silicon nitride micro-orifice arrays were stored together with a few microliters of FOTS or OTS in a dry sealed glass box. The heat treatment was carried out at 120°C for 2 hours in a nitrogen flushed oven. Afterwards the micro-orifice arrays were allowed to cool down to room temperature while staying in the oven followed by a stabilization step at 100°C for 1 hour. The modification process was finished by extensively rinsing first with iso-propanol, then with ultra pure water and dried with nitrogen. After these modifications surfaces of OTS and FOTS showed water contact angles of 104 ± 2° and 114 ± 1° respectively.

Interfacial tension and static contact angle

The dynamic interfacial tension measurements of BolecMT were conducted with a drop volume tensiometer (Lauda) at the University of Karlsruhe, Institut für Lebensmittelverfahrenstechnik (Germany). Static contact angles were measured with a goniometer (OCA 15, Data Physics).

Emulsification set-up

In order to visualize and quantify the drop formation process the micro-orifice arrays were placed into a module with a transparent cover slide designed for studying the filtration performance of silicon nitride microsieves shown in Figure 3B and 3C [19]. The continuous (oil) and the dispersed phase (water) were fed into the module via gear pumps with maximum flow rates of 100 L/h for the continuous phase and 1 L/h for the dispersed phase. Both phases were recirculated within the system. To prevent pore blocking the dispersed phase (water) was pre-filtered inline with a 0.45 μm cellulose acetate filter (Schleicher & Schuell).

The dispersed phase pressure was adjusted either with a needle valve or by changing the dispersed phase flow and monitored via a pressure sensor connected to a data acquisition system. The continuous phase pressure was measured next to the position of the micro-orifice array inside the module and collected as well by a data acquisition system. The data acquisition system was obtained from National Instruments equipped with two signal read-out cards and a serial interface connected to a personal computer. For the signal processing and for the calculation of the applied pressure difference ($\Delta p = p_{dispersed\ phase} - p_{continuous\ phase}$) a Labview program was used. The entire set-up is shown schematically in Figure 3A.

The visualization was performed using an inverted optical microscope (Zeiss Axiovert) equipped with a CCD camera providing a maximum frame rate of 8 frames per second. Although slow, this rate is sufficiently accurate to observe the drop formation process at low emulsification pressures and low cross-flow velocities.

The set-up was cleaned first with an aqueous detergent solution (Lux, Unilever, contains anionic and amphoteric surfactants) followed by a 1-2 vol.% aqueous Deconex solution (Borer Chemie; contains KOH). Both cleaning steps were performed at room temperature and low pressure. Afterwards the set-up was rinsed several times with ultra pure water. Before drying with air the ultra pure water was pressed out with air followed by flushing isopropanol through the system. After each experiment, the oil phase was pressed out with air before starting the mentioned cleaning procedure.

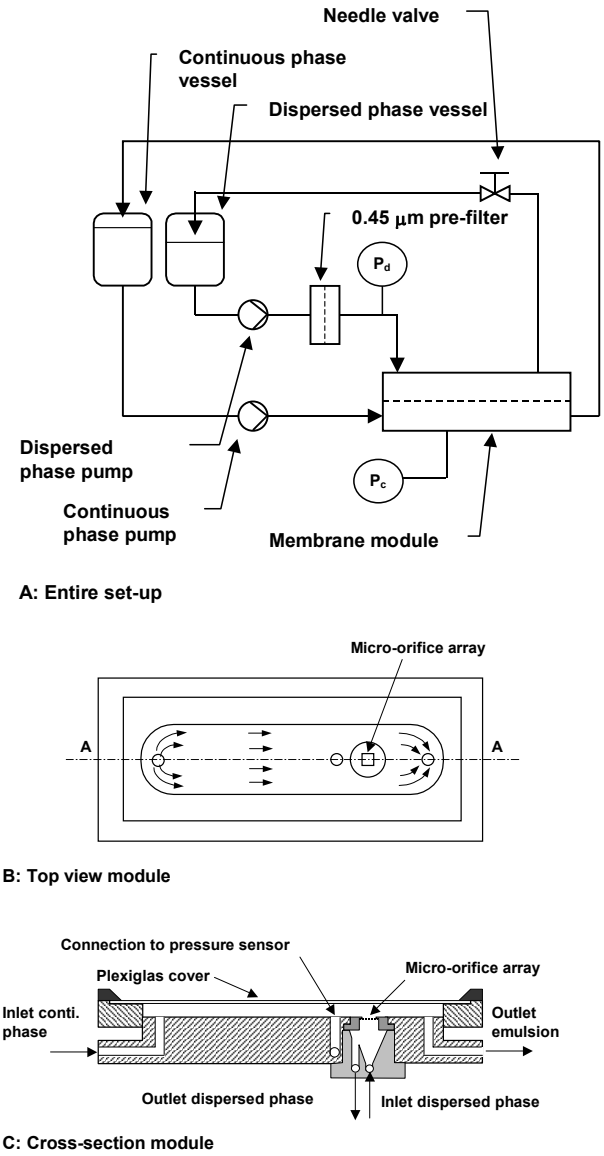

Figure 3: Cross-flow membrane emulsification set-up (A), top view (B) and cross-section (C) of the emulsification module.

Used micro-orifice arrays were cleaned separately from set-up and were replaced inside the set-up with a dummy array. The micro-orifice arrays were first washed with an aqueous detergent solution (Lux, Unilever, contains anionic and amphoteric

surfactants), then rinsed with tap water and followed by MilliQ-water, and finally with isopropanol. All rinsing and washing steps were performed at room temperature. Afterwards, the micro-orifices arrays were dried first in a nitrogen stream and then at 80°C.

The hydrophobized micro-orifice arrays were fixed and sealed within stainless steel holders with silicon glue. To start an experiment, the holder including a micro-orifice array was mounted into the emulsification module and connected to the dispersed phase supply tubing. Then both liquid phases were slowly pumped into the system at low pressure. At the same time the pressure data acquisition system was started. After the set-up was completely filled with both phases, the desired continuous phase velocity of 0.074 m/s was adjusted. Higher velocities were not explored due to the restrictions of the CCD camera. However, increasing the cross-flow velocity leads to smaller drop sizes as already reported in several studies [2,5,7,11]. The dispersed phase pressure was step-wise increased until first droplet formation occurred. From there on the dispersed phase pressure was adjusted. At each pressure step two movies of minimum 30 seconds were recorded.

Individual frames were extracted from the movies with a video converter program and the drop size, the drop formation rate and the number of active pores were achieved from single frames with the imaging software Scion Image® (Scion Corporation).

4.3 Results and discussion

Drop formation rate

The drop formation process starts when the pressure difference exceeds the critical pressure ($P_{critical}$), which is determined by the pore radius (R_{pore}) and the interfacial tension (γ) according to equation 1.

$$P_{critical} = \frac{2\gamma}{R_{pore}} \qquad (1)$$

For the 2.5 μm array and 1 wt% BolecMT the experimentally obtained critical pressure is equal to 183 mbar and for the 3.5 μm array and 1 wt% Span 85 the value is 54 mbar as it can be seen in Figure 4, which shows the drop formation rate versus the applied pressure difference.

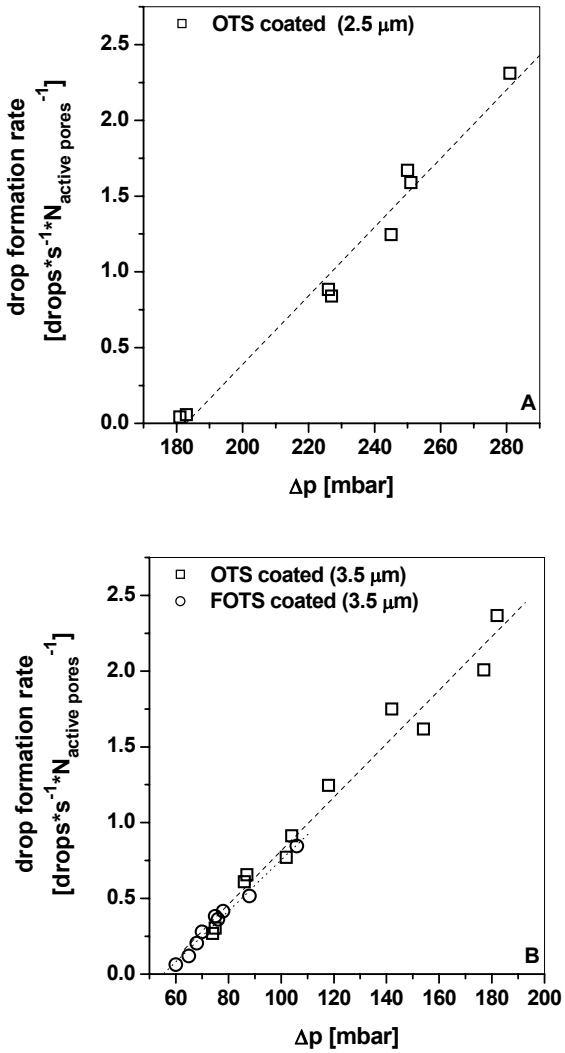

Figure 4: Drop formation rate versus applied pressure difference (Δp) of water drops emulsified into 1 wt% BolecMT (A) containing n-hexadecane with a 2.5 μm micro-orifices array and into 1 wt% Span85 (B) containing n-hexadecane with a 3.5 μm micro-orifices array.

The drop formation rate also accounts for the increasing number of active pores with increasing pressure. When doing this, we found a linear relationship with the intercept at the x-axis giving the critical pressure of the used surfactant containing system. These pressures correspond to interfacial tensions of 11.4 for BolecMT and 4.7 mN/m for Span85, respectively. The slope of the regression lines in Figure 4A and 4B corresponds to the resistance of the pores following Darcy's law.

The dispersed phase flux in our experiments was remarkable high compared to conventional macroporous membranes and comparable to the flux obtained for oil-in-water emulsification with silicon nitride micro-orifice arrays as indicated in Table 2. The flux value was calculated from the average drop volume ($\overline{V}_{Drop}$), the drop formation rate and the number of active pores ($N_{p,\,active}$) according to equation 2.

$$Flux = \frac{\overline{V}_{Drop} \cdot Drop\ formation\ rate \cdot N_{p,active}}{\Delta p \cdot A_{Array}} \qquad (2)$$

The considered array area (A_{Array}) was 1.599 10^{-7} m^2 and represents only the observed unsupported area of the micro-orifices array.

The most distinguishing feature between conventional membranes and the silicon based micro-orifices arrays is their thickness and morphology. The conventional membranes have a thickness ranging from 50 to several hundreds of micrometer. The morphology is tortuous and pore sizes are polydisperse. Thickness and tortuosity will lead to a high membrane resistance.

The pure water flux for polypropylene hollow fibers was measured to be 6000 times higher than the water flux in a membrane emulsification experiment [12]. Contrary to the high porosity of the conventional membranes, which enables a high pure liquid permeability, Vladisavljevic et al. calculated that for SPG membranes only 2 percentages of the pores were active within emulsifying oil into water [10]. The interfacial tension between oil and water influences the permeability of the dispersed phase in highly porous and tortuous membranes to a great extend.

Table 2: Dispersed phase flux obtained here in comparison with different membranes found in literature.

Type of membrane	Mean pore size [μm]	Δp [bar]	Dispersed phase	Flux [L $h^{-1}m^{-2}bar^{-1}$]	Ref.
Si_xN_y micro-orifices[1]	3.5	0.177	water	4600	present work
Si_xN_y micro-orifices	7	0.09	n-hexadecane	21000	[13]
Silicon MC	17.3	0.108	soybean oil	600	[23]
SPG membrane	2.5	0.264	rape seed oil	11	[10]
Ceramic membrane	0.2	1.4	mineral oil	14	[20]
PP hollow fiber	0.4	0.76	water	0.26	[12]
MPG membrane	0.5	3.5	sunflower oil	13	[21]

[1] hydrophobized with OTS

The silicon based micro-orifices arrays are extremely thin and have an optimized morphology. The porosity is quite low to prevent coalescences of growing drops. Here, in contrast to Vladisavljevic et al. the percentage of active pores was extremely high. The percentage of active pores was over 90 percent in case of the 2.5 μm array in combination with BolecMT, reached at 1.25 times the critical pressure. For the 3.5 μm micro-orifices array coated with OTS the percentage of active pores was about 60 percent at 3.3 times the critical pressure. For the same arrays coated with FOTS the pore activity reached 100 percent at 1.6 times the critical pressure. For comparison, these values are listed in Table 3.

Table 3: Number of active pores and membrane properties.

	D_{pore} [μm]	Thickness [μm]	Porosity [%]	No. of active Pores [%]	At x times $P_{critical}$	Ref.
SPG - membrane	15	1000	53	0.5	6	[22]
Silicon Microchannel	17.3	200	1.2	95	6	[23]
Si_xN_y Microsieve	7	1	0.12	16	3	[13]
Micro-orifice array[1]	3.5	1	0.25	100	1.6	present work
Micro-orifice array[2]	2.5	1	0.05	100	1.3	present work

[1] hydrophobized with FOTS

[2] hydrophobized with OTS

Only a few papers have reported the number of active pores obtained by visualization of the drop formation process. The optical observation of the oil drop formation into a 0.3 wt% SDS aqueous solution using a 10 μm hydrophilic polycarbonate track-etch membrane showed only 1 percent active pores just above the critical pressure of 13.5 mbar. Unfortunately, no data is given for higher pressures [11]. A SPG membrane with a mean pore size of 15 μm used to emulsify soybean oil into 0.3 wt% SDS aqueous solution showed an increase of the number of active pores from 0.3 to 0.5 percent while the dispersed phase flux was increased by a factor of six [22]. For rectangular straight-through microchannels with a hydraulic diameter of 17.3 μm, the number of active microchannels increased from 10 to 95 percent with the increasing pressure from 1.8 mbar (critical pressure) to 18 mbar. As dispersed phase soybean oil was used and emulsified into 0.3 wt% SDS aqueous solution [23]. Abrahamse et al. reported at 3 times the critical pressure for a 7 μm silicon nitride micro-orifice array that 16 percent of the pores were active during the emulsification of hexadecane into 1 wt% Tween20 aqueous solution. The

reason for the low pore activity was explained by the small ratio of the pore resistance (R_p) over the substructure resistance (R_s) against flow. The ratio found for the 7 μm silicon nitride array was 3.7. The authors claim that a higher ratio leads to a higher number of active pores [24]. Here, micro-orifice arrays were used with an open substructure, which results in a lower flow resistance in the substructure, and with smaller pore sizes resulting in higher flow resistances in the pores. This increases the ratio of R_p over R_s compared to Gijsbertsen-Abrahamse et al. by a factor of 14 and explains the differences between the high percentage of active pores reported in our work and low activity reported by Abrahamse et al. [13]. Table 3 suggests also that the surface porosity influences the number of active pores.

Drop size

The formed water drops had diameters in the range of 100 to 200 μm as shown Figure 5. They were one order of magnitude larger than the nozzle diameter of the used arrays. In order to observe the drop formation process we performed the emulsification at low cross-flow velocities resulting in relative large drops. The coefficient of variation, which is the standard deviation divided by the average drop size, varied between 5 and 25 percent and increased with increasing number of active pores. At high pore activity growing and detaching drops were interfering with drops growing next to it. This results in a less controlled drop detachment of neighboring drops and larger drop size variations. The drops produced with FOTS coated arrays were for both pore sizes and both surfactants larger compared to those produced via OTS coated arrays. This is related to the approximately 20° lower contact angle of water in surfactant containing hexadecane on FOTS coated substrates [16].

The drop diameter was independent of the applied pressure for both observed emulsifier systems and for both hydrophobic coatings as depicted in Figure 5. Van der Graaf et al. reported that the drop size increases at constant emulsifier concentration if the applied pressure difference increases [25]. These observations can be related to the adsorption rate of the emulsifier on a growing droplet. Schröder et al. suggested that the influence of the dispersed phase pressure becomes less as the emulsifier adsorbs faster [2]. When the fast emulsifier SDS is used, the drop

diameter is nearly independent from the applied dispersed phase pressure [2,22]. Here, slow adsorbing surfactants showed the same results as fast adsorbing emulsifiers.

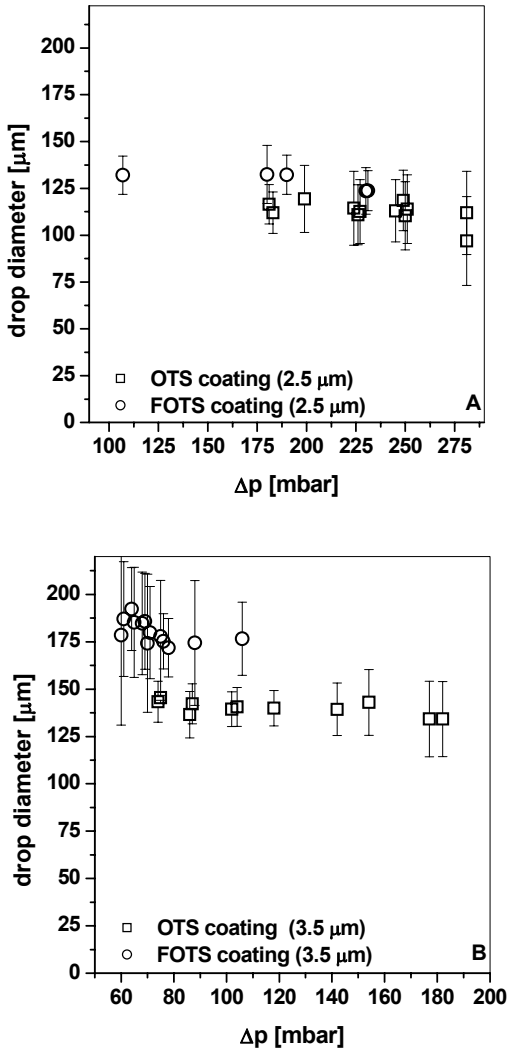

Figure 5: Average drop diameter versus applied pressure difference (Δp) of water drops emulsified (A) into 1 wt% BolecMT containing n-hexadecane with 2.5 μm OTS and FOTS coated arrays and (B) into 1wt% Span85 containing n-hexadecane with 3.5 μm OTS and FOTS coated arrays.

The interfacial tension is a major factor determining the final drop size. It forces the drop to remain attached to the pore as long as the interfacial tension force is higher than the shear force applied by the cross-flowing continuous phase (Figure 6).

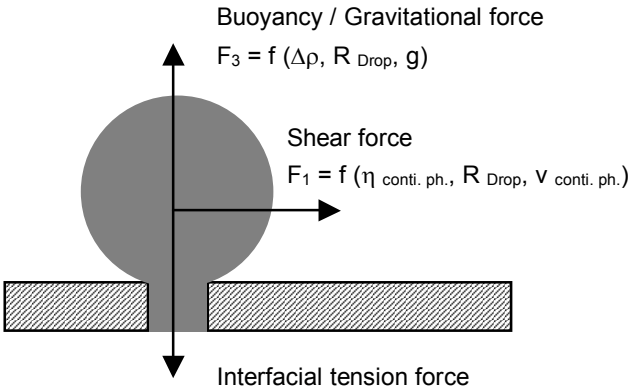

Force balance:

$$6\,\pi\,v_{conti.\ ph.}\,\eta_{conti.\ ph.} + 4/3\,\pi\,R^3_{Drop}\,\Delta\rho\,g = 2\,\pi\,\gamma\,R_{Pore}$$

Figure 6: Schematic drawing of the major forces acting on a droplet inflated from a pore into the cross-flowing continuous phase.

When the pressure is increased, the drop grows faster while the adsorption kinetic of the emulsifiers is not changed. The higher interfacial tension force keeps the drop attached to the pore. At constant cross-flow velocity the shear force scales with the drop diameter. Hence, the drop grows until a diameter is reached at which the shear force is higher than the interfacial tension force. For fast adsorbing emulsifiers the interfacial tension will be close to its equilibrium value. In our case, however, BolecMT is used, which is a very slow adsorbing emulsifier [16]. This suggests that another regime exist where the drop diameter is independent from the applied pressure. In the first regime the adsorption of the emulsifier is fast enough to compensate the surfactant dilution of the interface caused by the expansion of the growing drop. Therefore, the final interfacial tension is not significantly changing over a certain pressure range. While in the other regime, after the initial adsorption

to start drop growth, the surfactant adsorption rate is far lower then the surfactant surface dilution rate. Therefore, the interfacial tension increases due to surfactant dilution at the interface caused by its growth and insufficient replenishment out of the continuous phase.

Lag time

During the visual observation of the drop formation it was found that the drops were not formed continuously at low pressure differences. After detachment of a drop the pore remained inactive for a certain period of time before a new drop was inflated as depicted in Figure 7. The period of inactivity is called lag time and was firstly reported by Abrahamse et al. [13]. Van der Graaf et al. did not observe any lag time [25]. Today, no physical reason for the lag time nor the conditions at which a lag time occurs are reported. Here, we will prove that the lag time is a subtle measure for the dynamic interfacial tension of the oil-water-surfactant system.

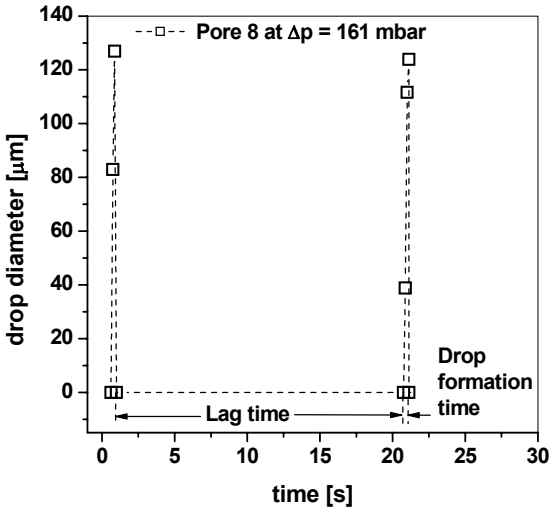

Figure 7: Growth of water drops from a single pore at 161 mbar. (2.5 μm OTS coated array; 1 wt% BolecMT dissolved in n-hexadecane).

A lag time was found for all observed pores during all performed experiments. The most obvious finding concerning the lag time was the decrease of the lag time with

increasing pressure difference. Figure 8 shows the pressure difference plotted as a function of the inverse square root of the lag time. For 1 wt% Span85 we observe a clear linear relationship (Fig. 8B). For 1wt% BolecMT (Fig. 8A) the linear relation holds only for pressure differences above 180 mbar. We will explain this observation later in this section. Based on the data reported by Abrahamse et al. we calculated the lag time for the hexadecance-water-Tween20 system used in this study [13]. The applied pressure difference showed as well a linear function of the inverse square root of the lag time.

The relation between the lag time and the pressure difference can be explained with the critical Laplace pressure. This pressure has to be overcome by the applied pressure difference to inflate a drop from a nozzle and corresponds to the Laplace pressure of a hemispherical interface at the nozzle opening. The second variable to take into account is the interfacial tension (IFT). For a certain Δp and a given nozzle diameter the IFT has to reach a value which corresponds to the critical Laplace pressure. As long as the applied pressure difference is lower compared to the Laplace pressure drop formation will not occur.

After drop detachment, a sufficient amount of surfactants has to adsorb at the hemispherical interface before the critical Laplace pressure is reached again. The adsorption of surfactants at an interface is a kinetic process and is represented by the dynamic interfacial tension of a given surfactant.

Figure 9 shows a representation of the relation between the lag time and the pressure difference. If the emulsification process operates at low pressure difference (Δp_2 in Figure 9) then the Laplace pressure has to decrease by the surfactant adsorption to a relatively low value (from point 1 to point 3). The absolute value of the lag time depends on the corresponding interfacial tension at the moment of drop detachment (point 1). For faster adsorbing surfactants, indicated by a higher diffusion coefficient, the lag time reduces, because the required critical interfacial tension is reached at earlier (lag) times. Following the same arguments explains that increasing the pressure difference leads to a decreasing lag time.

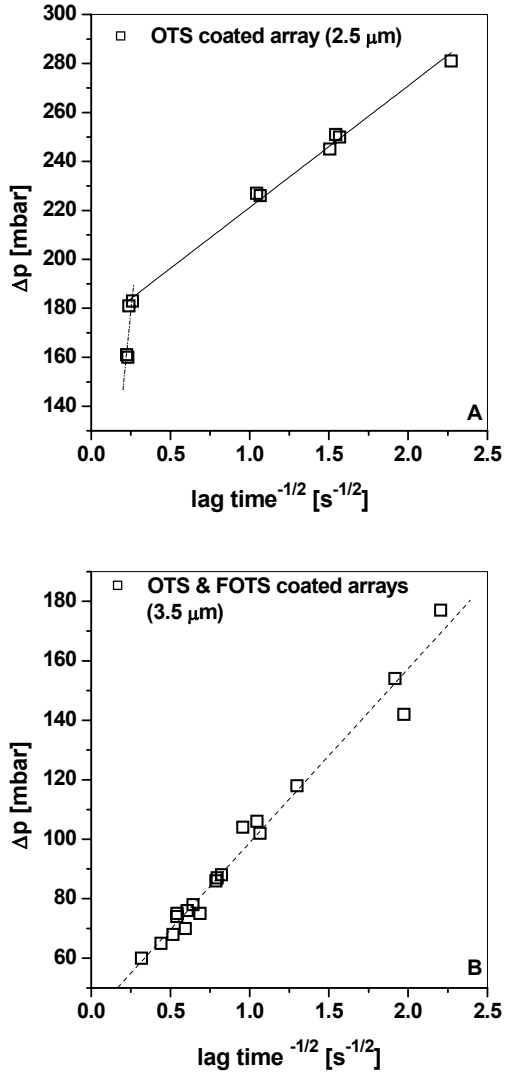

Figure 8: Applied pressure difference versus the inverse square root of lag time for (A) 1 wt% BolecMT and (B) 1 wt% Span 85.

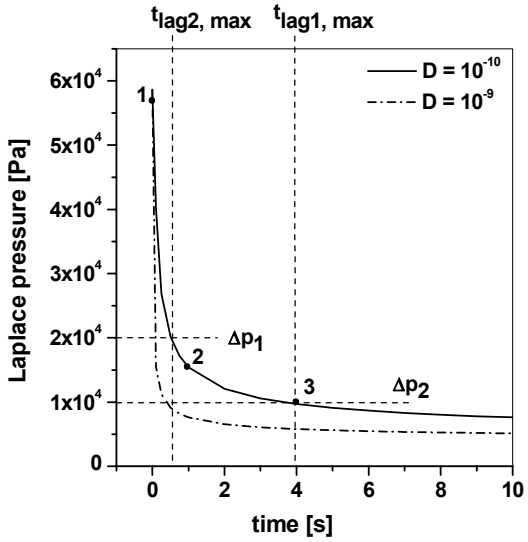

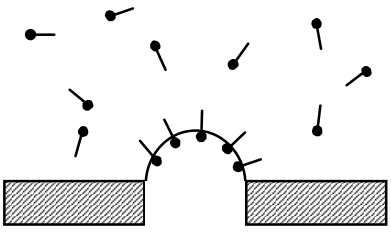

Point 1:

- Low surfactant surface coverage
- High $P_{Laplace}$
- $P_{Laplace} >> \Delta p_2$
- Hemisphere at nozzle tip

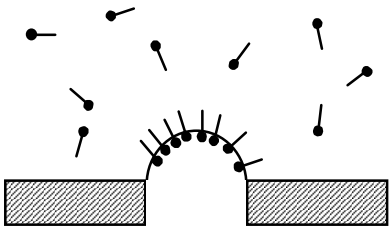

Point 2:

- Increasing surface coverage
- Decreasing $P_{Laplace}$
- $P_{Laplace} > \Delta p_2$
- Hemisphere at nozzle tip

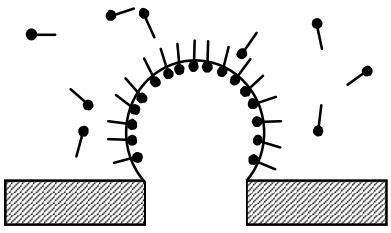

Point 3:

- Increasing surface coverage
- Decreasing $P_{Laplace}$
- $P_{Laplace} \leq \Delta p_2$
- Inflation of a drop

Figure 9: Decline of the Laplace pressure with adsorption time. Calculated via equation 1 and 3 for a nozzle size of 3.5 μm and two different diffusion coefficients.

We can conclude that the lag time appears to be a sensitive measure of the dynamic interfacial tension. To prove this, the corresponding interfacial tensions were calculated from the lag time according to the Laplace pressure equation and in case of 1 wt% BolecMT compared with the dynamic interfacial tension obtained by the drop volume method. The results are plotted in Figure 10. The interfacial tension derived from the lag time fits well to the values from the drop volume method.

Recalling the inverse square root relation between the lag time and Δp, Figure 11 depicts the same for the IFT of 1 wt% Span85. This type of plot is typical for presenting the dynamic interfacial tension of a given emulsifier containing system. Basis for these plots is the so-called long time approximation for the dynamic interfacial tension [26].

$$\gamma(t) - \gamma_{eq.} = \frac{RT\,\Gamma_c^2}{C_0}\sqrt{\frac{\pi}{4D\,t}} \qquad (3)$$

Equation 3 is a simplified version of the equation of Ward and Tordai relating the interfacial tension decline with the surfactant bulk concentration C_0, the adsorbed emulsifier density Γ_c and the diffusion coefficient D. From the intercept of the linear regression line in Figure 11 the equilibrium interfacial tension of 3.5 ± 0.2 mN/m is obtained. This value agrees with the equilibrium interfacial of 3.3 ± 0.1 mN/m for 1 wt% Span 85 obtained from sessile drop measurements.

The interfacial tension of 1 wt% BolecMT does not follow the linearity of equation 3 over the entire time range. Only at short adsorption times the values agree with it. This emulsifier is a mixture of phospholipids and proteins and its adsorption on interfaces is a competitive process. Therefore, its interfacial tension decline differs from single component adsorption as we showed in an earlier work [16].

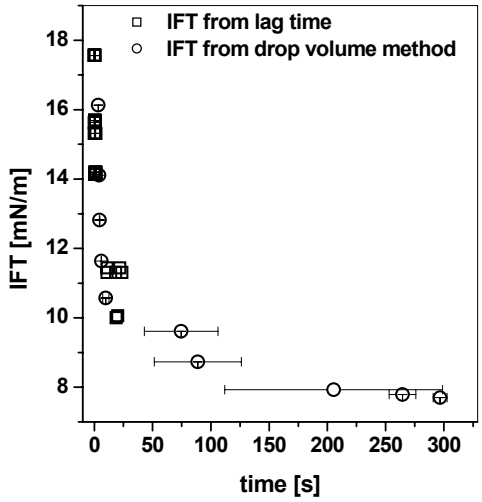

Figure 10: Comparison between interfacial tension (IFT) of water/n-hexadecane + 1 wt% BolecMT obtained from lag time and from drop-volume method.

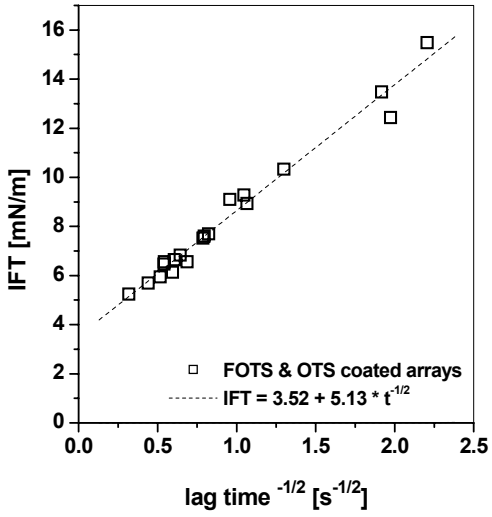

Figure 11: Interfacial tension (IFT) versus the negative square root of the lag time according to equation 3 of 1 wt% Span 85.

As indicated by equation 3 the slope and the intercept of the regression line in Figure 11 can be influenced by varying the surfactant concentration and by using surfactants with different diffusion coefficients. Considering the first, concentrations

below the critical micelle concentration (CMC) will result in a steeper slope and a higher intercept and for concentrations above the CMC the line flattens while fixed at a constant intercept representing the interfacial tension of the fully saturated interface. Secondly, for emulsifiers with higher diffusion coefficients the slope will increase. In conclusion, the lag time will be shorter or disappears at a given pressure difference for higher surfactant concentrations and for surfactants with higher diffusion coefficients.
In general, a lag time appears in an emulsification process at pressures close to the critical pressure and in combination with slow or medium fast adsorbing emulsifiers. It disappears if the applied pressure is increased or faster adsorbing emulsifiers are used.

4.4 Conclusions

We could demonstrate successful emulsification of water into n-hexadecane with hydrophobic arrays of micro-orifices. Significant differences between FOTS and OTS coatings were found for the drop diameter caused by different contact angles with in the system of water/n-hexadecane+surfactant/coated substrate. The different hydrophobic coatings do not significantly influence the drop formation rate, the percentage of active pores and the lag time. The extremely low porosity and the open back structure of the used micro-orifice arrays result in nearly 100 percent active pores at less than two times the critical pressure.
The observed lag time also disappears at a certain Δp. For fast adsorbing emulsifiers like SDS a lag time is not observed. Therefore, two ways are possible to avoid the lag time. Using faster adsorbing emulsifiers or if this is not possible, due to restrictions of the usable emulsifiers within the product recipe, the applied pressure difference over the nozzles can be increased until the lag time vanishes.

4.5 Acknowledgements

The work was sponsored by the European Union (Thames Project; QLRT 2000-01228). Microsieve membranes were kindly provided by Aquamarijn B.V. The drop volume dynamic interfacial tension measurements were conducted by Uwe Lambrich from the University of Karlsruhe – Germany.

4.6 Abbreviations

CMC	Critical micelle concentration
FOTS	perfluorinated octyltrichlorosilane
IFT	Interfacial tension
MPG	Micro porous glass
SDS	Sodium dodecylsulfate
SPG	Shirasu porous glass
PC	Polycarbonate
PP	Polypropylene

4.7 References

[1] S. Sjöblom, (Ed.); Encyclopedic Handbook of Emulsion Technology; Marcel Dekker, New York, 2001

[2] V. Schröder, H. Schubert, Colloids and Surfaces A 152 (1999) 103-109

[3] G. Muschiolik, S. Dräger, I. Scherze, H.M. Rawel, M. Stang, in Food Colloids; E. Dickinson, B. Bergeståhl, Eds.; The Royal Society of Chemistry: Cambrigde, 1997; No. 192, 393-400

[4] V.B. Galazka, E. Dickinson, D.A. Ledward, Food Hydrocolloids 10 (2) (1996) 213-219

[5] S.M. Joscelyne, G. Trägårdh, J. Membr. Sci. 169 (2000) 107-117

[6] V. Schröder, O. Behrend, H. Schubert, J. Colloid Interface Sci. 202 (1998) 334-340

[7] S.M. Joscelyne, G. Trägårdh, J. of Food Engineering 39 (1999) 59-64

[8] K. Kandori, in Food Processing: Recent Developments (Ed.: A. G. Ganokar), Elsevier Science 1995, Chapter 7, 113-142

[9] N.C. Christov, D.N. Ganchev, N.D. Vassileva, N.D. Denkov, K.D. Danov, P.A. Kralchevsky, Colloids and Surfaces A 209 (2002) 83-104

[10] G.T. Vladisavljevic, H. Schubert, Desalination 144 (2002) 167-172

[11] I. Kobayashi, M. Yasuno, S. Iwamoto, A. Shono, K. Satoh, M. Nakajima, Colloids and Surfaces A 207 (2002) 185-196

[12] G.T. Vladisavljevic, S. Tesch, H. Schubert, Chemical Engineering Processing 41 (2002) 231-238

[13] A.J. Abrahamse, R. van Lierop, R.G.M. van der Sman, A. van der Padt, R.M. Boom, J. Membr. Sci. 204 (2002) 125-137

[14] C.J.M. van Rijn, M.C. Elwenspoek, IEEE proc. MEMS 1995, 83

[15] Nano and Micro Engineered Membrane Technology, Chapter 11: Membrane Emulsification, C.J.M. van Rijn, Elsevier Amsterdam, 2004 ISBN 0.444-51489-9

[16] M.J. Geerken, R.G.H. Lammertink, M. Wessling, Colloids and Surfaces A (2006) doi:10.1016/j.colsurfa.2006.06.30

[17] B.V. Zhmud, J. Sonnefeld, L. Bergström, Colloids and Surfaces A 158 (1999) 327-341

[18] M.J. Geerken, T.S. van Zanten, R.G.H Lammertink, Z. Borneman, W. Nijdam, C.J.M. van Rijn, M. Wessling, Advanced Eng. Materials 6 No.9 (2004) 749-754

[19] M. Gironès, Z. Borneman, R.G.H. Lammertink, M. Wessling, J. Membr. Sci. 259 (2005) 55-64

[20] R.A. Williams, S.J. Peng, D.A. Wheeler, N.C. Morley, D. Taylor, M. Walley, D.W. Houldsworth, Trans IChem. E. 76 Part A (1998) 902-910

[21] I. Scherze, K. Marzilger, G. Muschiolik, Colloids and Surfaces B 12 (1999) 213-221

[22] M. Yasuno, M. Nakajima, S. Iwamoto, T. Maruyama, S. Sugiura, I. Kobayashi, A. Shono, K. Satoh, J. Membr. Sci. 210 (2002) 29-37

[23] I. Kobayashi, M. Nakajima, K. Chun, Y. Kikuchi, H. Fujita, AIChE Journal 48 (2002) 1639-1644

[24] A.J. Gijsbertsen-Abrahamse, A. van der Padt, R.M. Boom, J. Membr. Sci. 217 (2003) 141-150

[25] S. van der Graaf, C.G.P.H Schroën, R.G.M. van der Sman, R.M. Boom, J. Colloid Interface Sci. 277 (2004) 456-463

[26] B.B. Niraula, T.K. Chun, H. Othman, M. Misran, Colloids and Surfaces A 248 (2004) 157-166

Chapter 5

Micro-fabricated metal nozzle plates: An alternative for silicon based emulsification devices

Abstract

In this chapter the fabrication and use of micro-structured metal nozzle plates as emulsification devices is investigated and discussed. These structured metal nozzle plates were fabricated via two distinct routes. Laser ablation was used to drill micrometer-sized holes into stainless steel and aluminum foils. A conventional steel mesh with an average pore size of 2.4 μm fabricated by weaving and roll compaction of micrometer sized steel wires was investigated. The laser ablation was performed with a femtosecond laser. Average hole diameters of 4.4 μm with a standard deviation of 0.36 μm were obtained. The perforated metal nozzle plates were used for oil-in-water and after hydrophobization with alkylchlorosilanes for water-in-oil emulsification as well. In both case, two types of drop formation processes were observed. The first one is the shear-induced drop formation well known for cross-flow membrane emulsification. The second is the spontaneous drop formation known from microchannel emulsification.

5.1 Introduction

In the last years, several micro-engineered emulsification devices were developed to produce emulsions with drop size distributions having coefficient of variations (COV) below 10 percent. In comparison the lower limited reachable with membrane emulsification using conventional membranes such as micro-porous glass, ceramic and polymeric membranes is often above 10 percent. Micro-engineering tools like photolithography and etching, adapted from the semiconductor industry, were used to fabricate precisely defined structured drop formation devices. Therefore, the disadvantage of conventional membranes having a polydispersed pore size distribution and a tortuous morphology and its influence on the resulting emulsion can be avoided.

The microchannel emulsification technique developed by T. Kawakatsu and co-workers was one of the first applications using micro-engineered devices to produce narrow drop size distributed emulsions [1]. Rectangular microchannels were etched into a silicon wall, which separates the dispersed phase from the continuous phase. Towards the continuous phase the microchannel ends in a terrace, where dispersed phase drops are inflated before they detach as depicted schematically in Figure 1. The whole microchannel plate is covered with a transparent cover to allow an optical observation of the drop formation process.

The hydraulic diameter of the microchannels fabricated in silicon varied between 4.2 and 9.6 μm and the aspect ratio from 1.2 to 3.6. The terrace length was mostly about 30 μm. In most of the studies oil-in-water emulsification was performed due to the more hydrophilic nature of silicon. Within these studies, oil drops of 2.6 to 4.6 times the hydraulic diameter of microchannels were produced with coefficients of variation from 1.4 to 13 percent [2-5]. The drop formation process is characterized by the spontaneous transformation of the disk-like drop between the terrace and the cover plate to a spherical drop when the edge of the terrace is reached. This transformation is driven by the Laplace pressure difference between the disk-shaped drop and the spherical shape. The latter one has a lower Laplace pressure. Therefore, the dispersed phase on the terrace flows faster into the spherical drop than the dispersed phase is supplied through the microchannel. Due to this, necking

occurs between the dispersed phase on the terrace and the growing spherical drop at the edge of the terrace until the neck ruptures and the spherical drop releases from the edge.

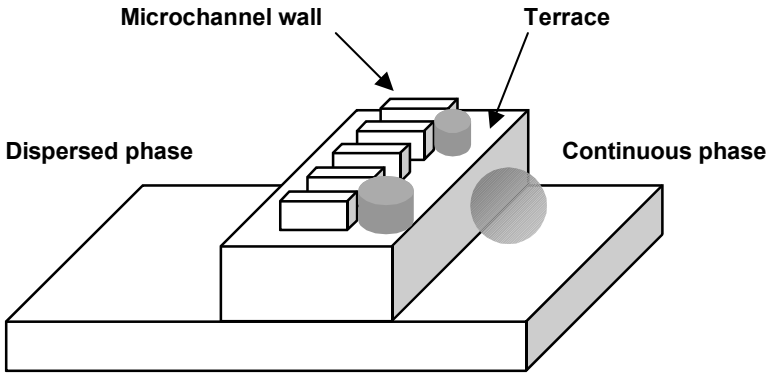

Figure 1: Schematic drawing of a microchannel emulsification device, as used by Nakaijma [1].

Kobayashi and co-workers developed a second design exploiting the spontaneous drop formation process. Here, rectangular microchannels were etched vertically through a silicon plate with a thickness of 100 to 200 μm (see Figure 2) and therefore called straight-through microchannels. The slit-shaped channels had hydraulic diameters from 10.6 to 22.1 μm. The aspect ratio varied from 3.4 to 5.1. The formed oil drops were 1.9 to 3.5 times larger than the hydraulic diameters of the used microchannels and the coefficients of variation were ranging between 1.4 and 10 percent [6-9].

Recently, Kobayashi and co-workers designed a new straight-through microchannel emulsification device fabricated out of silicon via photolithography and deep-reactive-ion etching. This design, quite similar to the microchannel/terrace approach, consists out of a circular dispersed phase supply channels ending in high aspect ratio slits towards the continuous phase. The slits themselves had an aspect ratio of 9.5, a hydraulic diameter of 19.9 μm and a depth of 21 μm. With this design Kobayashi et al. performed successful emulsification of a low viscosity dispersed

phase (decane) into 1 wt% aqueous SDS solution. The decane drops had an average diameter of 40.9 μm and a COV of 1.3 percent [10].

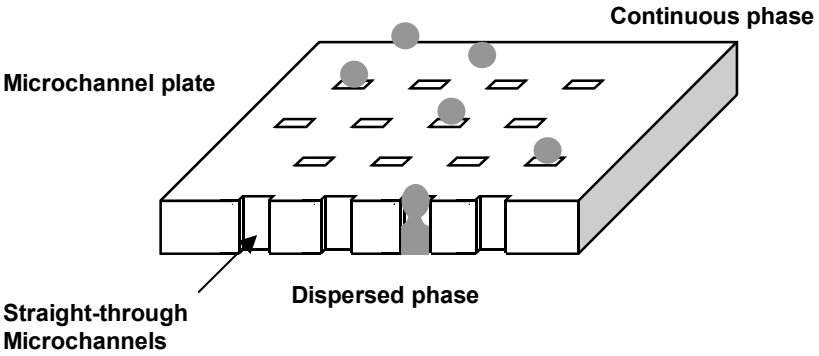

Figure 2: Schematic picture of a straight-through microchannel plate.

Analog to conventional membranes van Rijn and co-workers generated a micro-engineered membrane (microsieves) based on silicon and silicon nitride [11]. In principle, it is similar to the straight-through microchannel plate, but in contrast to the MC plate the membrane layer is only about 2 μm in thickness. The membrane layer is supported by a silicon grid structure as depicted in Figure 3. The accuracy of the fabricated pores is very high. The standard deviation of the pore diameter is less than 1 percent for pores larger than 10 μm and approaches 5 percent for pores of 1 μm [12].

Oil-in-water emulsifications were studied using low porosity microsieves with 7 and 4.8 μm circular pores [13,14]. Resulting drop sizes were ranging between 40 and 220 μm depending on the process conditions. Here, drops are released from the pores by shear force generated by the cross-flowing continuous phase. Therefore, the drop size strongly dependents on the cross-flow velocity of the continuous phase.

Hydrophobic silicon nitride micro-nozzle plates with pores sizes of 2.5 and 3.5 μm were used to produce water-in-oil emulsions. The produced water drops had sizes between 100 and 200 μm and COV values were ranging from 5 to 25 percent [15].

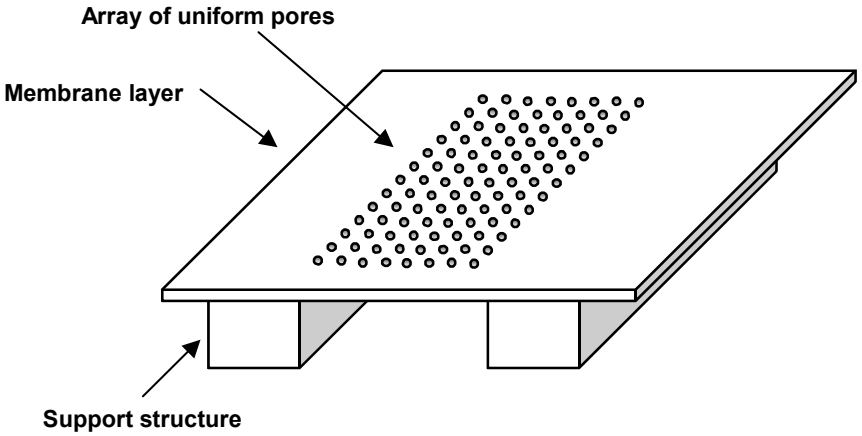

Figure 3: Schematic representation of silicon nitride microsieve.

Main drawbacks of these methods are the high fabrication costs for the emulsification devices and the restriction to silicon based materials.
Within this paper, we discuss the use of regular micro-structured metal nozzle plates fabricated without the use of cleanroom technology (photolithography and etching processes) for water-in-oil and oil-in-water emulsification. In order to produce water-in-oil emulsions the metal surfaces were hydrophobized with self-assembled monolayers of alkylsilanes. The results achieved with laser-drilled metal foils and with a conventional woven metal mesh are presented and compared with silicon based emulsification devices fabricated with cleanroom technologies.

5.2 Direct micro structuring of metal substrates

The direct structuring of metal substrates without the use of any cleanroom technology (including photolithographic and LIGA methods) offers the ability to decrease the fabrication costs. Compared to silicon, ceramics and polymers, metal alloys like steel offer good mechanical and chemical properties. Here, we will give a short overview of direct fabrication techniques for microchannels and micro holes with dimensions below 50 μm in metals.

Micro-mechanical machining is one technique to create microstructures in metals with feature sizes ranging from tens of micrometer to a few millimeters. The feature size is mainly determined by the size of the used micro machining tool, which is mainly made from tungsten carbide. Commercial end mills with diameters down to 50 μm are available. In literature ends mills with diameters of 11 and 25 μm are reported. The latter one was used to fabricate microchannels with 25 μm in width and depth [16].

Electro-chemical micro drilling (ECD) is another technique for machining metals. Within this method the material of the work piece is removed by an anodic dissolution process. An electrical field is applied between the cathode tool and the anodic work piece. The gap between the cathode and the anode is filled with an acidic electrolyte. The ECD process enables to drill holes with very smooth surfaces, without creating a burr and avoiding wear and residual stress [17]. This technique allows the fabrication of three-dimensional and high aspect ratio structures in stainless steel with minimum feature sizes of 10 μm [18]. A recent study shows the fabrication of through holes in steel foils [19]. Main drawback of this method is the long processing time of several tens of minutes for each hole. Simultaneous drilling with several tools is possible.

Laser ablation is a promising tool to fabricate microstructured devices out of polymers, metals and ceramics [20-24]. Here, a brief overview is given about the drilling of straight-through holes in metals. In general, two different types of laser drilling are discussed in literature. The first one is trepanning. Within this technique through holes in 1 mm thick stainless steel and aluminum samples down to 50 μm are reported [25]. Secondly, percussion drilling generates through holes with a certain degree of taper. Therefore, one has to distinguish between the hole diameter on the entrance side of the laser beam and on the exit side, which is the smaller one. In literature percussion drilled exit holes in stainless steel foil down to 3 μm were found [26].

5.3 Materials and Methods

Materials

For water-in-oil emulsification, n-hexadecane (Merck) was used as the continuous phase containing 1 wt% Span85 (sorbitan-trioleate, Merck). For the dispersed phase MilliQ-water was used. For oil-in-water emulsification sunflower oil was used as the dispersed phase and water containing 1 wt% Tween20 (polyoxyethylene (20) sorbitan monolaurate, Merck) as the continuous phase.

For the self-assembled monolayer formation two types of alkyltrichlorosilanes were used. Octyltrichlorosilane (OTS) (Aldrich, 97 %) and a perfluorinated octyltrichlorosilane (FOTS) (Fluka, >97%) were used as received.

For laser percussion drilling 25 μm thin aluminum and 50 μm thin stainless steel foils were used as metals substrates. Besides laser-drilled metal samples, a woven stainless steel mesh (1 μm nominal pore size, Haver & Boecker, Germany) was investigated. This mesh was roll compacted after the weaving process resulting in a flat and 48 μm thick mesh with cavities (Figure 4). The cavities have a width ranging from 16 to 19 μm and a length of around 30 μm. Two pores are ending in each cavity.

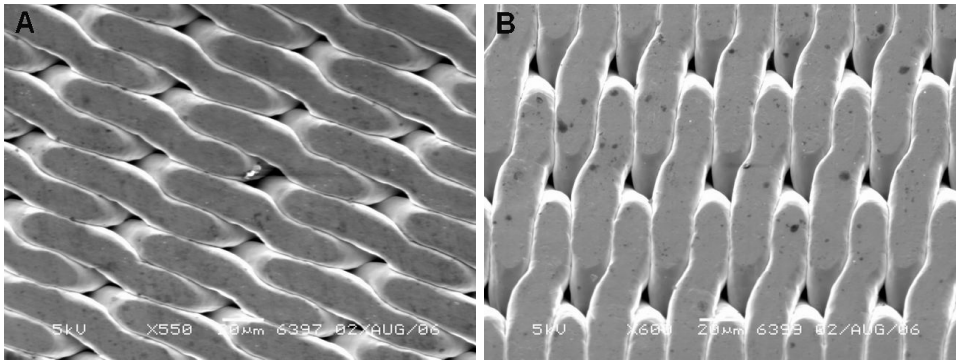

Figure 4: SEM images of a roll compacted stainless steel woven mesh. Front view (A) and under a tilt angle of 30° (B).

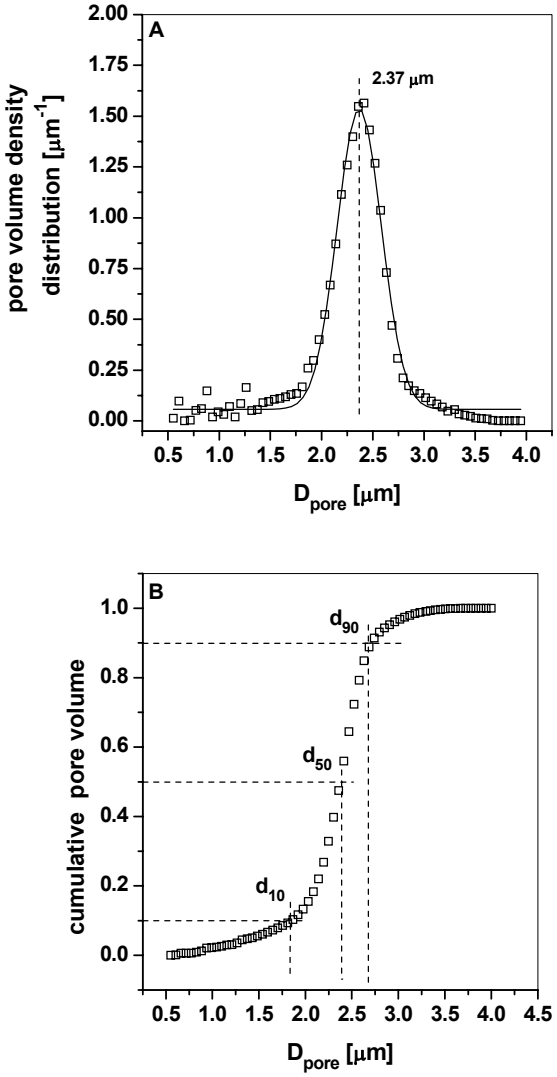

Figure 5: Pore size distribution (A) and cumulative pore volume curve (B) of the roll compacted stainless steel woven mesh.

The pore size of the mesh was measured by the gas-liquid displacement method (Beckmann Coulter Porometer). Figure 5A displays the resulting pore size distribution having a center value of 2.37 μm and span of 0.37. The span of the pore size distribution is defined as follows.

$$Span = \frac{(d_{90} - d_{10})}{d_{50}} \quad (1)$$

The d_{90} value corresponds to the maximum pore diameter, which covers 90 percent of cumulative pore volume, d_{10} covers 10 percent and d_{50} covers 50 percent, as depicted in Figure 5B.

Laser drilling

The perforation of the 25 μm thick aluminum and the 50 μm thick steel sample was performed with a Titanium sapphire laser system with a central wavelength of 800 nm. A seed/oscillator combination (Coherent Vitesse Duo) together with a regenerative amplifier (Coherent RegA9000) delivered a pulse train of 10-250 kHz repetition rate with 1 W average power (at 250 kHz). The pulse length, measured by a second order auto-correlator, was adjusted to 200 fs for all experiments. A λ/4 waveplate was used to convert the horizontally polarized beam into a state of circular polarization. The bundle was manipulated over the sample by use of a two mirror galvo scanner system (Scanlab Scangine 14). A 55 mm f-theta lens (fused silica) focused the beam to a spot size of 25 μm. The holes were drilled by percussion drilling with varying number of incident pulse and pulse energy.

Surface modification

As a pre-treatment, the laser-perforated samples were cleaned and oxidized using a reactive oxygen plasma (Plasmafab 508, Electrotech; 10 min, 500 W, pO_2 = 16 mbar). For the chemical vapor deposition of silane monolayers plasma oxidized metal samples were stored together with a few microliters of FOTS or OTS in a dry sealed glass box. The vapor deposition was carried out at 120°C for 2 hours in a nitrogen flushed oven. Afterwards the nozzle plates were allowed to cool down to room temperature while staying in the oven followed by a stabilization step at 100°C for 1 hour. The modification process was finished by extensively rinsing with iso-propanol, then with ultra pure water and dried with nitrogen. Aluminum samples were coated with FOTS and the steel foil with OTS. To quantify the

hydrophobization, static water/air contact angles were measured with a goniometer (OCA 15, Data Physics).

Emulsification set-up

The emulsification set-up used here to observe the drop formation as well as the settings and procedures to start, perform and analyze the experiments were the same as reported before [15]. These procedures were also adapted to oil-in-water emulsification experiments. Two essential points for oil-in-water experiments are, that nozzle plates are cleaned and oxidized using a reactive oxygen plasma (Plasmafab 508, Electrotech; 10 min, 500 W, pO_2 = 16 mbar) and that the continuous phase should be fed first into the system resulting in a negative pressure difference and therefore permeation of water through the nozzle plate. This ensures that the nozzle plate is fully wetted by the continuous phase.

5.4 Results

Laser drilling

In the aluminum foil one row of 20 holes was drilled with a distances of 100 μm between the holes, especially designed for membrane emulsification. At first a steel sample was fabricated to check the feasibility of laser drilling of steel. For this purpose more than 50 rows with several tens of holes were drilled. The minimum distance between the rows and the holes within a row was 50 μm. Secondly, a steel sample with 100 holes arranged in an array of 10 times 10 holes with a hole-to-hole distance of 150 μm was fabricated.

The average hydraulic diameters ($D_{hydraulic}$) of the drilled holes on the exit and entrance side in aluminum and stainless steel foils determined from optical images are shown in Table 1. The values were calculated from the cross-sectional area (A_{cross}) and the perimeter (P) according to the following equation:

$$D_{hydraulic} = \frac{4\ A_{cross}}{P} \qquad (2)$$

The cross-sectional areas and the perimeters were obtained from the outlined shapes of the holes and calculated by the imaging software of the used microscope system (Zeiss Axiovert).

Table 1: Calculated average hydraulic diameters of the laser-drilled holes in 25 μm thick aluminum foil and 50 μm thick stainless steel foils.

	Aluminum foil	Stainless steel foil	
		Sample 1	Sample 2
Entrance side [μm]	17.8 ± 0.8	38.0 ± 3.0	21.8 ± 0.7
Exit side [μm]	6.0 ± 0.3	10.5 ± 3.3	4.3 ± 0.4

The shape of the holes on the entrance side were elliptic in contrast to the exit side where the holes had somewhat more irregular shapes, which can be seen in the SEM-Images of the laser-drilled steel sample displayed in Figure 6A and 6B.

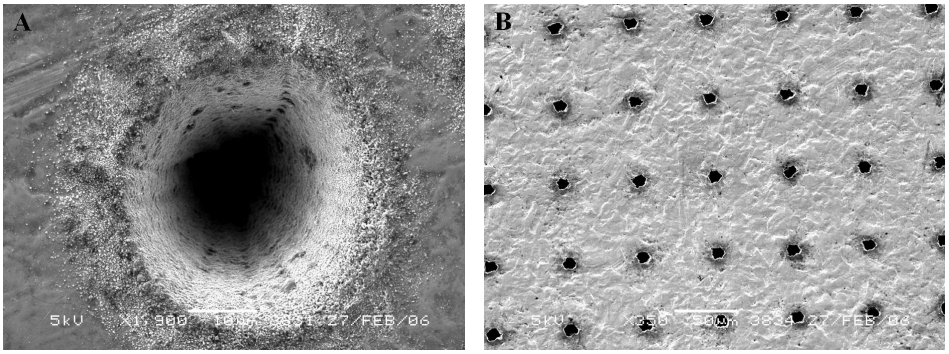

Figure 6: SEM-images of the first laser-drilled steel sample. Single hole on the beam entrance side (A) and array of holes on the beam exit side (B).

The exit and entrance hole diameter distributions of the first laser-drilled stainless steel sample are shown in Figure 7A. The mean diameters obtained from Gaussian fits are 12.2 μm for the exit holes, which is higher than the arithmetic diameter in Table 1, and 38.0 μm for the entrance holes, respectively. As already indicated by

the high standard deviation, the distribution of the exit holes has a span of 0.36. This is comparable to SPG membranes, which have pore size distributions with spans between 0.29 and 0.7 [27]. From visual inspections the reason for this high span value was found in the fact that quite a number of holes were not completely drilled through and only partly open.

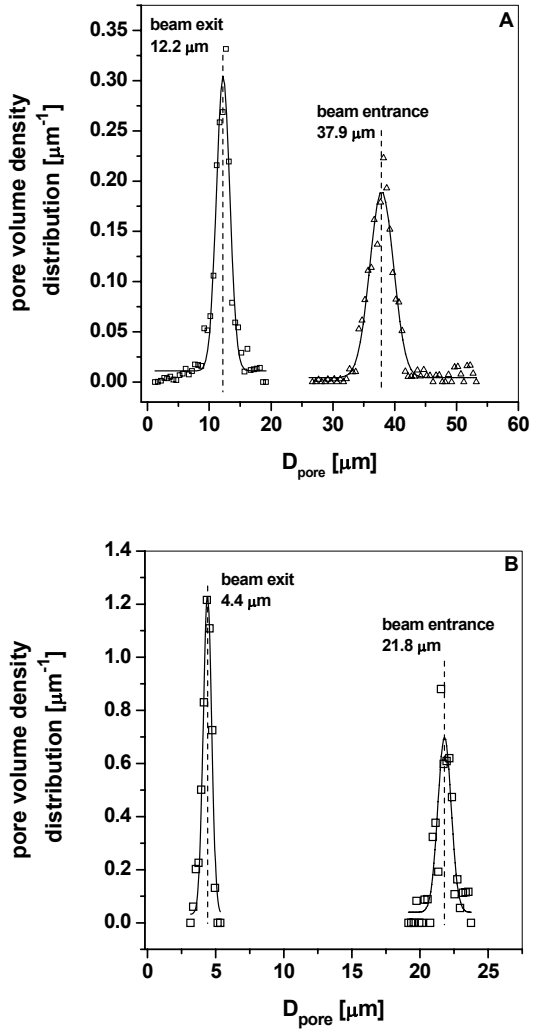

Figure 7: Distribution of the exit and entrance hole diameters of the laser-drilled stainless steel samples (A: First sample; B: Second sample).

The second stainless steel sample could be fabricated with a higher precision. As Figure 7B shows the exit diameter decreased to 4.4 μm. The span of the exit hole diameter distribution was decreased to 0.2 and the standard deviation from around 30 percent for the first sample down to 8 percent. This is quite an improvement, but still eight times larger compared to silicon nitride micro-nozzle plates.

Contact angles

The surface modification of the aluminum and steel samples was successfully as indicated by the measured water/air contact angles (CA) shown in Table 2. The FOTS modified samples are in agreement with silicon nitride samples modified with the same silane. The OTS coated stainless steel showed a somewhat smaller water/air contact angle compared to OTS modified silicon nitride [28]. It might be caused by a less ordered or less dense monolayer on stainless steel, which has a grainy structure of different oxides, compared to a smooth and homogeneous artificial silicon oxide layer on silicon nitride.

Table 2: Water/air contact angles on hydrophobized aluminum and stainless steel.

	Water/air CA [°]
FOTS modified aluminum	112.5 ± 0.8
OTS modified stainless steel	100.1 ± 3.2

Contact angles of water drops on modified samples while immersed in hexadecane containing 1 wt% of the surfactant Span85 were in both cases higher than 150° This is sufficiently high to perform successful emulsification of water into oil [29].

Water-in-oil emulsification with the FOTS coated Aluminum nozzle plate

At first an emulsification experiment was performed with the exit holes of the aluminum nozzle plate towards the continuous phase. Within this experiment two different cross-flow velocities of 0.042 m/s and 0.074 m/s were investigated. The

drop formation rate was not significantly affect by different velocities, as it can be clearly seen from Figure 8. The critical Laplace pressures ($P_{critical}$) determined from the linear regression lines in Figure 8 were 20.56 mbar and 25.36 mbar for 0.042 m/s and 0.074 m/s respectively. Considering the average hydraulic diameter of the exit holes of 6.0 μm this corresponds to interfacial tensions (γ) of 3.78 mN/m and 3.06 mN/m, respectively, calculated via equation 3 assuming that the diameter of the hemispherical dispersed phase cap at the hole exit is equal to the hydraulic diameter ($D_{hydraulic}$) of the exit hole.

$$\gamma = \frac{P_{critical}\ D_{hydraulic}}{4} \tag{3}$$

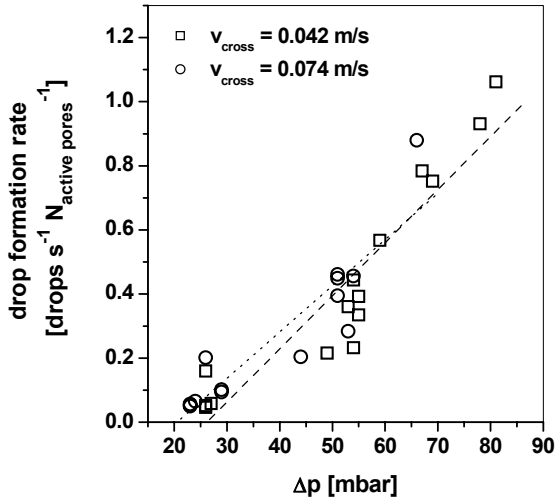

Figure 8: Drop formation rate achieved during water-in-hexadecane emulsification at different pressure differences.

The number of active pores varied between 80 and 90 percent independently from the pressure and reached already at the lowest applied pressures in opposite to conventional membranes.

A lag time between two drop formations was observed here as well. As Figure 9A clearly displays, a significant influence of the cross-flow velocity could not be found.

Therefore, the surfactant transport towards the liquid-liquid interface at the exit holes during the lag time is diffusion controlled. The calculated Reynolds numbers of below 20, which is clearly within the laminar flow regime, supports this finding.

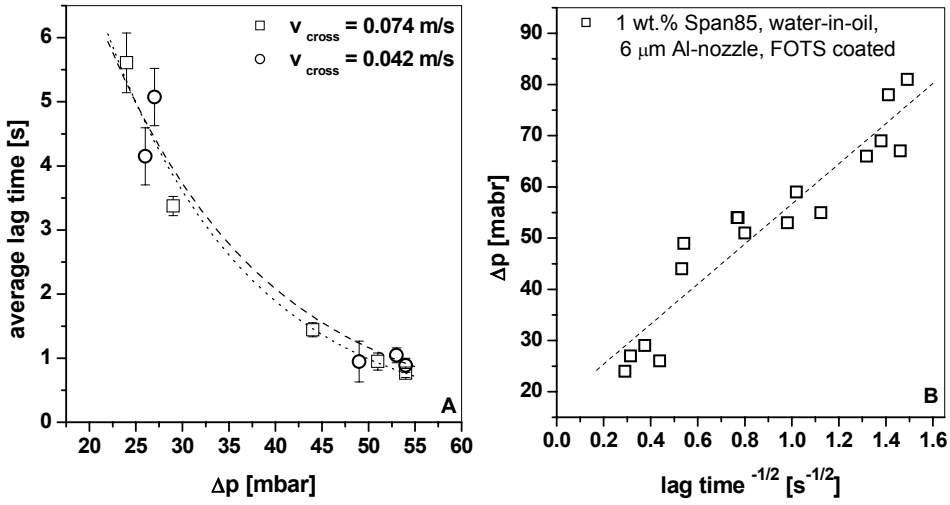

Figure 9: Lag time versus pressure difference for two different cross-flow velocities (A). Relationship between the applied pressure difference and the negative square root of the lag time (B).

The observed lag time for both cross-flow velocities exhibits also a linear relationship between the negative square root of the lag time and the applied pressure difference (see Figure 9B) as it was found for the water-in-oil emulsification reported in Chapter 4.

The most interesting finding was the observation of two different drop formation processes. At first the shear force induced drop formation could be observed at 2/3 of the exit holes at all applied pressures. The resulting drop sizes were ranging from 140 to 170 μm for the higher velocity and from 180 to 210 μm for the lower velocity. The coefficients of variation were 7 and 10 percent, respectively. Figure 10 displays the drop size as a function of the applied pressure difference for two velocities. It can be seen that for 0.074 m/s the drop size increases significantly at pressures above 50 mbar.

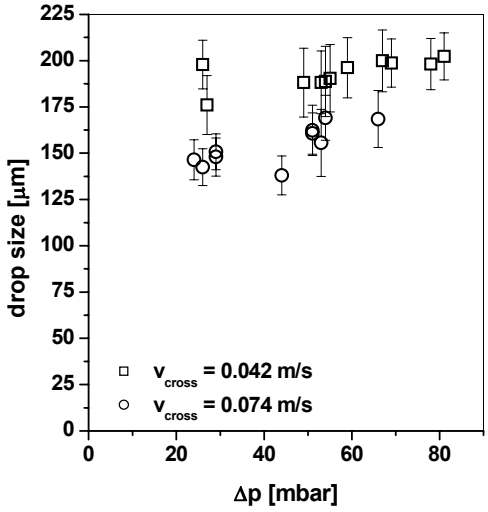

Figure 10: Average drop size of shear induced formed water drops versus applied pressure difference (Δp) at two different cross-flow velocities (v_{cross}).

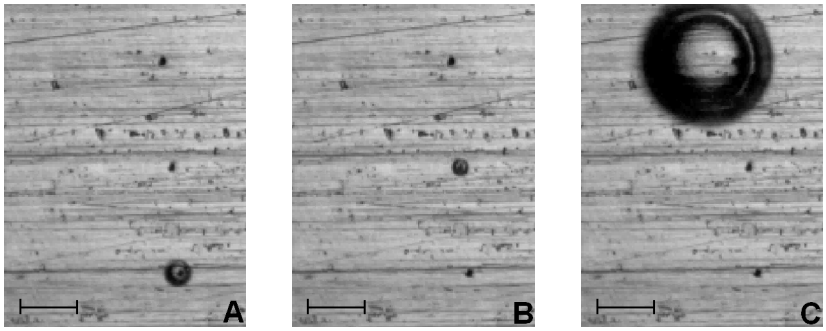

Figure 11: Spontaneous drop formation (Δp = 23 mbar, v_{cross} = 0.074 m/s) at three different holes. The scale bar represents 50 μm. The pictures were taken one frame before the drop detachment.

At pressures below 60 mbar some of the exit holes were forming water drops by the spontaneous drop formation process. Figure 11 shows the spontaneous formation at three different holes. Two holes are forming drops with diameter of 28 μm (A, B) and one produces drops of 76 μm (C). As Figure 12A shows, the drop size increased with increasing pressure difference independently from the cross-flow velocity. One

characteristic of the spontaneous drop formation is the independency of the drop diameter from the cross-flow velocity of the continuous phase. This can be clearly seen in Figure 12A that drops formed at around 55 mbar and three different cross-flow velocities have nearly the same diameter. Coefficients of variation below 5 percent were obtained at pressure differences smaller than 26 mbar. The spontaneous drop formation occurred at maximum at 5 holes but not all of these 5 holes were producing the same drop size. The drop size distribution shown in Figure 12B is obtained from drops produced by 4 holes (marked data points in Figure 12A). Each peak represents drops inflated from two holes.

In microchannel emulsification, the effect of increasing the applied pressure within the spontaneous drop formation process is characterized as follows. From the critical pressure until a certain pressure, drops with a constant diameter are produced. Above this range the drop size increases resulting finally in a continuous out-flow of the dispersed phase. Within the drop size stable zone the number of drop forming microchannels increases with increasing pressure reaching a maximum at certain pressure, while the flow velocity of the dispersed phase in the active microchannels does not change dramatically [2]. When the maximum number of active channels is reached and the pressure is further increased, the flow velocity also increases. The spontaneous drop formation process is driven by Laplace pressure differences. Therefore, the interfacial tension is the dominating effect. At a certain flow velocity of the dispersed phase viscous forces become dominant resulting in a continuous out-flow of the dispersed phase. At higher cross-flow velocities of the continuous phase the out-flowing dispersed phase would be sheared of as droplets like in membrane emulsification. By increasing the applied pressure difference and the cross-flow velocity of the continuous phase the drop formation process can be changed from spontaneous to shear-induced.

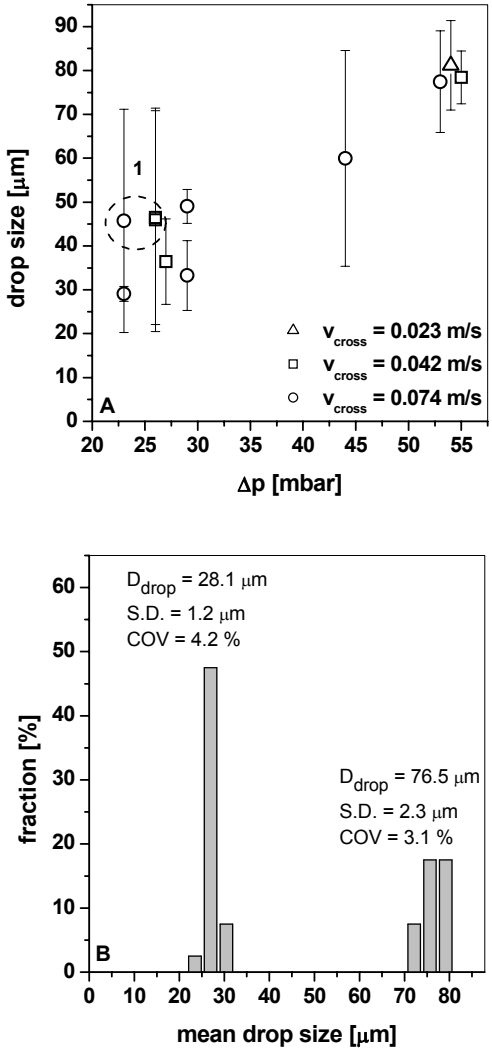

Figure 12: Average size of water drops formed by the spontaneous drop formation process versus the applied pressure difference (Δp) at three different cross-flow velocities (A); Drop size distribution for the marked data points in graph 12A showing a bimodal distribution (B).

To describe this transition Sugiura et al. introduced a critical Capillary number.

$$Ca_{critical} = \frac{viscous\ force}{interfacail\ tension\ force} = \frac{\eta U_{critical}}{\gamma} \qquad (4)$$

Where η is the dispersed phase viscosity, $U_{critical}$ the critical dispersed phase velocity and γ the liquid-liquid interfacial tension. Above $Ca_{critical}$ the velocity of the dispersed phase results in a domination of the viscous force over the interfacial tension force and below vice versa. The dimensionless drop diameter, which is the droplet diameter divided by depth of the microchannels, is constant below $Ca_{critical}$ and above it increases [30]. The same argumentation can be applied to the straight-through microchannel emulsification. Also there, the drop size stays constant for a certain pressure range and increases dramatically if the pressure is increased further. Kobayashi et al. explained this observation as well by the critical Ca number [31].

In Figure 13 the average drop diameter of spontaneous and shear-induced formed drops is plotted against the dispersed phase flow obtained from the inflation time of the drops and their average diameter. It can be seen that the flow for the spontaneous formed drops is by a factor 10 to 100 smaller than for shear-induced formed drops. Both data points representing the spontaneous formed drops were obtained at two different cross-flow velocities. The pressure difference was constant at 24 mbar for the spontaneous formed drops (data points 1 and 2) therefore only the geometry of the laser-drilled holes is responsible for the different drop sizes. From optical analysis no significant differences in geometry could be found.

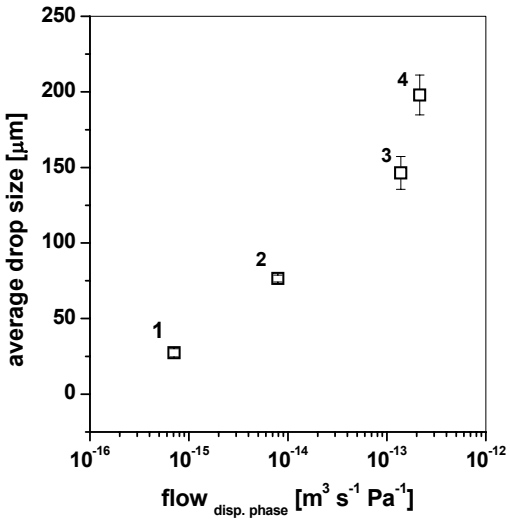

Figure 13: Average drop size of water drops formed by the spontaneous (1, 2) and the shear induced drop formation process (3, 4) versus dispersed phase flow. Spontaneously formed drops inflated at 24 mbar and at two different cross-flow velocities. Shear induced drops formed at 24 mbar, v_{cross} = 0.074 m/s (3) and at 26 mbar, v_{cross} = 0.042 m/s (4).

As mentioned before the laser-drilled holes are conical in shape having a wider opening on the beam entrance side than on the exit side. To check if the tapering has an influence on the drop formation process emulsification experiments were conducted with the beam entrance side towards the continuous phase. For this purpose the same nozzle plate was used. After removing the nozzle plate from the holder, it was cleaned by oxygen plasma and coated as well with FOTS.

In general, comparable observations were made as in the experiment with the beam exit side towards the continuous phase. One third of the active holes were producing drops with average diameters ranging from 19 to 21 µm with a COV of 3 to 5 percent attributed to the spontaneous drop formation process. The remaining holes were forming drops according to shear induced drop formation with an average drop size of 195 µm and a COV of 15 percent.

We assume that the geometry of the drilled holes is not defined enough to ensure only spontaneous drop formation. For this purpose elongated holes should be fabricated similar to straight-through microchannel plates. We could prove the ability

of laser ablation to fabricate relatively precise geometries in aluminum foil used as emulsification device, forming drops either according to the shear-induced or spontaneous formation process. Beside the limitations of the geometry also the viscosity of the dispersed phase (water) can be considered as a limiting factor. Low viscosity liquids are flowing faster through a constriction compared to liquids with a higher viscosity under the same applied pressure difference. Therefore, the critical Ca-Number is reached sooner resulting in shear-induced drop formation. Kobayashi et al. also observed this restriction to viscous liquids in their work. For straight-through MC plates, following the design shown schematically in Figure 2, the formation of monodispersed decane drops was not possible. Only with a new MC plate design offering more space for the dispersed phase to expand within the slits, monodispersed decane drops could be produced [10]. Kawakatsu et al. studied the influence of the viscosity of the dispersed phase. In their study water-in-oil emulsification with alkyl-alkoxy silane modified silicon microchannels (as depicted in Figure 1) was performed by varying the viscosity of water by adding different amounts of sucrose. They found, that with increasing viscosity the average diameter of the produced drops decreases and as well as the COV [32].

Water-in-oil emulsification with OTS coated stainless steel nozzle plates

In this experiment the emulsification performance of the laser-drilled stainless steel nozzle plate no. 1 (38 μm entrance, 10.5 μm exit) for the production of water-in-oil emulsions was investigated. Here, the beam entrance side was facing the continuous phase. Water permeation and drop formation occurred already at an applied pressure difference of 5 mbar. These drops were hundreds of micrometer in size. At slightly higher pressures huge drops were formed floating together resulting in a body of water covering nearly the whole observed area.

The water flow through the holes was far above the critical velocity for the spontaneous drop formation and even too high for stabilizing the drops against coalescences by surfactant adsorption. Therefore, the following experiments were conducted in the oil-in-water modus.

Oil-in-water emulsification with oxidized stainless steel nozzle plates

Within these experiments laser-drilled oxygen plasma pre-treated stainless steel nozzle plates were used to emulsify sunflower oil into 1 wt% Tween20 aqueous solution. At first sample 1 (38/10 μm) was investigated. The beam exit side was facing the continuous phase having the hole size distribution displayed in Figure 7A. As expected, the drop formation rate increased with increasing applied pressure difference. Because of the broad hole size distribution and different observed locations at different optical magnifications during the experiment, the formation rate shows scattering values (see Figure 14).

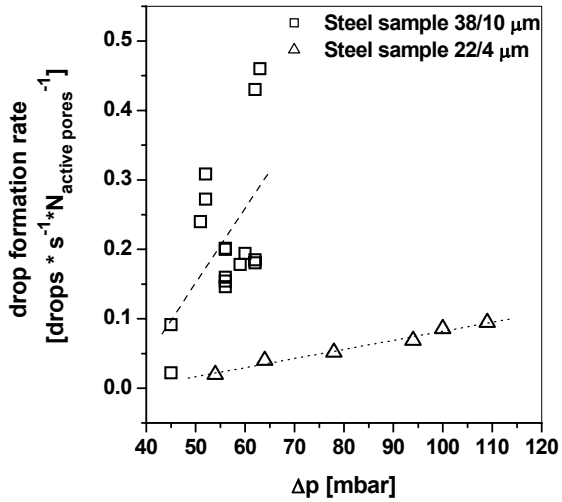

Figure 14: Formation rate of sunflower oil drops emulsified into 1wt% Tween20 aqueous solution with laser-drilled stainless steel foils. Results shown for steel sample 38/10 μm and 22/4 μm.

Here as well, both types of drop formation processes could be observed. Shear-induced drops with an average diameter of 143 μm with a COV of 24 percent were produced. The spontaneously formed drops had an average diameter of 48 μm with a COV of 20 percent and were 4.6 times larger than the average hydraulic diameter of the holes. A significant influence of the applied pressure difference on the drop size could not be found as Figure 15A indicates.

The number of holes forming spontaneously drops decreased with increasing pressure. The ratio of shear-induced forming holes to spontaneously increased from around 1 to 13 at the highest applied pressure. This is correlated to an increasing pore flow resulting in higher Ca-numbers.

The high COV values for shear-induced and spontaneously formed drops seem to be a result of the broad hole diameter distribution resulting in broad drop size distributions. Figure 16A shows the drop size distribution obtained from all produced drops regardless of the applied pressure divided into spontaneously and shear-induced formed drops. The first peak representing spontaneously formed drops has a span of 0.52. The size distribution of shear-induced formed drops shows is very broad as well and has span of 0.4, which corresponds to the span of the pore size distribution of 0.36 for sample 38/10 μm.

The obtained results for spontaneously formed drops are comparable to results from Tong et al. [33]. In their study, microchannel plates were fabricated by dicing channels into a stainless steel plate. The average hydraulic diameter of the diced microchannels was 16.4 ± 2.5 μm. The microchannel plate was used to emulsify sunflower oil into an aqueous solution of 0.3 wt% pentaglycerol monolaurate. Unfortunately, only drop diameters for a single microchannel are given. However, based on the reported ratio of the drop diameter to the microchannel diameter of 2.61, drop diameters for all microchannels were calculated resulting in an average drop diameter of 42.8 μm. The COV of these drops was 15 percent. The COV for drops formed at a single microchannel was below 3 percent. Both, the drop diameter and the COV, are in the same range for spontaneously formed drops, as obtained here with the laser-drilled stainless steel nozzle plate.

This experiment clearly showed that the fabrication of laser-drilled stainless steel nozzle plates has to be improved in terms of a more defined geometry and an improved hole size distribution in order to achieve smaller COV values. To promote only the spontaneous drop formation the hole geometry should be changed into a more elliptical shape.

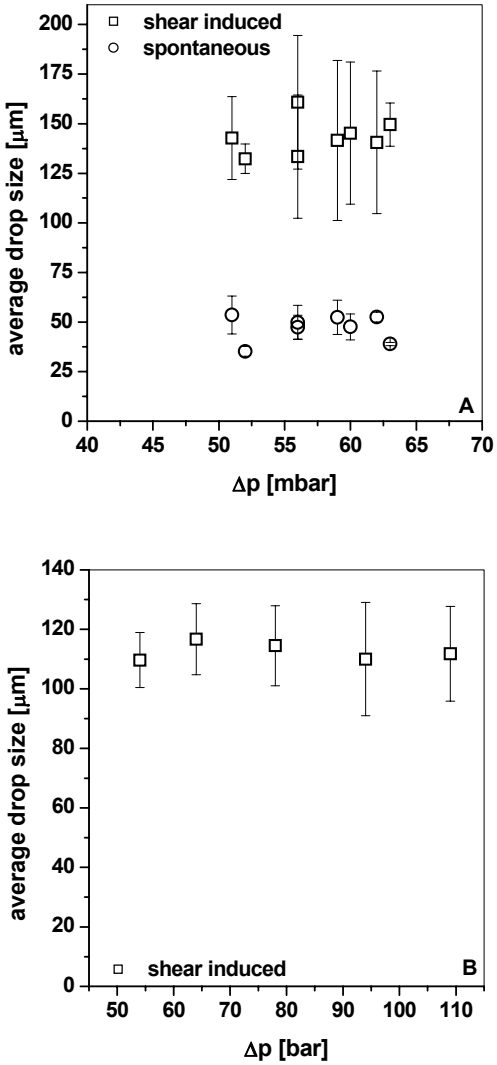

Figure 15: Obtained sunflower oil drop sizes for shear induced and spontaneous formed drops for sample 38/10 μm (A) and shear induced drops for sample 22/4 μm (B) versus the applied pressure difference (Δp).

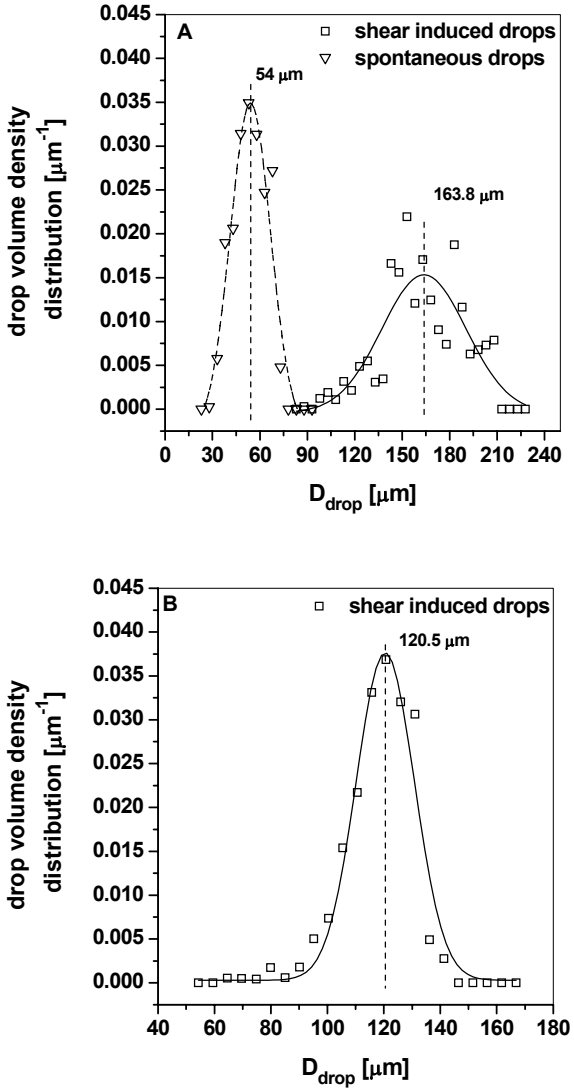

Figure 16: Drop size distribution of spontaneous and shear induced formed drops for steel sample 38/10 µm (A) and steel sample 22/4 µm (B).

An improvement of the precision was achieved within sample 22/4 µm, which had, as already shown in Figure 7B, smaller exit holes and a more narrow hole size distribution. With this steel nozzle plate, an emulsification experiment was performed in a similar way. As before, both types of drop formation occurred, but here, the

fraction of spontaneous drop forming holes was less compared to sample 38/10 μm. This might be a result of the higher precision of the drilled holes. The drop formation rate, shown in Figure 14 for sample 22/4 μm, was smaller compared to sample 38/10 μm, which is a result of the smaller exit hole size. The resulting drop size as a function of the applied pressure is depicted in Figure 15B and clearly shows no significant influence of the pressure. Only the COV increased slightly from below 10 percent to over 15 percent. This is related to the increase of the number of active pores, rising from 40 to 90 percent, and therefore the mutual influence of growing and detaching drops increases as well. The average drop size regardless of the applied pressure was 112.5 μm with COV of 14 percent, which is strongly reduced compared to the obtained 24 percent for steel sample 38/10 μm. This becomes even clearer, if the drop size distributions for the shear-induced drops are compared as shown in Figure 16. From sample 22/4 μm a much more narrow drop size distribution was obtained having a span of 0.24, which reflects the exit hole size distribution of sample 22/4 μm. In Figure 17 a snapshot of the obtained sunflower oil drops is shown. It displays the high number of active pores (>80 percent) reached at a pressure difference of 100 mbar.

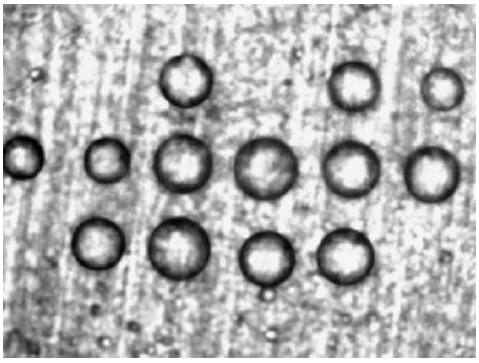

Figure 17: Sunflower oil drops inflated at 100 mbar pressure difference from the holes drilled in steel sample 22/4 μm with a hole-to-hole distance of 150 μm.

The spontaneously formed drops had diameters from approximately 10 μm at the lowest applied pressure to 35 μm at the highest applied pressure. Regarding single

holes producing spontaneously drops, the COV of these drops were smaller than 5 percent at pressure below 94 mbar. Above this pressure the COV for spontaneously formed drops from single holes increased up to 20 percent.

In the experiments with both steel nozzle plates a lag time was observed. As Figure 18 depicts, a linear relationship between the applied pressure difference and the negative square root of the lag time was found.

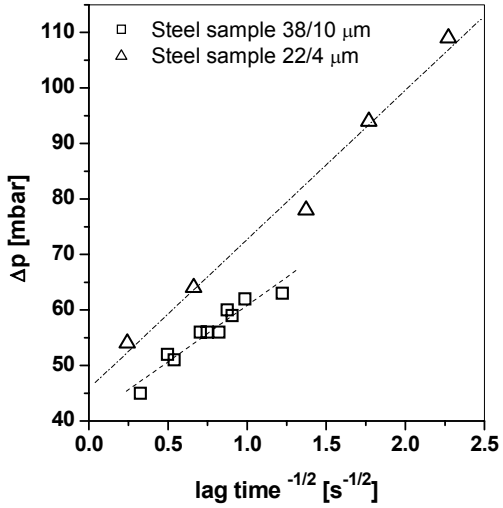

Figure 18: Applied pressure difference as a function of the negative square root of the lag time observed for sunflower oil emulsified into 1 wt% aqueous solution of Tween20.

Emulsification with hydrophobized stainless steel mesh

In this section the results of water-in-hexadecane emulsification with a hydrophobic woven stainless steel mesh are discussed. The mesh has a quite regular structure of cavities as shown in Figure 5. It was hydrophobized with OTS following the standard procedure.

Emulsification started at a pressure difference of 40 mbar. Assuming an equilibrium interfacial tension of 1 wt% Span85 of 3.5 mN/m the largest pore diameter is equal to 3.5 μm. Here as well, both types of drop formation were observed. The shear-induced drops had diameters of 100 to 150 μm. The ratio between shear-induced and spontaneously forming cavities was valued to be around one. From the optical

observations it could be clearly identified that the drop formation occurred in the cavities and the drops were released by being pushed out of the cavities by a newly formed drop. Figure 19 shows released drops and drops still located within the cavities.

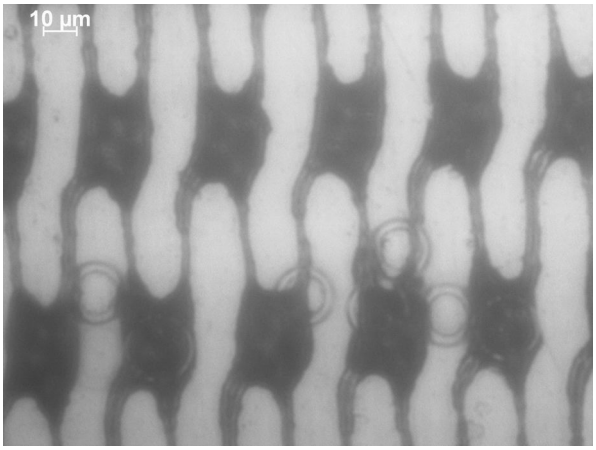

Figure 19: Spontaneous water drop formation from the cavities of the woven stainless steel mesh. The continuous oil phase flows from right to left.

From the experiments with the laser-drilled aluminum nozzle plate it is known that the size of spontaneous formed drops increases with increasing pressure. Here, we also found this but not as well pronounced. The average drop size increased only from 19 to 23.5 µm while the COV exceeded 10 percent as depicted in Figure 20.
A similar experiment was conducted with an unmodified stainless steel mesh. Here as well, both types of drop formation processes could be observed. The spontaneous formed water drops had an average drop size of 17.2 µm and a COV of 10 percent in a pressure range from 99 to 114 mbar. In contrast to the experiment with the OTS modified mesh, the spontaneous drop formation could not be restored after increasing the pressure to value, at which only shear-induced drop formation occurred. After only shear-induced drops were formed from a cavity, it is likely, that the cavity is fully filled and wetted with water. If the pressure is decreased again the

continuous oil phase is not able to enter and wet the surface of the cavity. However, an oil wetted surface is one major requirement for the spontaneous drop formation.

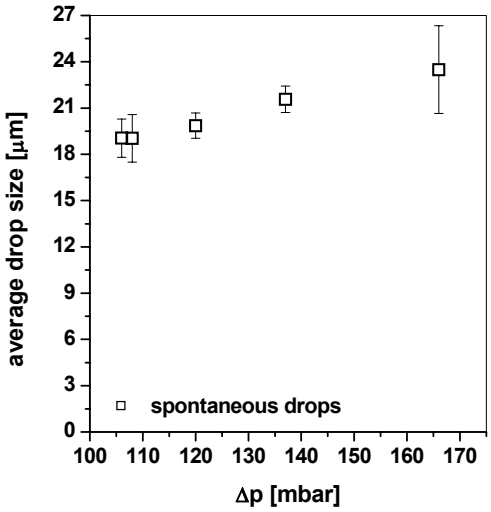

Figure 20: Drop size of spontaneously formed drops versus applied pressure difference (Δp) obtained from water-in-oil emulsification with the woven stainless steel mesh.

5.4 Conclusions

We could successfully demonstrate the fabrication of laser-drilled metal nozzle plates with a relatively high accuracy. The laser-drilled metal nozzle plates with hole diameters ranging from 4.4 to 10.5 µm and pore size distributions with spans from 0.2 to 0.36 were performing successfully water-in-oil and oil-in-water emulsifications. Within these experiments spontaneous and shear force induced drop formation was observed. The first drop formation process is attributed to the deviation of the exit hole from the circular shape. The drop size distributions of the shear-induced drops are displaying clearly the pore size distributions of the used nozzle plates. The obtained COV are 7 to 25 percent depending on the used nozzle plate and are comparable to results from silicon nitride micronozzle plates. Compared to microchannel and straight-through microchannel emulsification the laser-drilled metal nozzle plates are less defined to ensure only spontaneous drop formation.

Nevertheless, there is still the opportunity to fabricate metal nozzle plates having slits instead of more or less circular holes. Laser-drilled metal nozzle plates are an alternative for silicon nitride micro nozzle plates, conventional microporous glass, and ceramic membranes and can be used for water-in-oil and oil-in-water emulsification.

Beside the laser-drilled metal nozzle plates a conventional roll compacted metal mesh was used for water-in-oil emulsification. Here as well, both types of drop formation were observed, which can also be addressed to the less defined geometry. Therefore, it can not compete with the cleanroom fabricated devices producing drops with COV values below 5 percent via the spontaneous formation process, but for producing small drops (< 50 μm) with COV values of about 10 percent it is an alternative.

5.5 Acknowledgements

The work was sponsored by Dutch government in the framework of the BISK program MicroNed. The laser-drilling was performed at the Laboratory of Mechanical Automation by Max N.W. Groenendijk (Applied Laser Technology, Department of Mechanical Engineering, University of Twente).

5.6 Abbreviations

COV	Coefficient of variation
ECD	Electro-chemical micro drilling
FOTS	perfluorinated octyltrichlorosilane
MC	Microchannel
OTS	Octyltrichlorosilane
SDS	Sodium dodecylsulfate
SPG	Shirasu porous glass

5.7 References

[1] T. Kawakatsu, Y. Kikuchi, M. Nakaijma, JAOCS 74 (1997) 317-321

[2] S. Sugiura, M. Nakajima, J. Tong, H. Nabetani, M. Seki, J. of Colloids and Interface Sci. 227 (2000) 95-103

[3] T. Kawakatsu, G. Trägårdh, C. Trägårdh, J. of Food Engineering 50 (2001) 247-254

[4] S. Sugiura, M. Nakajima, S. Iwamoto, M. Seki, Langmuir 17 (2001) 5562-5566

[5] J. Tong, M. Nakajima, H. Nabetani, Eur. J. Lipid Sci. Technol. 104 (2002) 216-221

[6] I. Kobayashi, M. Nakajima, K. Chun, Y. Kikuchi, H. Fuijata, AIChE Journal 48 (2002) 1639-1644

[7] I. Kobayashi, M. Nakajima, Eur. J. Lipid Sci. Technol. 104 (2002) 720-727

[8] I. Kobayashi, S. Mukataka, M. Nakajima, Ind. Eng. Chem. Res. 44 (2005) 5852-5856

[9] I. Kobayashi, S. Mukataka, M. Nakajima, Lamgmuir 21 (2005) 5722-5730

[10] I. Kobayashi, S. Mukataka, M. Nakajima, Langmuir 21 (2005) 7629-7632

[11] Nano and Micro Engineered Membrane Technology, Chapter 11: Membrane Emulsification, C.J.M. van Rijn, Elsevier Amsterdam, 2004 ISBN 0.444-51489-9.

[12] Stein Kuiper, Ph.D. Thesis, University of Twente, Enschede, The Netherlands, 2000, ISBN 90-36514754

[13] A.J. Abrahamse, R. van Lierop, R.G.M. van der Sman, A. van der Padt, R.M. Boom, J. Membr. Sci. 204 (2002) 125-137

[14] S. van der Graaf, C.G.P.H Schroën, R.G.M van der Sman, R.M. Boom, J. Colloid Interface Sci. 277 (2004) 456-463

[15] M.J Geerken, Chapter 4 of this thesis

[16] J. Chae, S.S. Park, T. Freiheit, Int. J. of Machine Tools & Manufacture 46 (2006) 313-332

[17] M. Sen, H.S. Shan, Int. J. of Machine Tools & Manufacture 45 (2005) 137-152

[18] B.H. Kim, S.H. Ryu, D.K. Choi, C.N. Chu, J. Micromech. Microeng. 15 (2005) 124-129

[19] S.H. Ahn, S.H. Ryu, D.K. Choi, C.N. Chu, Precision Engineering 28 (2004) 129-134

[20] B.N. Chichkov, C. Momma, S. Nolte, F. von Alvensleben, A. Tünnermann, Appl. Phys. A 63 (1996) 109-115

[21] M. Okoshi, N. Inoue, Appl. Phys. A 79 (2004) 841-844

[22] C.K. Chung, Y.C. Lin, G.R. Huang, J. Micromech. Microeng. 15 (2005) 1878-1884

[23] M. Bowden, O. Geschke, J.P. Kutter, D. Diamond, Lab Chip 3 (2003) 221-223

[24] M. Womack, M. Vendan, P. Molian, Applied Surface Science 221 (2004) 99-109

[25] M. Ostermeyer, P. Kappe, R. Menzel, S. Sommer, F. Dausinger, Appl. Phys. A 81 (2005) 923-927

[26] M. Kohno, Y. Matsuoka, JSME International Journal Series B 47 (2004) 497-500

[27] G.T. Vladisavljevic, M. Shimizu, T. Nakashima, J. Membr. Sci. 250 (2005) 69-77

[28] M.J. Geerken, T.S. van Zanten, R.G.H Lammertink, Z. Borneman, W. Nijdam, C.J.M. van Rijn, M. Wessling, Advanced Eng. Materials 6 No. 9 (2004) 749-754

[29] M.J. Geerken, R.G.H. Lammertink, M. Wessling, Colloids and Surfaces A (2006) doi:10.1016/j.colsurfa.2006.06.30

[30] S. Sugiura, M. Nakajima, N. Kumazawa, S. Iwamoto, M. Seki, J. Phys. Chem. B 106 (2002) 9405-9409

[31] I. Kobayashi, M. Nakajima, S. Mukataka, Colloids and Surfaces A 229 (2003) 33-41

[32] T. Kawakatsu, G. Trägårdh, C. Trägårdh, M. Nakajima, N. Oda, T. Yonemoto, Colloids and Surfaces A 179 (2001) 29-37

[33] J. Tong, M. Nakajima, H. Nabetani, Y. Kikuchi, Y. Maruta, J. Colloid Interface Sci. 237 (2001) 239-248

Chapter 6

Fabrication of perforated polymer films by phase separation micromolding for membrane emulsification

Abstract

In this chapter the fabrication of perforated polymer films obtained by phase separation micromolding is described. We observed that a known standard recipe to create high porosity microsieves could not be applied to the fabrication of low porosity microsieves. This standard recipe based on polyethersulfone was advanced to create defect free films for oil-in-water emulsification. The perforated films had slightly deformed pores with hydraulic diameters of around 5 μm. To successfully emulsify sunflower oil into a Tween20 containing aqueous phase, the hydrophilicity of PES films had to be increased by oxygen plasma treatment and using sulfonated poly-ether-ether-ketone (SPEEK) as a hydrophilic additive.

6.1 Introduction

Micro-engineered nozzle plates for emulsification purposes can be fabricated in different ways and from different materials. Semi-conductor materials like silicon and silicon nitride have been used to create well defined micro-nozzle plates for emulsifying oil-in-water [1,2] and water-in-oil [3]. The fabrication of this kind of nozzle plates requires several steps of cost intensive cleanroom micro-engineering tools.

An economical less intensive and faster tool is laser micro drilling. With this technique metal or polymer foils can be perforated down to hole diameters of 3 μm [4]. Laser perforated metal foils were applied in water-in-oil and oil-in-water emulsification [5]. The hole geometry is not as precise and has a wider hole size distribution compared to silicon nitride nozzle plates.

Phase separation micromolding is another way to achieve perforated hole structures. It combines the precision of cleanroom technologies with the low cost fabrication of macroporous polymer membranes. Phase separation is a well known technique to produce porous polymer membranes [6]. A polymer solution of a certain composition is thermodynamically destabilized by introducing a polymer non-solvent, which is miscible with the polymer solvent. Consequently, the solution phase separates and the polymer solidifies resulting in a polymer phase and a solvent/non-solvent phase. Depending on the polymer, the solvent/non-solvent pair and the phase separation conditions the membrane structure can be tuned in a desired way.

In phase separation micromolding the polymer solidification is conducted on a micro-structured mold. This was first demonstrated by Vogelaar et al. [7,8]. They fabricated perforated polyimide films via phase separation micromolding on silicon molds with pillars of 2 to 5 μm in width and approximately 20 μm in height. To achieve a fully perforated film it is of great importance to cast a very thin and uniform polymer film over the mold. Therefore, a casting machine is used allowing to adjust the casting height on a micrometer scale. Figure 1 depicts schematically the whole phase separation process. After the film casting (Fig. 1A), the mold is placed into the non-solvent bath (Fig. 1B), where the liquid polymer film undergoes the phase

separation process. It solidifies while the solvent is exchanged with the non-solvent. The solidification is coupled with shrinkage of the film normal to the mold surface. During the shrinkage the pillars punch through the film. Slight lateral shrinkage of the film occurs as well. This promotes the lift-off of the perforated film from the mold as shown in Figure 1C.

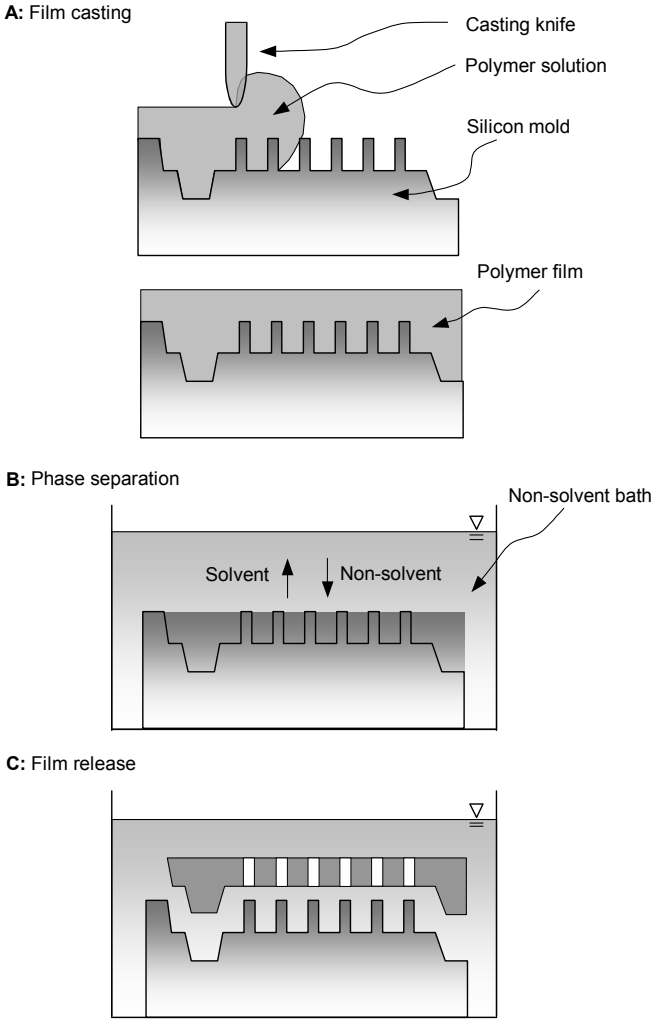

Figure 1: Schematic representation of the phase separation micromolding process. Casting over a microstructured silicon mold (A), phase separation within the non-solvent bath (B) and release of the perforated film from the mold (C).

In order to wash out residual solvent, the perforated film stays for a certain period of time in the non-solvent bath. Finally, the film is removed from the bath and dried.
To achieve a fully perforated film without surface defects, several parameters like composition of the casting solution, casting temperature, casting height and non-solvent bath have to be optimized. Gironès et al. optimized all these parameters to obtain fully perforated polymer films (microsieves) for microfiltration applications [9]. They used a volatile co-solvent (acetone) in the casting solution, which was evaporated after casting in a vapor bath with a continuous water saturated nitrogen flow at a certain temperature. Beside the evaporation, causing a decrease of thickness of the polymer film, the water vapor already induced the phase separation of the polymer film. Finally, the film was immersed into the non-solvent bath (water) at room temperature. The best results following this procedure ($t_{vapor\ bath}$ = 3 min, T_{vapor} = 30°C, $t_{H2O\ bath}$ = 3 min) were obtained with a polyethersulfone solution (9.8 wt% PES, 49 wt% NMP, 39.2 wt% acetone, 2 wt% Span 80) denoted here as standard PES solution. These microsieves had average pore diameters of 4.5 μm, a pore-to-pore distance of 10 μm, a surface porosity of 10 %, and a thickness of 10 μm.
To use these kinds of microsieves for emulsification purposes, the porosity has to be decreased to avoid coalescence and disturbances of adjacent growing drops. Therefore, we studied the fabrication of defect free polymeric microsieves with a lower porosity using a dedicated silicon mold. After successful fabrication, the emulsification behavior was tested.

6.2 Materials and Methods

Materials

As polymer base material for the polymeric nozzle plates, polyethersulfone (PES, Ultrason E6020P, BASF) was used. The polymer solvent was N-Methylpyrrolidone (NMP, Acros Organics) and the co-solvent was acetone (Merck). The surfactant Span80 was used to suppress macrovoid formation and to decrease the surface tension of the casting solution. Other used additives were the polyvinylpyrrolidones

(PVP) K90 and K30 (Fluka) and sulfonated polyether-ether-ketone (SPEEK, custom-made, sulfonation degree approx. 70 % [10]).

For emulsification experiments MilliQ-water containing 1 wt% Tween20 (polyoxyethylene (20) sorbitan monolaurate, Merck) was used as continuous phase and sunflower oil as dispersed phase.

The silicon mold had a structured area of about 7 cm^2 divided into 2500 fields. The field area was 0.5 x 0.5 mm and the fields were separated from each other by a deeper grid structure (see Fig. 2A). Each field contains 116 straight pillars of 4 μm in diameter and 15 μm in height. A single pillar is depicted in Figure 2B. Within a single field the pillars were arranged in four different patterns as shown in Figure 3. The larger distances between the pillars - compared to molds used by Vogelaar et al. [7,8] and Gironès et al. [9] – were chosen to avoid coalescence and interference of adjacent growing drops. The mold was prepared by photolithographic techniques and deep-reactive-ion-etching.

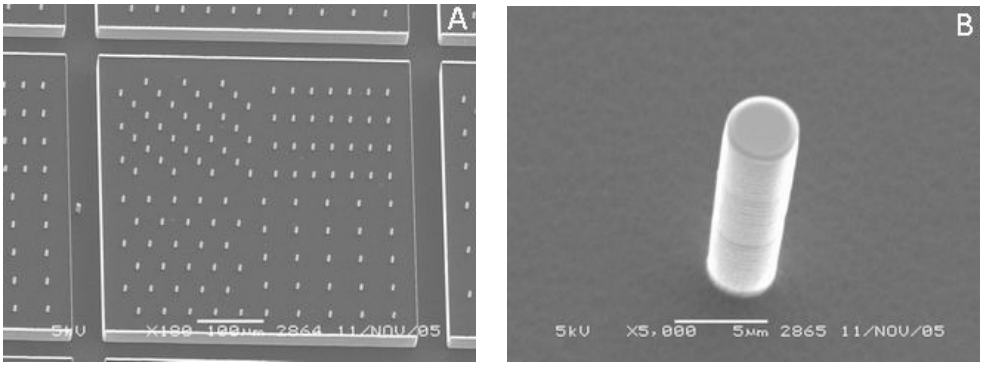

Figure 2: SEM-images of a pillar field surrounded by the deeper grid structure (A) and a single pillar (B) on the silicon mold. The images were made under a tilt angle of 30°.

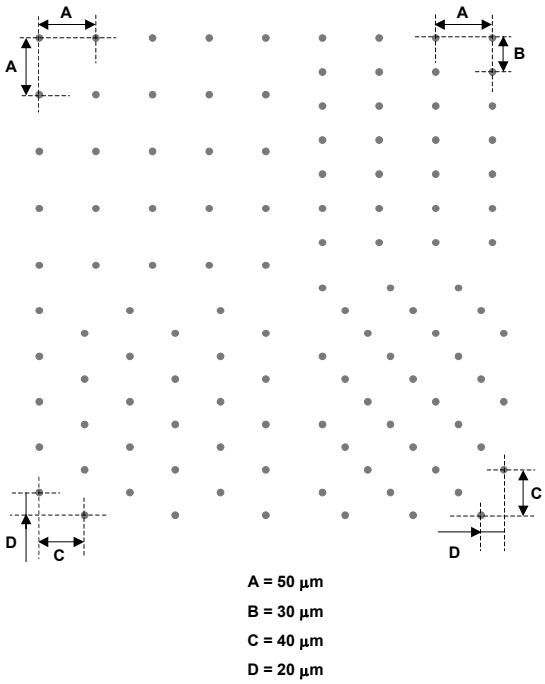

Figure 3: Pillar pattern within one field on the silicon mold. Each dot represents one pillar.

Phase separation micromolding

The mold was placed on a steel table provided with several millimeter-sized holes connected to a vacuum pump to fix the mold on its position. The casting thickness, which is the height between the casting knife and the mold, was adjusted with two micrometer screws ($h_{casting}$ = 25 –35 µm).

After casting, the mold was removed from the casting table and placed into a box flushed with nitrogen to evaporate the volatile co-solvent for 5 to 10 min. Depending on the used casting solutions, the mold was transferred into a water vapor bath for 5 min or for 5 min into a NMP/water (75/25 v/v) at room temperature. The water vapor temperature was varied between room temperature and 60°C. Finally the mold was immersed into a water bath for complete solvent exchange. Within the water bath the perforated films were carefully peeled from the mold and dried in air. The mold itself was cleaned afterwards in a NMP bath for approximately 30 min, then washed with fresh NMP and rinsed with iso-propanol.

The quality of the produced films was studied by light microscopy using an inverted microscope (Zeiss Axiovert). All pictures shown here are optical images unless otherwise noted.

Emulsification set-up

The emulsification set-up and procedures used here to observe the drop formation was the same as described before [3]. The procedures were also adapted to oil-in-water emulsification experiments. One essential point for oil-in-water experiments is that the continuous phase should be fed first into the system, resulting in a negative pressure difference and therefore permeation of water through the perforations of the polymer film. This ensures that the polymer film is fully wetted with the continuous phase.

The perforated films were glued with a two-component epoxy glue on metal sieve holders having a square shaped opening of 4 x 4 mm. Other glues (Cyan acrylate or silicon glue) were too liquid and wicked into the polymeric film resulting in a blockage of the perforations.

6.3 Results and Discussion

6.3.1 Fabrication of perforated polymer films

Pure PES films

The starting point of the fabrication of perforated polymer films was the standard PES recipe and the phase separation procedure reported by Gironès et al [9]. They obtained fully perforated and defect free polymer films. Applying this recipe and procedure on the mold used here, which has less pillars per field, leads to an enormous shrinkage of the polymer film around some of the imprints of the pillars. This phenomenon is show in Figure 4A. To check the reproducibility of the fabrication procedure according to Gironès et al., the same PES solution was cast over a microfiltration mold with 16 times more pillars per field. Following the

standard procedure a perforated and mostly defect free PES films was prepared as depicted in Figure 4B.

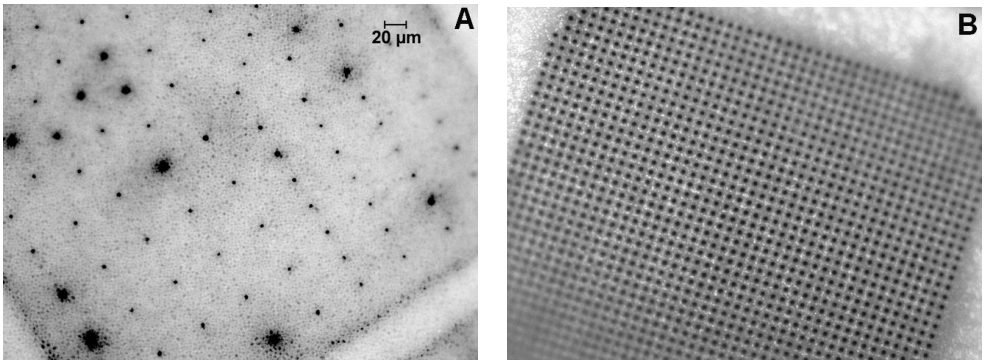

Figure 4: Phase separated PES films obtained from a mold with few pillars (A) and from a mold with 16 times more pillars per field (B). Both films were made from the standard PES solution and under the same conditions ($h_{casting}$ = 30 µm, t_{vapor} = 3.5 min, T_{vapor} = 30°C).

To reduce the shrinkage of the polymer film during the phase separation process, a polymer solution with a higher PES content was used (13.9 wt% PES, 46.3 wt% NMP, 37.4 wt% acetone, 1.9 wt% Span80). To increase the polymer concentration even more before phase separation the co-solvent acetone was partly evaporated in a box continuously flushed with nitrogen. The amount of defects could be decreased but not fully avoided as Figure 5A and B clearly illustrate. Figure 5A shows a film cast with a thickness of 25 µm and the one shown in Figure 5B with 20 µm under similar conditions. The latter one could not be peeled from the mold. In Figure 5B it can be seen that the defects are either located at the edges of the grid structure or around the pillars. The bright parts in the figure are representing the mold surface and the pillars, which punched through the film.

Higher PES concentrations in the casting solutions were not investigated since this increases the viscosity of the casting solutions, causing problems with entrapment of air bubbles in the grid structure.

As shown in Figure 4A, 5A and 5B, the origin of the defects is mostly the location of a pillar. But the observed defects are also found in polymer film outside the structure

area as it can be seen in Figure 6. Therefore, it is likely that these defects are related to macrovoids.

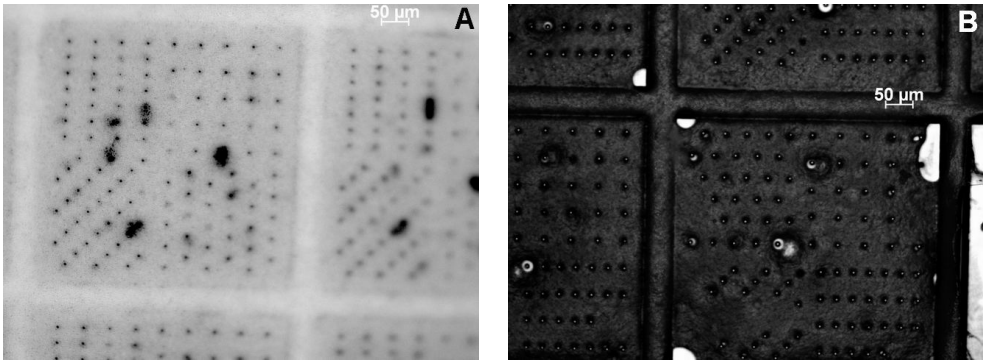

Figure 5: PES films obtained from a higher PES concentration (13.9 wt%) phase separated at equal conditions ($t_{nitrogen\ bath}$ = 5 min, $t_{water\ vapor}$ = 5 min, T_{vapor} = 30°C). Film cast with 25 µm thickness (A). Film cast with 20 µm thickness and not peeled from the mold (B).

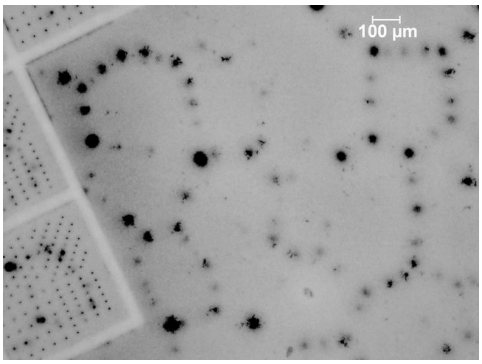

Figure 6: Network like structure of defects in a phase separated PES film (13.9 wt% PES, $h_{casting}$ = 20 µm, $t_{water\ vapor}$ = 5 min, T_{vapor} = 30°C)

To suppress the macrovoid formation without changing the composition of the casting solution an additive for the coagulation bath had to be chosen. This additive should delay the phase separation process. For the three phase system PES/NMP/water, Boom et al. studied the formation of membranes and the resulting structures with a coagulation bath containing different volume ratios of NMP and

water [11]. The delayed demixing occurred at a ratio of NMP to water of 3/1 associated with the disappearance of macrovoids. Beside the fact that this research was done on membranes prepared from casting solutions with higher PES contents and larger thickness, it was applied to phase separation micromolding. The PES recipe itself was not changed and the evaporation step of the co-solvent acetone was kept as well. Only the water vapor bath was replaced with a 75/25 vol% NMP/water bath. The final solvent exchange was still taking place in a water bath.

The appearance of the polymer film after immersing into the NMP/water bath was more opaque instead of white. The films turned totally white after immersing into the final water bath. PES films cast and phase separated using the NMP/water coagulation bath showed no macrovoids across the entire film. Figure 7A and 7B show two images of the resulting perforated PES films. It can be seen that these films are defect free. The pores are slightly deformed probably due to the shrinkage of the polymer. The average hydraulic diameter of the pores is 5.5 ± 0.5 μm.

The pore deformation becomes more pronounced in thinner cast PES films under otherwise equal conditions. The shrinkage of the film increased to an extent that the polymer film in the pillar fields separated from the grid structure. Consequently, the polymer film in the field could not be completely removed from the mold. Still, the remaining film allowed the quantification of the pore deformation. In Figure 8, the length and the direction of the deformations within a single field is plotted as vector graph. It clearly shows that the length of the pore deformation decreases from the outside towards the center and that the direction of the deformation is mostly pointing to the center of the field. A proved physical reason for this orientated deformation is not available. Further research on this phenomenon is required.

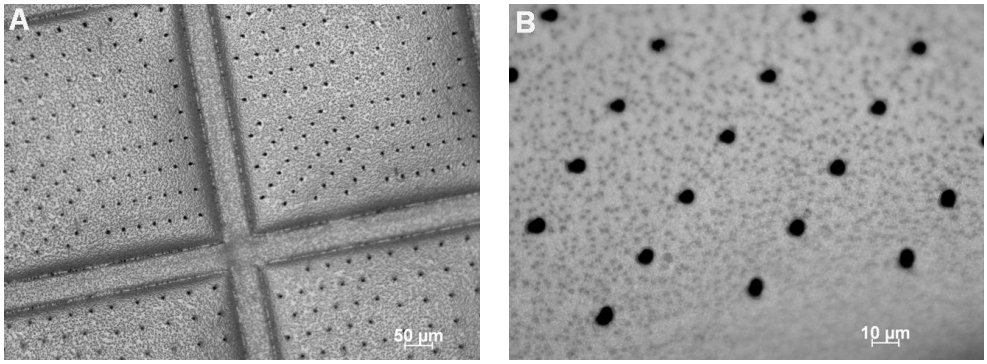

Figure 7: Perforated PES films obtained by immersing in a pre-coagulation bath of 3:1 NMP/water bath (13.9 wt% PES, $h_{casting}$ = 30 µm, $t_{nitrogen}$ = 10 min, $t_{NMP/water}$ = 5 min). Pore fields and grid structure (A). Close-up of the pores within a pore field (B).

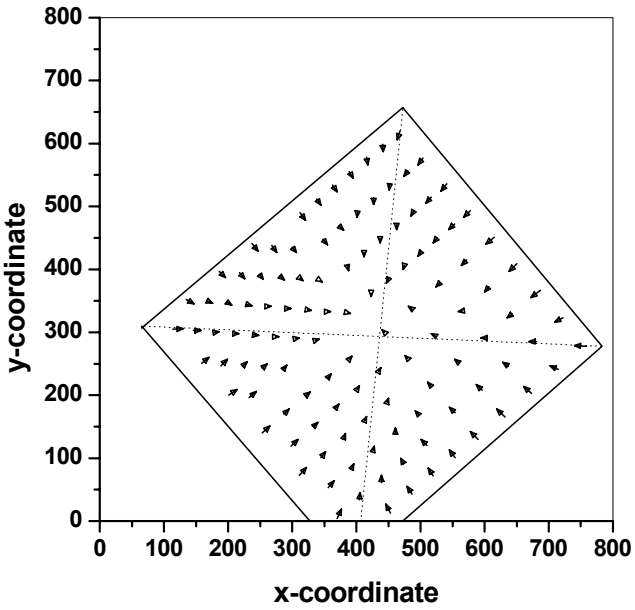

Figure 8: Vector graph of the pore deformation in a single pore field. The solid lines are representing the edge of the field and the crossing dash lines indicating the center of the field.

PES-PVP films

It was already reported from Gironès et al. that pure PES films are not really hydrophilic, having a water/air contact angle of about 60° [9]. In order to perform a successful oil-in-water emulsification, the used perforated polymer film should be more hydrophilic. The addition of PVP to the PES casting solution decreases the water/air contact angle as shown by Gironès et al. In Figure 9, PES/PVP films are shown cast with a thickness of 30 μm from a 9.6 wt% PES, 1.9 wt% PVP K90, 51.0 wt% NMP and 37.5 wt% acetone solution. The fabrication conditions were the same as used for the pure PES films (10 min N_2 bath, 5 min 75/25 NMP/water bath). It can be clearly seen that defects emerge at the edges of grid structure. This tearing was also reported by Gironès et al. for PES/PVP K90 (10 wt% / 7 wt%) films [9]. The pores in the PES/PVP are also deformed. From the pores next to the grid structure to the pores towards the center of the field, the deformation decreases and the pores are deformed always in the direction of the center.

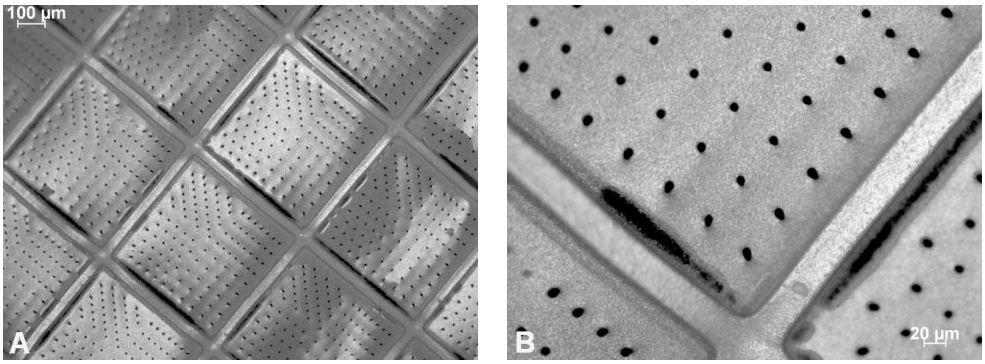

Figure 9: PES/PVP K90 films showing tearing at the edges of the grid structure (A) and deformation of the pores in direction of the pore field center (B).

To suppress the tearing, a mixture of PVP K90 and K30 could be used. Unfortunately, the addition of the PVP K30 increases the water/air contact angle, which is not desired here. The PVP K30 has only a molecular weight of 40 kDa and might be washed out in the water bath.

PES-SPEEK films

In order to increase the hydrophilicity of the perforated PES films, sulfonated poly-ether-ether-ketone (SPEEK) was chosen as an additive for the casting solution. SPEEK is a polyelectrolyte material having sulfonic acid groups located at the aromatic rings. In an aqueous environment this group is able to dissociate into a SO_3 anion and a proton resulting in a negatively charged polymer. Due to its electrical properties pure SPEEK or SPEEK blends are under investigation as ion exchange membranes and proton-conductive membranes for direct full cell applications [12-14]. To improve the hydrophilicity of relative hydrophobic polymers, SPEEK was used firstly by PCI Membranes [15]. The improvement of the hydrophilicity is associated with the SO_3H groups and the ability of SPEEK to adsorb water to a great extent. At a sulfonation degree of 80 percent SPEEK has a water uptake of 20-23 wt% [12]. Therefore, SPEEK seems to be an excellent additive to enhance the hydrophilicity of perforated PES films.

For the casting of perforated films a solution of 11.7 wt% PES, 2.3 wt% SPEEK, 49.2 wt% NMP and 36.8 wt% acetone was used. To achieve defect free films, the phase separation was performed in the water vapor bath instead of the NMP/water bath. The latter one caused tearing at the grid structure and pore deformation. With this recipe, well perforated, defect free and less deformed films were obtained as shown in Figure 10.

The addition of SPEEK seems to suppress the formation of macrovoids in PES films. This feature of SPEEK was also described for the fabrication of polysulfone membranes [16]. The pore size of 5 ± 0.3 μm within the PES/SPEEK film was only slightly smaller compared to the pore size obtained in pure PES films.

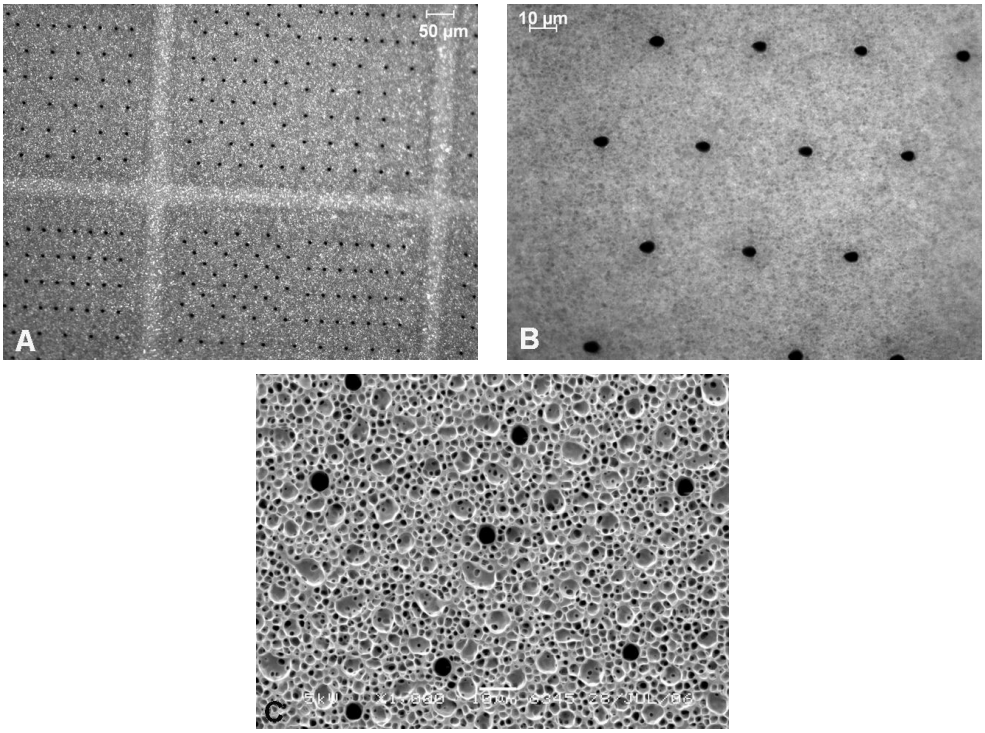

Figure 10: PES/SPEEK films ($h_{casting}$ = 30 µm, $t_{nitrogen\ bath}$ = 10 min, $t_{water\ vapor}$ = 5 min, $T_{water\ vapor}$ = 30°C) showing no tearing and macrovoids (A) and less deformed pores (B). SEM-Image of the air side of the PES/SPEEK film showing a spongy and open structure (C).

6.3.2 Emulsification experiments

Pure PES films

The emulsification experiments were conducted with perforated PES films produced by phase separation in a 3:1 NMP/water bath. The first sunflower oil drops appeared at approximately 54 mbar. Considering the average hydraulic diameter of the pores of 5.5 µm this critical pressure corresponds to an interfacial tension of 6.75 mN/m. This value for the interfacial tension of 1wt% Tween20 at the water/sunflower oil interface is close to the value of 6.5 mN/m for the same pair of liquids reported in literature [17].

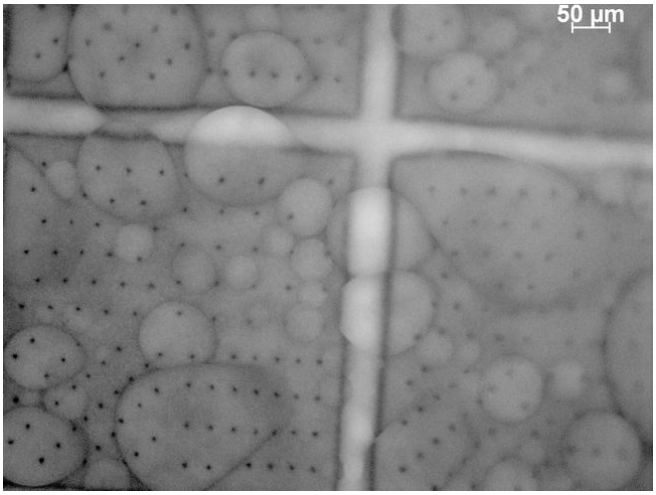

Figure 11: Emulsifying sunflower oil into water containing 1 wt% Tween20 with a pure PES film without any pre-treatment of the film.

The drop formation was not successful as it can be clearly seen in Figure 11. The sunflower oil wetted the surface of the film resulting in extensive coalescence. The PES film was not hydrophilic enough to ensure controlled oil drop formation. To overcome this negative performance, the surface properties of the PES film have to be changed into a more hydrophilic state. Therefore, the polymer film was pre-treated in an oxygen plasma etcher. This will create oxygen containing functional groups leading to a hydrophilic surface [18,19].

In Figure 12 the oil drop formation with an oxygen plasma treated PES film is shown. Compared to the untreated PES film, the drop formation was enhanced and drops of several hundreds of micrometer were formed and released. The hydrophilicity should be improved further to reduce the oil wetted area around the perforations in order to produce smaller drop sizes. The treatment time was only 2 minutes to avoid damages of the thin PES film. An optimization of the treatment time was not conducted and therefore left open for future research. Another approach to render the PES films more hydrophilic is to graft hydrophilic monomers onto the surface [20,21].

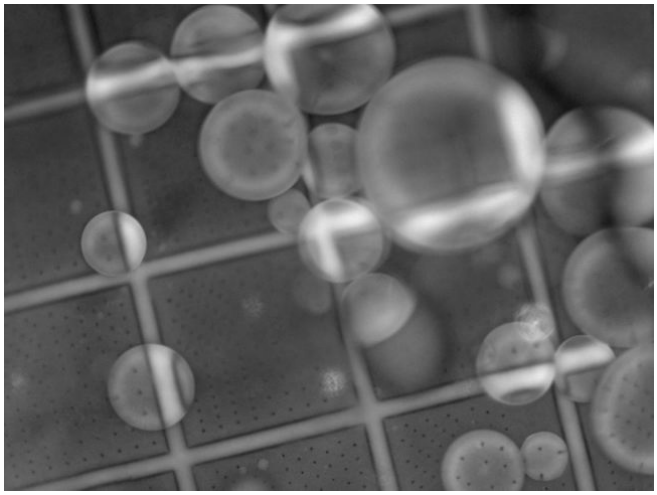

Figure 12: Emulsifying sunflower oil into water containing 1 wt% Tween20 with a plasma oxidized pure PES film ($t_{oxygen\ plasma}$ = 2 min).

PES/SPEEK films

To emulsify sunflower oil into water, PES/SPEEK films were used (same batch). The perforated film is shown in Figure 10. A first experiment was performed with a perforated film, which was immersed 3 hours in the aqueous continuous phase before starting the experiment to increase its hydrophilicity. But as Figure 13 clearly illustrates, the sunflower oil was spreading over the film surface.

At next the immersion time was greatly extended to 6 days. This pretreatment time had a huge influence on the drop formation. The sunflower oil formed drops, which detached from the film surface as depicted in Figure 14. The generated drops are relatively large indicating that the wetting properties are not optimal yet. Therefore, an oxygen plasma pre-treatment was performed instead of pre-soaking the film with the continuous phase before starting an experiment. Here, the treatment time was also 2 minutes. A longer exposure time causes visible damages.

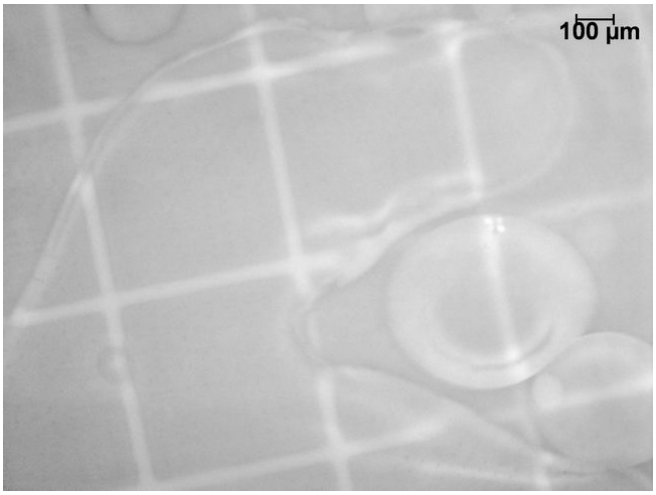

Figure 13: Emulsifying sunflower oil into water containing 1 wt% Tween20 with PES/SPEEK film. The film was immersed 3 hours before starting the experiment in the continuous phase.

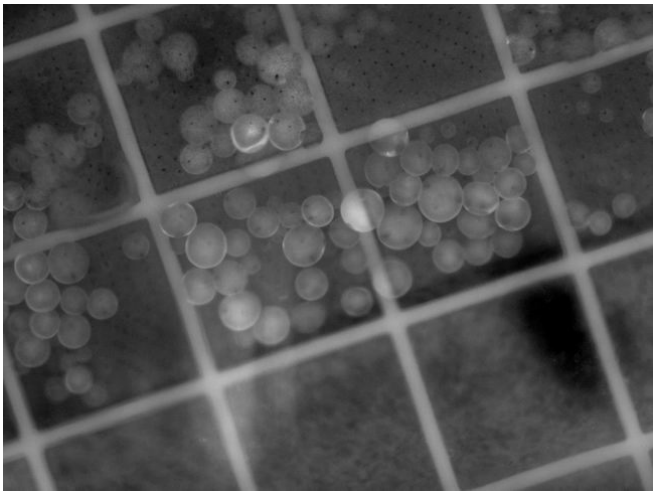

Figure 14: Emulsifying sunflower oil into water containing 1 wt% Tween20 with a perforated PES/SPEEK film, which was stored for 6 days inside the continuous phase.

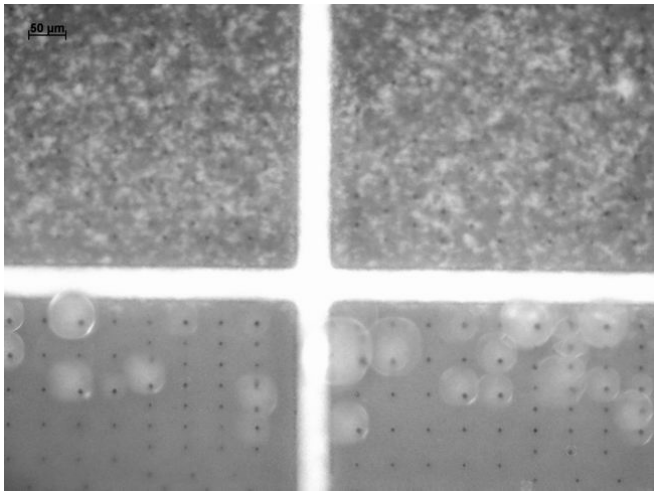

Figure 15: Sunflower oil emulsified into water containing 1 wt% Tween20 with a perforated PES/SPEEK film pre-treated for 2 min in an oxygen plasma. The film above the grid structure is glued on the sieve holder.

With the plasma treated PES/SPEEK film, sunflower oil could be successfully emulsified into the aqueous continuous phase. Figure 15 shows the generation of sunflower oil drops with a diameter of around 68 µm at the edge of the perforated film. There, first drops appeared at 52 mbar. The drop formation rate depicted in Figure 16 was determined from drops formed in the center of the entire film. Here, first drop formation was observed at 78 mbar. Considering that the equilibrium interfacial tension of 1 wt% Tween20 is 6.5 mN/m, the critical pressure of 78 mbar corresponds to a pore diameter of 3.3 µm assuming a spherical pore. Due to the deformation of the film towards the continuous phase under the action of the applied pressure difference, the pores can be deformed resulting in smaller hydraulic pore diameters. Thus, the pores in center of the entire film exhibit higher critical pressures. The number of active pores was also different. At the edges, as depicted in Figure 15, more pores per field were active compared to pore fields in the center. However, the drop formation rate showed, as reported earlier, a linear increase with increasing pressure difference [3,5]. The number of active pores was lower compared to silicon nitride and metal nozzle plates.

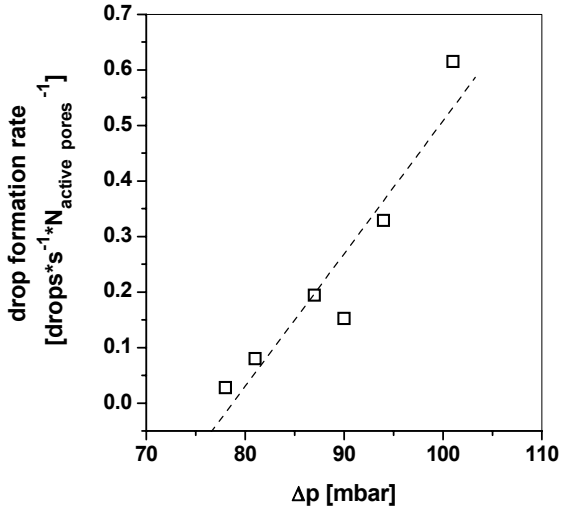

Figure 16: Drop formation rate versus applied pressure difference (Δp) for emulsifying sunflower oil into a 1 wt% aqueous Tween20 solution with a O_2 plasma treated PES/SPEEK film.

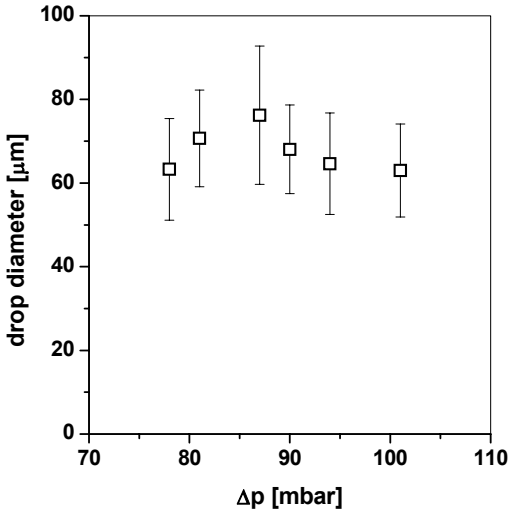

Figure 17: Average drop diameter versus applied pressure difference (Δp) obtained from emulsifying sunflower oil into water containing 1 wt% Tween20 with a perforated PES/SPEEK film.

The formed drops had a diameter of approximately 68 μm. The pressure influence on the drop size is shown in Figure 16. It indicates that the pressure has no significant influence on the drop size within the applied range of pressure differences. The coefficient of variation (COV) of the generated drops ranged from 16 to 22 percent, which lies in the reported interval of 5 to 40 percent for cross-flow membrane emulsification [22]. For silicon nitride micro-nozzle plates, the COV was increasing with increasing number of active pores resulting in a strong interference of drops growing next to each other [3]. Drops formed from a single pore had COV values below 10 %. Here, drops were mostly formed at pores far away from each other and the COV was not influenced by the pressure difference. The drop diameters from single pores had the same range of size variation. The drop sizes determined from the extracted movie frames were varying from 20 to 40 pixels and a single pixel represents 2.9 μm. Therefore, a measurement error of one pixel already results in a variation of the drop size of 5 %.

However, we could show the successful emulsification of sunflower oil into water with perforated and defect free polymer films. Future research on casting recipes based on more hydrophilic polymers or blends of PES with hydrophilic polymers is required. These polymers should possess low water/air contact angles (high surface energy) or high water swelling degrees combined with a low affinity to hydrophobic liquids. Possible candidates for these kinds of polymers are for instance cellulose acetate and other cellulose esters, which show low water/air contact angles. An interesting polymer blend found in literature is Polyacrylonitrile (PAN) /Poly acrylonitrile-r-3-sulfopropylacylate potassium salt (PAN-r-SAPS). This hydrophilic copolymer has an SO_3 terminated side chain and shows above 40 wt% a water/air contact angle of around 7° [23].

In principle, all polymers having polar functional groups like hydroxyl-, carboxyl- or sulfonic-groups are good candidates to increase the hydrophilicity of a polymeric film. These groups can be introduced by blending with hydrophilic co-polymers or additives, by surface grafting with hydrophilic monomers or by reactive gas plasmas.

6.4 Conclusion

Phase separation micromolding offers the ability to produce different kinds of micro perforated films from various polymers. We could show that changing the mold structure implies new recipes and adjustment of conditions. The standard PES recipe for the fabrication of microsieves for microfiltration was further developed to produce defect free low porosity films for membrane emulsification.
To generate oil-in-water emulsions a second limitation was faced – the wettability of the used polymers. The hydrophilicity of PES was not sufficient enough to ensure a controlled oil drop formation. The blending with the hydrophilic polymer SPEEK and the preconditioning by oxygen plasma increased the hydrophilicity to an extent that successful emulsification of sunflower oil into water could be performed.

6.5 Abbreviations

COV	Coefficient of variations
NMP	N-Methylpyrrolidone
PES	Polyethersulfone
PVP	Polyvinylpyrrolidone
SPEEK	sulfonated poly-ether-ether-ketone

6.6 References

[1] A.J. Abrahamse, R. van Lierop, R.G.M. van der Sman, A. van der Padt, R.M. Boom, J. of Membr. Sci. 204 (2002) 125-137

[2] S. van der Graaf, C.G.P.H. Schroën, R.G.M. van der Sman, R.M. Boom, J. Colloid Interface Sci. 277 (2004) 456-463

[3] M.J. Geerken, Chapter 4 of this thesis

[4] M. Kohno, Y. Matsuoka, JSME International Journal Series B 47 (2004) 497-500

[5] M.J. Geerken, Chapter 5 of this thesis

[6] M. Mulder, Basic principles of membrane technology, Kluwer Academic Publishers, Dordrecht/NL, 1996

[7] L. Vogelaar, J. N. Barsema, C. J. M. van Rijn, W. Nijdam, M. Wessling, Adv. Mater. 15 (2003) 1385-1389

[8] L. Vogelaar, R. G. H. Lammertink, J. N. Barsema, W. Nijdam, L. A. M. Bolhuis-Versteeg, C. J. M. van Rijn, M. Wessling, Small 1 (2005) 645-655

[9] M. Gironès, I.J. Akbarsyah, W. Nijdam, C.J.M. van Rijn, H.V. Jansen, R.G.H. Lammertink, M. Wesslin, J. Membr. Sci. (2006), doi: 10.1016/j.memsci.2006.07.016

[10] F.G. Wilhelm, I.G.M. Pünt, N.F.A. van der Vegt, H. Strathmann, M. Wessling, J. Membr. Sci. 199 (2002) 167-176

[11] R.M. Boom, Chapter 4, Ph.D Thesis, University of Twente, The Netherlands 1992

[12] P.X. Xing, G.P. Robertson, M.D. Guiver, S.D. Mikhailenko, K. Wang, S. Kaliaguine, J. of Membr. Sci. 229 (2004) 95-106

[13] C. Manea, M. Mulder, J. Membr. Sci. 206 (2002) 443-453

[14] J. Kerres, A. Ulrich, F. Meier, T. Häring, Solid State Ionics 125 (1999) 243-249

[15] M. Peer, UK patent application GB 2216134 A, 1989

[16] W.R. Bowen, T.A. Doneva, H. Yin, Desalination 145 (2002) 39-45

[17] P. Marie, J.M. Perrier-Cornet, P. Gervais, J. of Food Engineering 53 (2002) 43-51

[18] D. Tyszler, R.G. Zytner, A. Batsch, A. Brügger, S. Geissler, H. Zhou, D. Klee, T. Melin, Desalination 189 (2006) 199-219

[19] M. Ulbricht, G. Belfort, J. Membr. Sci. 111 (1996) 193-215

[20] M. Taniguchi, G. Belfort, J. Membr. Sci. 231(2004) 147-157

[21] D.S. Wavhal, E.R. Fisher, J. Membr. Sci. 209 (2002) 255-269

[22] G.T. Vladisavljevic, R.A. Williams, Adv. Colloids and Interface Sci. 113 (2005) 1-20

[23] B. Jung, J. Membr. Sci. 229 (2004) 129-136

Chapter 7

Porous Channel Emulsification

Abstract

This chapter describes the formation of droplets inside porous channels. Here, the continuous phase is introduced into the dispersed phase channel through a permeable porous polymer matrix. Inside the dispersed phase channel the continuous phase flow forces the dispersed phase to break-up into droplets. We will show the fabrication of channels with diameters of 160 μm embedded in a porous polymer membrane and the assembling into a microfluidic device. This device allowed us to observe the drop break-up process, which is similar to drop break-up in flow-focusing devices. We could prove the capability of this new technique to form monodispersed sunflower oil drops, which were 1.16 to 1.25 times larger than the channel diameter. The coefficients of variation were below 3 percent.

7.1 Introduction

In the last years, the formation of monodispersed drops with micro-engineered emulsification devices attracted more and more attention. Several authors showed designs, which provide the formation of monodisperse drops in micron-sized features.

One of the first methods was microchannel emulsification. Within this technique rectangular microchannels are etched into a silicon wall, which separates the dispersed phase from the continuous phase. Towards the continuous phase the microchannel ends in a terrace, where dispersed phase drops are inflated before they detach. Drops are formed according to the spontaneous drop formation mechanism. In most of the studies, oil-in-water emulsification was performed due to the more hydrophilic nature of silicon. Within these studies, oil drops of 2.6 to 4.6 times the hydraulic diameter of microchannels were produced with coefficients of variation from 1.4 to 13 percent [1-4].

Kobayashi and co-workers developed a second design using the spontaneous drop formation process. Here, rectangular microchannels were etched vertically through a silicon plate with a thickness of 100 to 200 μm. This design is called straight-through microchannels. The formed oil drops were 1.9 to 3.5 times larger than the hydraulic diameters of the used microchannels and the coefficients of variation were ranging between 1.4 and 10 percent [5-8].

Another approach to produce monodispersed drops are T-junctions. Two microchannels are forming a T-junction made in PMMA, glass or silicon via micro-engineering tools. The to be dispersed phase flows in a channel which ends right-angled at the continuous phase flow channel. The drop formation process is mostly driven by shear and interfacial tension forces. Depending on the flow rates of both phases, the drop diameter can be adjusted to be smaller or larger than the hydraulic diameter of the continuous phase channel. Reported coefficients of variation are in the range of 1 to 2 percent within the optimal process conditions [9,10].

Flow-focusing devices are also used to generate monodispersed drops. Within these devices the continuous and the to be dispersed phase are flowing coaxial through a small orifice. The to be dispersed phase is the inner phase and flows

more slowly than the outer continuous phase. The drop break-up can occur within the orifice or downstream out of the orifice depending on the total flow rates and the flow ratio of the inner to the outer phase. The drop formation occurs due to competition of viscous stresses induced by the flow field and capillary stresses due to the interfacial tension between the two phases [11]. Most studies were focused on the drop break-up process [12,13]. Monodispersed drops with COV below 3 percent were obtained and the drop diameter decreased with increasing flow velocity of the continuous phase [14,15].

A quite recent development is the production of monodispersed drops within a macroporous hollow fiber. In their study, Hoppe et al. showed the formation of 1-octanol drops in water inside a hydrophilic polyethersulfone microfiltration hollow fiber [16]. Here, the dispersed phase is fed into the core of hollow fiber, whereas the continuous phase permeates, driven by a pressure difference, from the outside into the hollow core of the fiber. One essential requirement is that the membrane material should be wetted by the continuous phase in order to form a fluid layer on the inner surface of the fiber. Over the length of fiber the water fraction increases and leads to a displacement of the inner dispersed phase until the inner phase ruptures into droplets. Over a wide range of flow rates they could show the generation of drops with diameters of 1.4 times the inner diameter of the hollow fiber (300 μm). Due to this, the reachable drop diameters are restricted to the available hollow fiber dimensions. Obtaining porous, liquid permeable hollow fibers with smaller inner diameters is difficult. Furthermore, it is rather difficult to visualize the drop formation inside a hollow fiber.

These two limitations were the motivation of the work presented here. We will show the fabrication of a microfluidic chip with round channels embedded in a porous polymer matrix, which are smaller in diameter compared to typical inner diameters of commercial available hollow fibers. This microfluidic chip should also allow the optical visualization of the drop break-up inside the channels. And finally the capability of the so-called porous channel emulsification (PCE) to generate monodispersed drops should be proved. The concept of the PCE in a microfluidic chip is schematically shown in Figure 1.

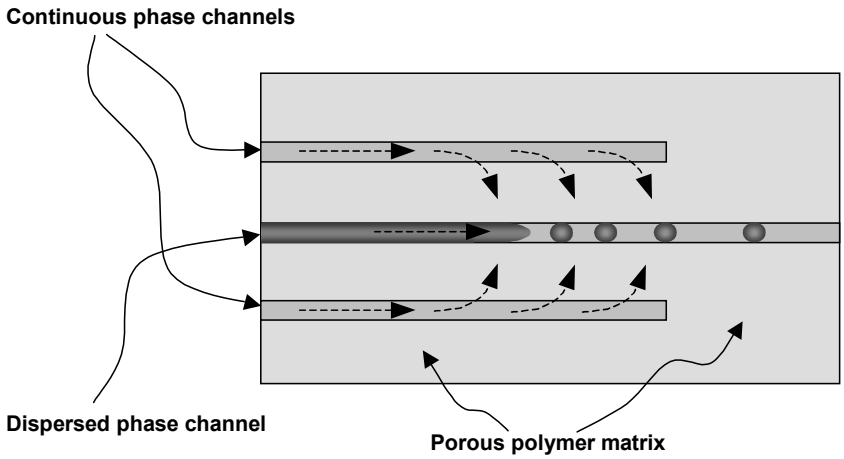

Figure 1: Schematic illustration of the porous channel emulsification in a microfludic chip.

7.2 Materials and Methods

Materials

For the membrane formation polyethersulfone (PES, Ultrason, BASF), polyetherimide (PEI, Ultem 1000), polyimide (PI, Lenzig) and polyvinylpyrrolidone (PVP, K90 360000 g/mol, Fluka) were used as polymers without further purification. In all cases N-methylprrolidone (NMP, Acros Organics) was used as solvent for the casting solutions. N-Hexadecane and sunflower oil were used as the dispersed phase and water containing the surfactant sodium dodecylsulfate (SDS) was used as continuous phase. For a better optical visualization, the water phase was coloured with Methylorange and the organic dispersed phase with Sudan Blue.

To feed the continuous and the dispersed phase into the microfluidic chip with controllable flow rates, two dual syringe pumps (Havard) were used, connected to the chip via 150 µm (internal diameter: 75 µm) fused-silica capillaries (Polymicro Technologies).

Phase separation micromolding

Phase separation micromolding is a recently developed method to structure polymeric materials [17]. In membrane fabrication a polymer solution is cast on a flat

glass plate and coagulated in a non-solvent bath afterwards. Further details about membrane formation via phase separation can be found in literature [18]. In phase separation micromolding the casting plate works as a template. For this purpose mostly a silicon wafer containing a microstructure produced in the cleanroom substitutes the glass plate. But also any other template, like shown in this work, can be used for structuring polymer sheets. With this technique, arbitrarily structured polymer films, even perforated ones can be formed. The wide range of polymeric materials, also with solid additives for later sintering, leads to manifold applications of the structured films, e.g. as scaffolds for tissue engineering, microsieves or in microfluidic systems [19].

The micromolding process starts with casting a polymer solution on a silicon wafer or other template mold and afterwards exposed to a non-solvent bath. The polymer film shrinks and solidifies during phase separation and therefore releases easily. After a cleaning step the mold can be reused for a new casting process.

Casting of flat sheet membranes

For the preparation of the flat sheet membranes steel roller casting knifes with a casting thickness of 0.2 mm to 0.4 mm were used. The casting was always performed on a glass plate at room temperature. The membrane coagulation was carried out at room temperature in a bath of tap water. Usually the membranes detached from the glass plate easily and were left in the water bath for at least one day while changing the tap water for several times to remove the solvent. Finally, all membranes were dried at room temperature between tissues. In the beginning an additional weight was placed on top of the tissues to prevent the membranes from rolling up and deforming. The obtained structure and the pore size were determined from SEM-Images.

Preparation of the capillary mold

To receive an easy microchannel structure of straight and parallel aligned channels, the polymer solution was cast on a template consisting of fused-silica capillaries glued on a glass plate with double sticky tape (Tesa®). This mold can be reused several times after cleaning with water. The outer diameter of the capillaries, which

are available from 90 µm diameter on, determines the later channel diameter. In this work 150 µm capillaries have been used.

7.3 Results and Discussion

Microfluidic Chip

First of all, a suitable recipe for the casting solution has to be identified. Therefore, we tested several polymer recipes to achieve an open and interconnected porous structure within the membrane and on the template side and a closed and dense surface on the air side. Table 1 shows some results obtained with polymer solutions based on PES, PEI and PI.

In all cases the glass side of the fabricated membranes was open. A general trend is that the pore size increases with decreasing polymer concentration, connected with the appearance of macrovoids as shown in Figure 2D. The use of a NMP/water-bath (60/40 v/v) instead of a water coagulation bath mostly suppressed the formation of macrovoids. The macrovoid formation is unwanted because the flow resistance in a macrovoid is lower than in the surrounding porous matrix. This would cause locally a higher continuous phase flow, which might be disturbing the drop formation process. Therefore, a homogeneous flow distribution is favored enabled by a regular porous structure.

The most suitable recipes for our purpose were the PEI recipes no. 6 and 7 and the PI recipes no. 10 and 11. As it can be seen in Figure 2A and 2B, the recipes 6 and 7 resulted in highly interconnected porous structures. This ensures a good permeability for the continuous phase over full length of the channels. The selected recipes were used to produce structured membranes for PCE experiments.

Table 1: Summary of the tested polymer recipes and resulting structures.

No.	Picture	Polymer/solvent	Mass percentages	Structure/comments	Pore size [μm]
1		PES/PVP/NMP	15/10/75	Open glass side, spongy, regular structure	0.5-1
2		PES/PVP/NMP	12/8/80	Spongy, highly interconnected pores, macrovoids, open glass side	3-8
3		PES/PVP/NMP	12/8/80	10 sec. NMP/water-bath, then pure water bath; round macrovoids, open glass side	3-7
4		PEI/PVP/NMP	19/11/70	Open glass side, spongy	0.5
5		PEI/PVP/NMP	19/11/70	10 sec. NMP/water-bath, then pure water bath; open glass side, graduently spongy to dense, interconnected pores	1
6	2A	PEI/PVP/NMP	15/10/75	Open glass side, spongy, interconnected pores	1-2
7	2B	PEI/PVP/NMP	15/10/75	10 sec. NMP/water-bath, then pure water bath; open glass side, spongy, interconnected pores	2-4
8		PEI/PVP/NMP	12/8/80	Open glass side, spongy, macrovoids on the bottom layer	3-8
9		PEI/PVP/NMP	12/8/80	10 sec. NMP/water-bath, then pure water bath; spongy, highly interconnected pores	5-10
10		PI/PVP/NMP	15/7/78	Open glass side, spongy, very regular	0.5
11	2C	PI/PVP/NMP	15/7/78	15 sec. NMP/water-bath, then pure water bath, open glass side, spongy	0.5-2
12		PI/PVP/NMP	12/8/80	Open glass side, spongy	0.5-1
13	2D	PI/PVP/NMP	10/5/85	Regular straight macrovoids, open glass side	2-10
14		PI/PVP/NMP	10/5/85	10 sec. NMP/water-bath, then pure water bath, spongy, few macrovoids, open glass side	3-8

One requirement for successful porous channel emulsification is that the continuous phase is the wetting phase. Therefore, contact angles of water containing SDS were

measured on the membranes while surrounded by the oil phase. For water/SDS the contact angle on a PEI membrane decreases from 105° measured after 1 minute to 80° after 20 minutes. In time the water phase becomes the wetting phase. Therefore, it is essential to flush the chip before starting an emulsification experiment with the continuous water phase to ensure complete wetting of the membrane material with water.

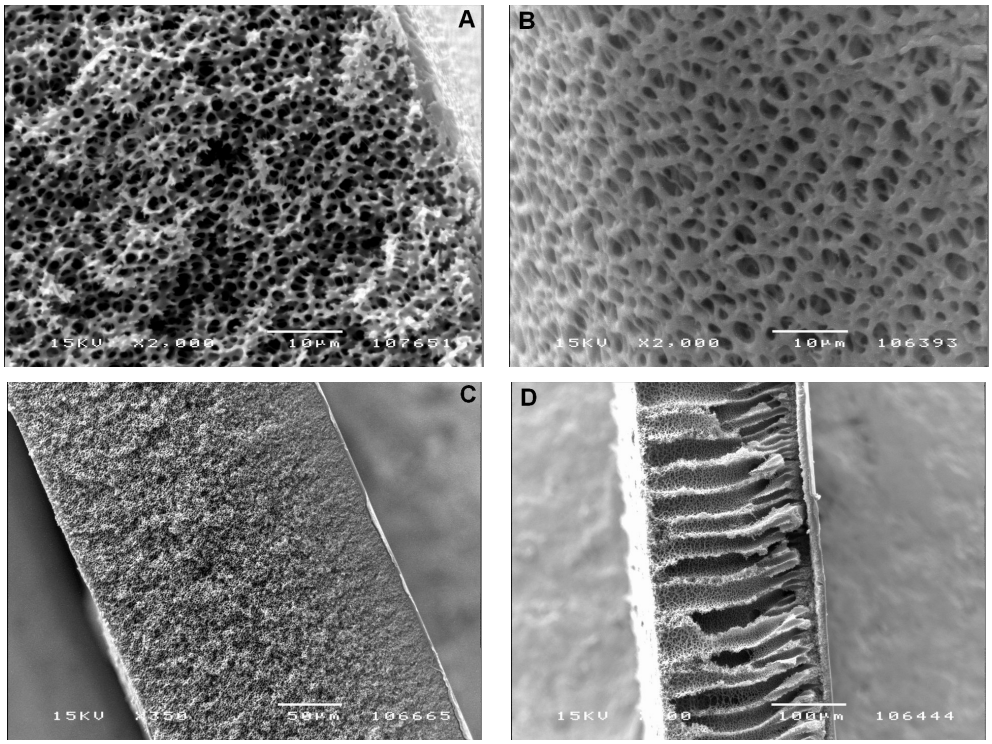

Figure2: SEM cross-section images of flat sheet membranes obtained from PEI recipes no. 6 (A) and 7 (B) showing highly interconnected pore structures and from PI recipe no. 11 (C). Image D displays the obtained macrovoid structure from the PI recipe no. 13.

To obtain a structure of parallel channels in a porous matrix the chosen polymer solutions were cast on the capillary mold and immersed into the coagulation bath as depicted in Figure 3.

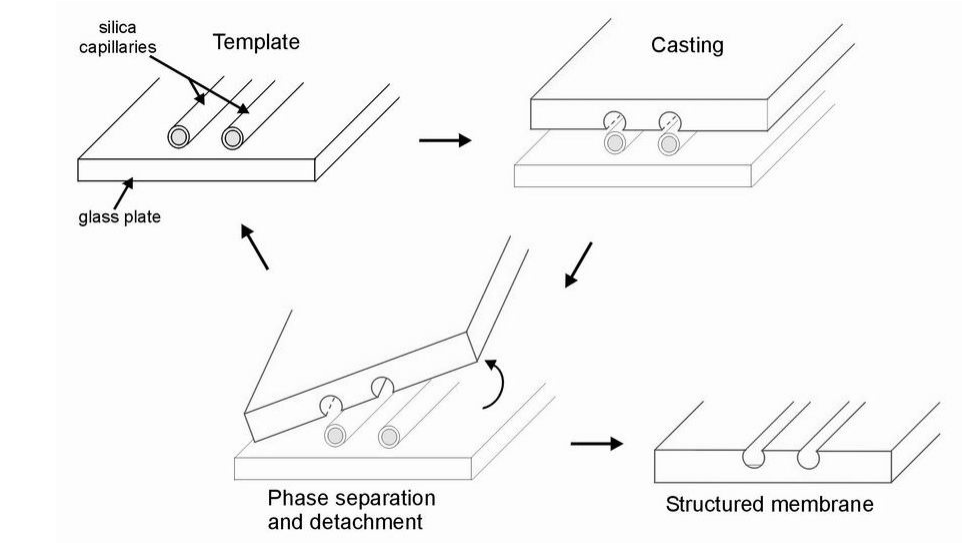

Figure 3: Phase separation mircomolding on a capillary mold.

To ease casting and avoid bubble inclusions, PEI and PI polymer solutions were heated up to 50°C before casting, while mold and casting knife were used at room temperature. The heating procedure lowers the viscosity of the solution, improving the casting. A significant change in pore size due to heating was not observed.

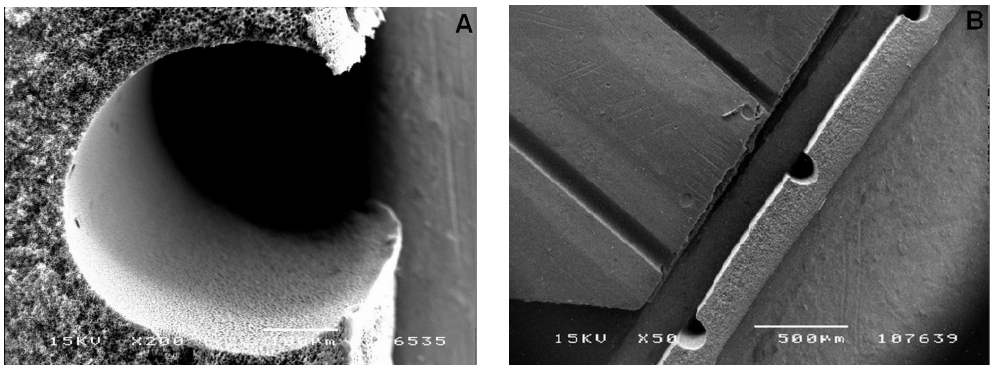

Figure 4: SEM-Images of the channels replicated from glass capillaries in the porous polyetherimide matrix. Cross-section of a single channel (A). Top-view and cross-section of three-channel microfluidic chip (B).

For materials like PEI and PI the shrinkage during phase separation and drying is rather low. The channel diameter (see Figure 4) was approximately 5 to 10 percent larger than the capillary diameter. This low shrinkage is later on important for the connection of the microfluidic chip to syringes, where the same types of capillaries were used.

This procedure resulted in round microchannels with porous walls embedded in a matrix of porous polymer. Channels obtained from 150 μm capillaries had a diameter of 160 μm. The channel diameter could be reduced even more by using smaller capillaries. Such circular channels cannot be produced by any cleanroom technology. Despite of the just simple geometry of straight channels the main advantage is the low material and time effort. Furthermore, the diameter, length and distance between the channels can be varied easily.

After the fabrication of the structured membrane itself, the channel structure has to be sealed. The sealing material itself should be resistant against the used liquids, should not block the pores and should allow optical observation. Several sealing procedures were applied (double sided adhesive tape, PDMS, PMMA) but the best and easiest method was to use commercial lamination sheets. A lamination sheet consists of thin and transparent polymer foil coated on one side with a melting adhesion layer. By applying heat and pressure the adhesive melts and joins the structured membrane layer with the foil. This works well for relatively large channels but for very small channels, blockage of the channel by the molten adhesive can occur [20].

For assembling the microfluidic chip, first the supply capillaries were placed into the channel ends. Chips with two and with three inlet capillaries were fabricated. Then the structured membrane, including the capillaries, was placed in between two pieces of the lamination sheet. For the drop break-up visualization experiments the exit of the dispersed phase channel was connected to a capillary as well. The exits of the continuous phase channels were blocked by the lamination sheet. To determine the resulting drop size, the dispersed phase channel was ending in a small reservoir on the chip. The lamination itself was conducted at 100°C on a hot plate while rolling with a steel bar over it.

Drop break-up

To identify the break-up process the drop formation was observed with a high-speed camera. Here, a two-channel chip was used. From the upper dead-end channel, water containing 0.5 wt% SDS was supplied. The hexadecane was pumped into the lower channel. The flow rates were 2 μl/min for the aqueous phase and 1 μl/min for the hexadecane phase, respectively.

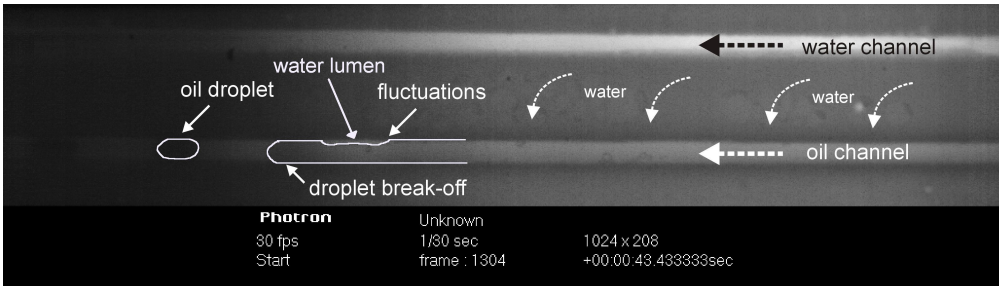

Figure 5: Drop break-up in the oil channel within a two-channel microfluidic chip. For clarification the oil-water interface is highlighted in white.

Figure 5 shows a snapshot of the drop formation. It can be seen that the permeating water forms a lumen between the channel walls and the oil phase. This lumen grows further resulting in narrowing and elongation of the oil lumen until this oil neck ruptures and an oil drop is formed. After the drop break-up the process starts again. Whether or not a thin layer of water surrounds the oil drop could not be identified. The drops formed within the experiments had approximately a diameter of 200 μm and with a formation rate of approximately 400 drops/min. The formation of satellite drops was not observed. Figure 6 shows a schematic representation of the observed drop break-up process for a three-channel chip.

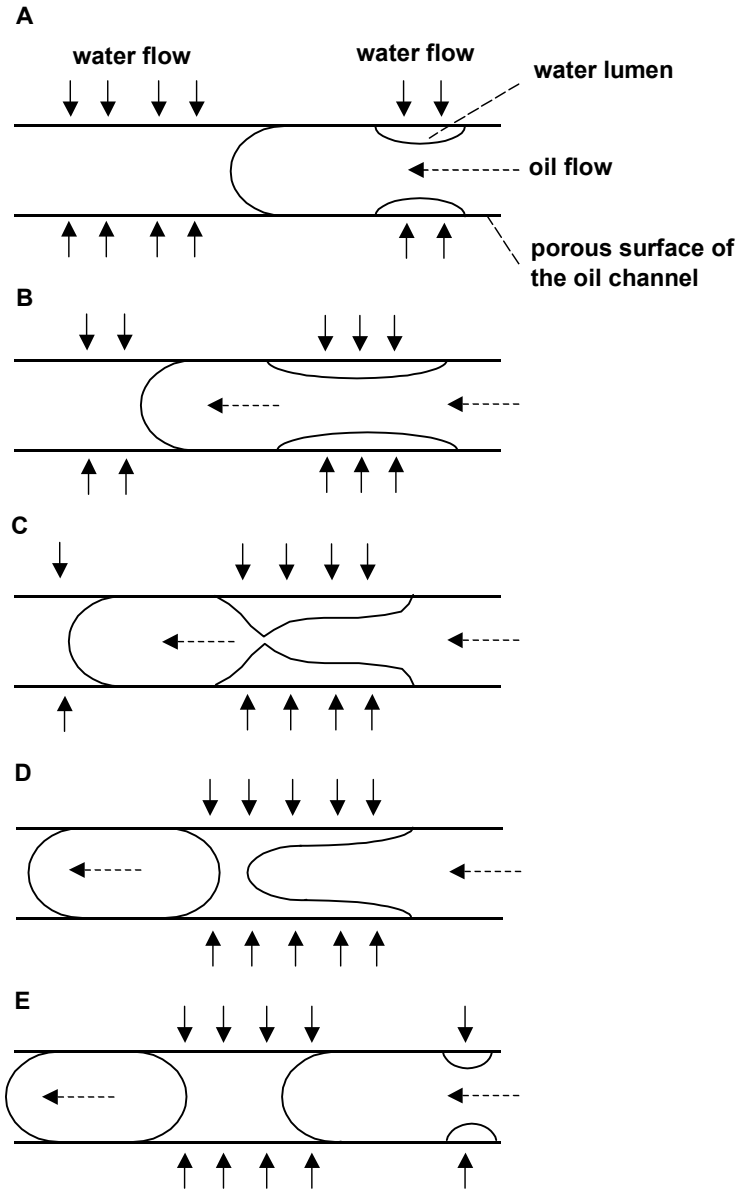

Figure 6: Schematic drawing of the observed drop formation process. Growing water lumen (A); lumen volume increases and oil neck is formed; oil neck ruptures and an oil drop is formed (C); oil neck recedes and new water lumen is formed (D-E).

The drop break-up process can be described as follows. A water lumen is formed due to the permeation of water from the water supply channel towards the oil channel through the porous membrane (Fig. 6A). The water lumen grows in time and displaces the oil phase from the channel surface forming a neck. (Fig. 6B). This part of the drop formation process can be seen as well in Figure 4. This process holds on until the neck diameter is reduced so far that it becomes unstable and ruptures (Fig. 6C). During this growth period the drop interface moves downstream with a constant velocity. After the drop break-up the remaining oil neck recedes to minimize its interfacial area and new water lumen is formed (Fig. 6D-E). The thinning of the neck at more than one horizontal position along the neck caused by capillary wave instabilities was not observed. Probably, the neck length did not exceed the Rayleigh-Plateau length.

Flow-focusing experiments performed by Anna et al. [12] and simulations based on these experiments conducted by Davidson et al. showed [13], that drops larger than the constriction are formed at a flow ratio of the inner to the outer phase of 0.25 and at a Reynolds number (Re) of 0.45. These parameters are in same order of magnitude as used in our work (Flow ratio 0.5, Re = 0.23). Davidson et al. described the drop break-up mechanism at low flow rates in a similar way compared to the observation reported in the present study. This drop formation process in two immiscible co-flowing liquids is called dripping and is characterized by a short thinning neck, which connects the forming drop with the bulk liquid. At higher velocities of the continuous phase and smaller flow ratios the dripping mode changes into the jetting mode [21,22]. Within the jetting regime the formed neck is far more elongated compared to dripping and multiple necking due to capillary wave instability can occur. In literature the transition from the dripping to the jetting regime is correlated to the Weber number. Depending on the viscosity ratio of the dispersed phase (the jet forming phase) and the continuous phase the Weber number of transition varies between 0.5 and 2. These values were obtained from numerical simulations for a liquid injected in a static continuous phase and the injection nozzle was located far enough from the side walls to neglect any influence of the walls [23]. In flow-focusing devices, effects caused by the channel walls might be not neglectable. However, the Weber numbers in our experiments were extremely small

(10^{-5}–10^{-3}) suggesting drop formation within the dripping regime. In the work of Hoppe et al. the Weber numbers were in a range of 1 to 15, which is probably already in the jetting mode as stated by them [16].

Drop size

From the drop break-up visualization experiments, it could already be concluded that relatively monodispersed drops with a diameter of around 200 μm were formed. To confirm this, drop formation experiments with a three-channel chip ($d_{channel}$ = 160 μm) using 1 wt% aqueous SDS solution as continuous phase and sunflower oil as the disperse phase were conducted. For observation and determination of the drop size the formed drops were collected in a small round reservoir.

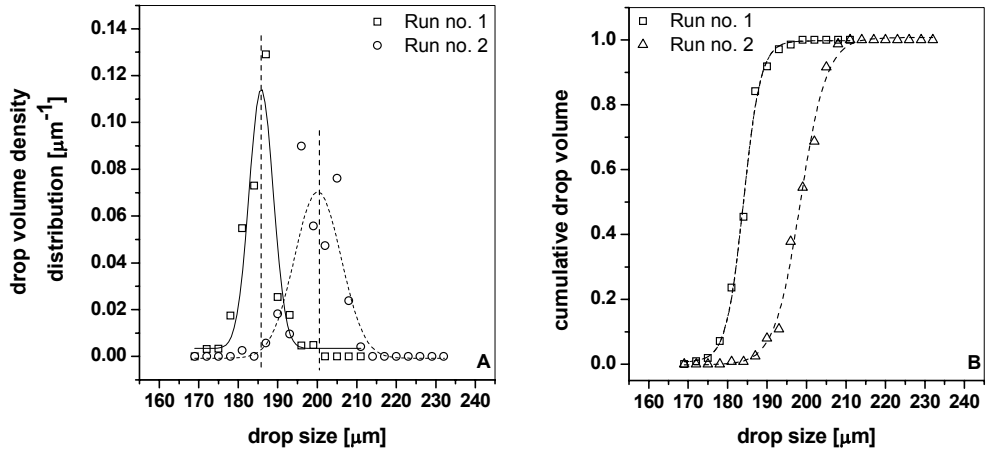

Figure 7: Resulting drop size distribution (A) and cumulative drop volume (B) of the formed sunflower oil drops.

The obtained drops showed a quite narrow size distribution (see Figure 7 and 8) with a span of 0.05 and 0.06 and a coefficient of variation of around 2.5 percent (see Table 2). The average drop sizes were 185 and 200 μm. Therefore, the ratio of the drop size to the channel diameter varied from 1.16 to 1.25. Here, the influence of different flow rates and flow ratios was not investigated. Hoppe et al. found a drop/channel size ratio varying from 1 to 2 for the system 1-octanol-in-water

emulsified within a hydrophilic PES hollow fiber depending on the flow ratio and the flow velocity of the continuous water phase [16].

Table 2: Average drop size, coefficient of variation and span of the drop size distribution of the formed sunflower oil drops.

Run	Average drop size [μm]	COV [%]	Span [-]
No. 1	185.4	2.3	0.054
No. 2	199.2	2.7	0.06

The drops in both runs were obtained at the same process conditions. It is know, that the drop size in flow-focusing devices increases with decreasing flow rate of the continuous phase [24,14]. Hoppe et al. reported this relationship as well [16]. Therefore, it is assumed that the formation of larger drops in the second run was caused by a lower water flow. A decline of the water flow might caused by a sealing failure or wetting problems.

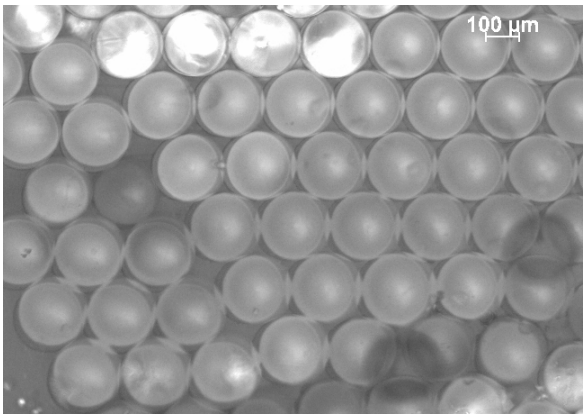

Figure 8: Optical image of the generated sunflower oil drops.

Air bubbles in the dispersed phase channel were always observed. It seems to be rather difficult to displace the air completely from the porous matrix and from the dead-end continuous phase channels. As long as the air bubbles were removed by

the liquid flow only small disturbances of the drop formation process were observed. Unfortunately, the air bubbles tended to stick to the channel surface resulting in a second break-up of the already formed drops into smaller drops. Most of the time, these drops were as well quite monodispersed. According to Link et al. this drop formation process by a flow restriction is called obstruction mediated passive break-up [25]. In fact, this effect can be used to make small droplets if the air bubble size and position can be controlled.

7.4 Conclusions

Here, we could successfully demonstrate the fabrication of a porous microfluidic chip allowing the visual observation of the drop break-up process. The chip was fabricated via phase separation micromolding using a custom-made capillary mold. The resulting chip contained round channels embedded in a porous polymer matrix. The porous matrix itself can be formed out of various polymers as long as a solvent/non-solvent pair is available to perform the phase separation process. In principle, all polymers and recipes for the fabrication of phase separated microfiltration membranes having a regular spongy structure can be applied for this technique. By choosing either a hydrophilic or a hydrophobic polymer oil-in-water and water-in-oil emulsions can be produced with the porous channel emulsification technique.

The observed drop formation within the channel is similar to the drop dripping process found in flow-focusing devices. The produced sunflower oil drops were up to 25 percent larger in diameter compared to the channel diameter of 160 μm and showed a monodispersed size distribution. Hence, we could prove the capability of the porous channel emulsification process to generate monodispersed drops. Most difficulties arise from entrapped air in the channels and within the porous polymer matrix. Further investigations on the air displacement are required.

7.5 Acknowledgements

Christina Schmidt-Leineweber and Nienke Ruepert are acknowledge for their huge effort and enthusiasm to get the microfluidc chips working.

7.6 Abbreviations

COV	Coefficient of variations
NMP	N-Methylpyrrolidone
PCE	Porous channel emulsification
PEI	Polyetherimide
PES	Polyethersulfone
PI	Polyimide
PMMA	Polymethmethylacrylate
PVP	Polyvinylpyrrolidone
SDS	Sodium dodecylsulfate

7.7 References

[1] S. Sugiura, M. Nakajima, J. Tong, H. Nabetani, M. Seki, J. Colloid Interface Sci. 227 (2000) 95-103

[2] T. Kawakatsu, G. Trägårdh, C. Trägårdh, J. of Food Engineering 50 (2001) 247-254

[3] S. Sugiura, M. Nakajima, S. Iwamoto, M. Seki, Langmuir 17 (2001) 5562-5566

[4] J. Tong, M. Nakajima, H. Nabetani, Eur. J. Lipid Sci. Technol. 104 (2002) 216-221

[5] I. Kobayashi, M. Nakajima, K. Chun, Y. Kikuchi, H. Fuijata, AIChE Journal 48 (2002) 1639-1644

[6] I. Kobayashi, M. Nakajima, Eur. J. Lipid Sci. Technol. 104 (2002) 720-727

[7] I. Kobayashi, S. Mukataka, M. Nakajima, Ind. Eng. Chem. Res. 44 (2005) 5852-5856

[8] I. Kobayashi, S. Mukataka, M. Nakajima, Lamgmuir 21 (2005) 5722-5730

[9] T. Nisisako, T. Torii, T. Higuchi, Chemical Engineering Journal 101 (2004) 23-29

[10] T. Nisisako, T. Torii, T. Higuchi, SICE 2002, Aug. 5-7, 2002, Osaka

[11] V. Cristini, Y.C. Tan, Lab Chip 4 (2004) 257-264

[12] S.L. Anna, N. Bontoux, H.A. Stone, Applied Physics Letters 82 No. 3 (2003) 364-366

[13] M.R. Davidson, D.J.E. Harvie, J.J. Cooper-White, ANZIM J. 46 (E) (2005) C47-C58

[14] S. Takeuchi, R. Garstecki, B. Weibel, G.M. Whitesides, Adv. Mater. 17 No. 8 (2005) 1067-1072

[15] S. Xu, Z. Nie, M. Seo, P. Lewis, E. Kumacheva, H.A. Stone, P. Garstecki, D.B. Weibel, I. Gitlin, G.M. Whitesides, Angew. Chem. Int. Ed. 44 (2005) 724-728

[16] J. Hoppe, T. Melin, in Abstract Book of the 10th Aachen Membrane Colloquium, 2005

[17] L. Vogelaar, J. N. Barsema, C. J. M. van Rijn, W. Nijdam, M. Wessling, Adv. Mater. 15 (2003) 1385-1389

[18] M. Mulder, Basic principles of membrane technology, Kluwer Academic Publishers, Dordrecht/NL, 1996

[19] L. Vogelaar, R. G. H. Lammertink, J. N. Barsema, W. Nijdam, L. A. M. Bolhuis-Versteeg, C. J. M. van Rijn, M. Wessling, Small 1 (2005) 645-655

[20] H. Becker, C. Gärtner, Electrophoresis 21 (2000) 12-16

[21] A.S. Utada, E. Lorenceau, D.R. Link, P.D. Kaplan, H.A. Stone, D.A. Weitz, Science 308 (2005) 537-541

[22] C. Cramer, P. Fischer, E.J. Winhab, Chemical Engineering Science 59 (2004) 3045-3058

[23] S. Homma, J. Koga, S. Matsumoto, M. Song, G. Tryggvason, Chemical Engineering Science 61 (2006) 3986-3996

[24] Y.C. Tan, V, Cristini, A.P. Lee, Sensors and Actuators B 114 (2006), 350-356

[25] D.R. Link, S.L. Anna, D.A. Weitz, H.A. Stone, Physical Review Letters 92 (2004) 1-3

Chapter 8

Summary and Outlook

8.1 Introduction

This thesis deals with the generation of emulsions with micro-engineered devices and relevant aspects like surface modification, wetting properties and fabrication of emulsification devices. In this section the main findings and conclusions are summarized and an outlook on further research is presented.

8.2 Summary

Silicon nitride micro-nozzles plates can be used for oil-in-water emulsification without any surface modification because of the hydrophilic nature of the clean silicon surface. For the creation of water-in-oil emulsions the surface has to be rendered hydrophobic to prevent the spreading of the aqueous dispersed phase across the surface. Therefore, different hydrophobization strategies were investigated in **Chapter 2**. The degree of hydrophobicity determined by water/air contact angle measurements and the thermal and chemical stability of self-assembling monolayers of alkytrichlorosilanes, plasma polymerized PDMS and dip-coated PDMS were investigated. The most hydrophobic and most stable under acidic and alkaline conditions was a monolayer of perfluorinated octyltrichlorosilane (FOTS). Other researched coatings exhibited sufficiently high water/air contact angles, but they possessed less thermal and chemical stability compared to FOTS.

The study of the wetting behavior of all tested coatings is discussed in **Chapter 3**. It was found that the highest water/oil contact angles were obtained when the used continuous phase (hexadecane) has a high affinity to the substrate. This could be

clearly shown for the octyltrichlorosilane (OTS) and for one type of the plasma polymerized PDMS, which both displayed higher water contact angles in hexadecane compared to FOTS. This could be explained by the solid surface energies and the interfacial tensions between the coatings and both liquids.
The measured water contact angles in hexadecane on several coatings showed significant differences compared to the calculated values according to Youngs equation. This was explained with a stable thin film of hexadecane between the water drops and the solid surfaces indicated by negative Hamaker constants for these systems. A positive constant was obtained for PTFE, suggesting a stable PTFE/water interface, resulting in a correct prediction by Youngs equation.
On the low surface energy coating FOTS we found a dramatic change in the wetting behavior when the continuous oil phase contained a protein containing emulsifier. Here, water drops suddenly wetted the former hydrophobic surface after some minutes. We attribute this to the ability of proteins to unfold and present their hydrophilic parts towards the water. During water-in-oil emulsification the drop formation process takes place in milliseconds. Therefore, the sudden drop spreading on FOTS was not observed in emulsification experiments.
In general, slow adsorbing emulsifiers will not significantly affect the continuous/dispersed and dispersed/solid interfaces as long as its adsorption rate is rather slow compared to the drop formation time.

In **Chapter 4,** the emulsification performance of hydrophobized silicon nitride micro-nozzle plates was studied. We demonstrated successfully the emulsification of water into n-hexadecane with OTS and FOTS coated nozzle plates via the shear-induced drop formation mechanism. Significant differences between FOTS and OTS coatings were found for the drop diameter caused by different contact angles for the water/n-hexadecane+surfactant/substrate systems. The different hydrophobic coatings did not significantly influence the drop formation rate, the percentage of active pores, and the lag time. At less than two times the critical pressure the number of active pores varied between 60 and 90 percent coupled with dispersed phase fluxes up to 4600 L h^{-1} m^{-2} bar^{-1}. The observed lag time is related to the slow adsorption kinetics of the used emulsifiers and decreased with increasing pressure

differences until it vanished at a certain Δp. For fast adsorbing emulsifiers like SDS a lag time is not reported.

An alternative to cleanroom-fabricated nozzle plates is discussed in **Chapter 5**. Laser drilled nozzles in metal foils with diameters down to 4.4 μm were used for oil-in-water and water-in-oil emulsification. Within these experiments, drop formation according to the shear-induced and spontaneous mechanism was observed. This observation is addressed to the less defined nozzle geometry compared to cleanroom-fabricated nozzles. The nozzle diameters were also wider distributed compared to silicon nitride nozzles. The obtained COV of the generated drops are comparable to drops formed with the silicon nitride nozzle plates. Therefore, laser-drilled metal nozzle plates are an alternative for silicon nitride microsieves, conventional microporous glass, and ceramic membranes and can be used for water-in-oil and oil-in-water membrane emulsification. Compared to microchannel and straight-through microchannel emulsification, the laser-drilled metal sieves are less defined to ensure only spontaneous drop formation. But there is still the opportunity to fabricate metal sieves having slits instead of circular holes.
Within emulsifying water into oil using Span85 as surfactant and dispersing oil into water using Tween20 as emulsifier the appearance of a lag time at low applied pressure difference was observed. In both cases it showed, as reported in Chapter 4, a linear relationship between the applied pressure difference and the negative square root of the lag time.

The use and production of perforated polymer films formed by phase separation micromolding is demonstrated in **Chapter 6**. Phase separation micromolding offers the ability to produce micro perforated films from various polymers. We could show that changing the mold structure implies recipe optimization and adjustment of conditions. The standard PES recipe for the fabrication of microsieves for microfiltration was further developed to produce defect free, low porosity films for membrane emulsification.
The wettability of the used polymers was another point of attention. Unmodified PES was not hydrophilic enough to ensure stable drop formation. Hence, the

hydrophilicity had to be improved by blending PES with SPEEK and by oxygen plasma treatment. Finally, we could demonstrate successful emulsification of sunflower oil into water.

In **Chapter 7** the development of a new emulsification device is shown. This new device is a porous microfluidic channel chip made via phase separation micromolding. It exhibits a simple channel geometry embedded in a porous polymer matrix and enables the optical observation of the drop formation process. The porous matrix itself can be made from various polymers as long as a solvent/non-solvent pair is available to perform the phase separation process.
The observed drop formation within the channel is similar to the drop dripping process found in flow-focusing devices. The produced sunflower oil drops were up to 25 percent larger in diameter compared to the channel diameter of 160 μm and showed a monodispersed size distribution. Hence, we could prove the capability of the porous channel emulsification process to generate monodispersed drops. Most difficulties arise from entrapped air in the channels and within the porous polymer matrix. Further investigations on the air displacement are required.

8.3 Outlook and future applications

Micro-engineering is a helpful tool to create nozzle plates with defined structures and geometries. For their use in membrane emulsification, it was found that exactly defined nozzle diameters are not so important. Despite equal nozzle sizes the resulting drop sizes have in most cases a certain distribution, as we could show in case of the silicon nitride nozzle plates. The shear induced drop formation process at multiple nozzles will result in a certain distribution because of limitations in generating a highly uniform and undisturbed flow field at each nozzle.
A more important feature of micro-engineering tools is the ability to adjust the distance between the nozzles to avoid coalescence and interference of adjacent growing drops compared to conventional membranes. A second advantage of the micro-engineered nozzle plates is the low flow resistance through the nozzles due to the low thickness of the plates and the absence of thick support structures. In spite

of the low porosity, this results in higher dispersed phase fluxes compared to conventional membranes.

Stainless steel foils can be easily perforated in a desired way by laser ablation. We could show the capability of laser ablation to perforate metal foils and their use for emulsification. Further optimization of the drilling process and wet etching after the drilling would possibly increase the accuracy and quality of the fabricated nozzle plates. Laser ablation can also be performed on polymer foils and due to the development of infrared femtosecond lasers, Polytetrafluoroethylene (PTFE) and Polyethylene are now laser processable [1,2]. This opens the possibility to fabricate hydrophobic nozzle plates for water-in-oil emulsification.

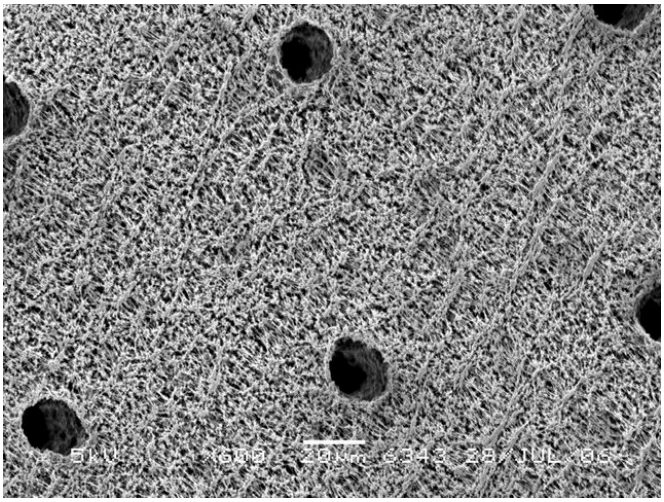

Figure 1: SEM-Image of holes in a commercial PTFE microfiltration membrane drilled by using a femtosecond laser.

We proved this by perforating a commercial PTFE microfiltration membrane (Millipore, FG, 0.22 μm) with a femtosecond laser. Figure 1 shows some of the drilled holes having a diameter on the laser beam entrance side of approximately 20 μm. Possibly, a further reduction of the diameter can be achieved by optimizing the drilling conditions and parameters.

Not only polymer foils can be processed but also polymer tubes or even polymeric hollow fiber membranes could be perforated. With perforated tubes or hollow fibers an emulsification module could be designed with multiple tubes aligned perpendicular to the flow of the continuous phase, as schematically drawn in Figure 2. The perforation itself is not restricted to circular shapes. Slit shaped or other non-circular shapes can also be drilled to promote the spontaneous drop formation process.

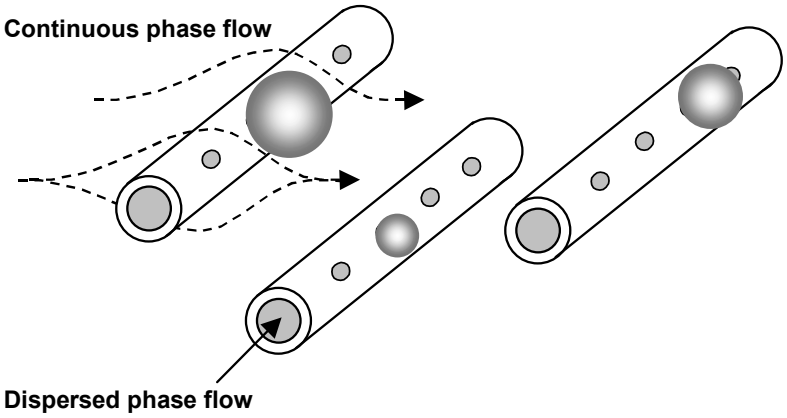

Figure 2: Schematic drawing of a multi tube emulsification module with laser-drilled holes.

To generate highly monodispersed emulsions with a single device, microchannel and straight-through microchannel emulsification are the most efficient processes. Here, drops are not released by shear forces. The so-called spontaneous drop formation process is based on Laplace pressure differences during the drop inflation. These differences are created by geometrical constraints in which the drops are inflated. Until now, this is the only device to generate highly monodispersed drops with relatively high production rates.

Most of the microchannel and straight-through microchannel emulsification studies were conducted with cleanroom-fabricated silicon based devices. In literature only stainless steel microchannels fabricated by dicing and polymeric microchannels formed by injection molding are reported [3,4]. Laser ablation and phase separation

micromolding are able to form these straight-through structures and they offer a wide range of processable materials (metals, ceramic and polymers).

The microfluidic chips, produced for the porous channel emulsification introduced in Chapter 7, can be further developed to chips with channels fully embedded in the porous polymer matrix. This avoids sealing problems and eases the fabrication. Three-channel chips made from PES and PEI solutions were fabricated using the same glass capillaries as used in Chapter 7. In Figure 3, three cross-sections of a PEI membrane with three fully embedded channels are depicted. Due to the polymer shrinkage in the normal direction, the channels have an elliptical shape as it can be seen in Figure 3A. The membrane has a thickness of half a millimeter. Figure 3B shows the embedding of the middle channel in the porous polymer matrix. The walls of the channels are porous as well as depicted in Figure 3C.

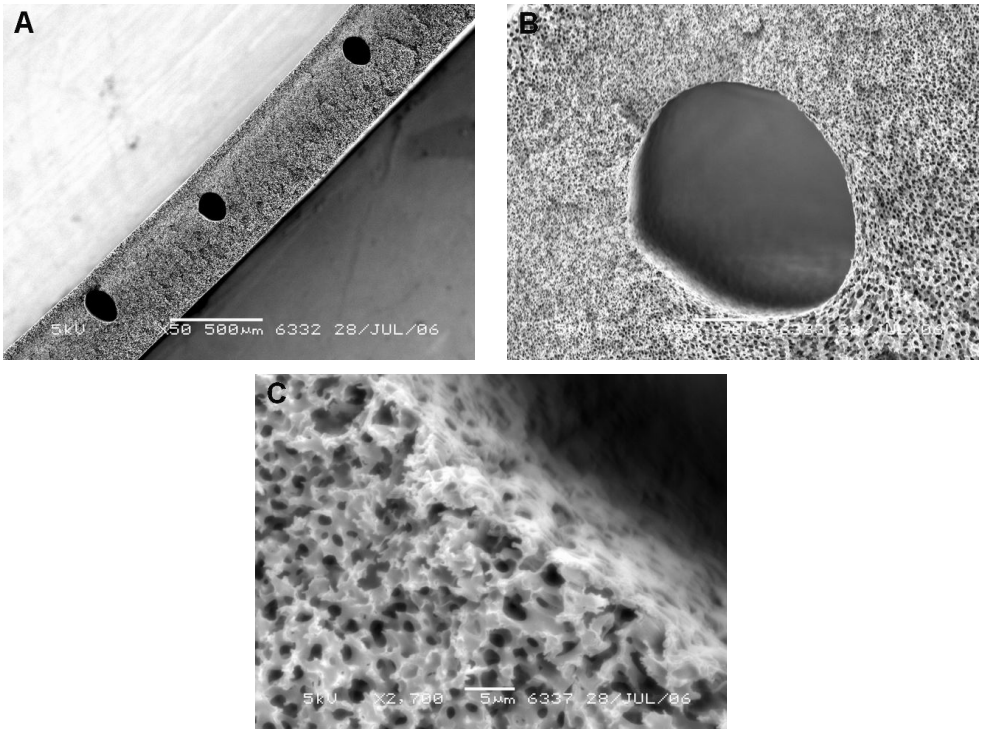

Figure 3: Cross-section SEM-Images of channels embedded in a porous PEI matrix.

The formation of drops was proved with a chip made from PES following the same procedures as reported in Chapter 7. Only the mold was different. Here, the glass capillaries were glued only at the ends with two slices of double sticky tape on to the glass plate, resulting in small gap between the capillaries and the glass plate. Figure 4 shows sunflower oil drops with an average diameter of 250 μm and a COV of 3 %.

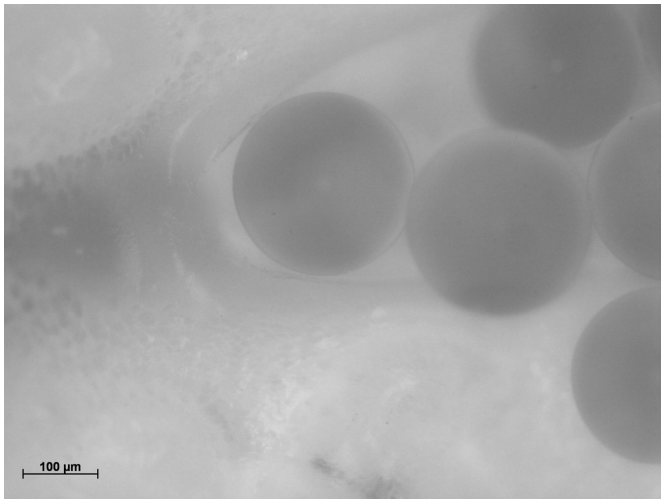

Figure 4: Sunflower oil drops emulsified in water by the porous channel emulsification using a microfluidic chip with fully embedded channels. The oil drops have just left the dispersed phase channel.

A multi channel chip design for high production rates is schematically drawn in Figure 5. Here, the embedded channels are fed all with the to be dispersed phase. The continuous phase is supplied from the top and bottom surface of the chip. Several of these chips can be stacked together to obtain a single device for high drop production rates. A critical issue is to generate an evenly distributed liquid supply for each dispersed phase channel and to fabricate a porous polymer matrix with a uniform permeability.

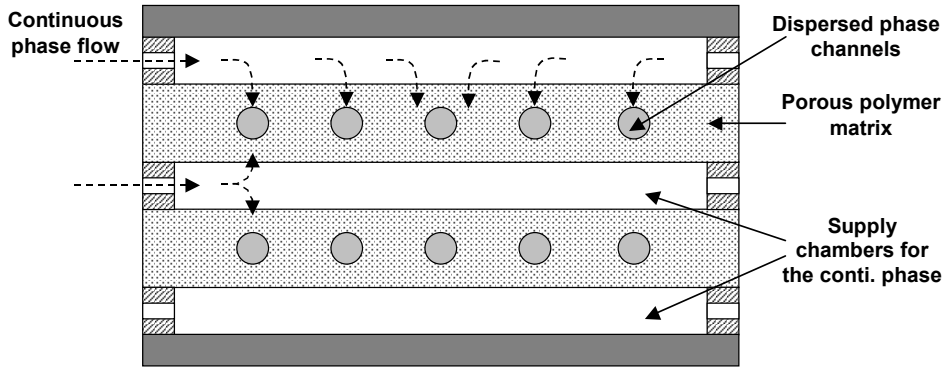

Figure 5: Schematic representation a of multi channel microfluidic chip device for higher drop production rates.

A new type of micro-nozzle plates is formed by silicon microtechnology and nickel electroplating resulting in nickel micro-chimneys as depicted in Figure 6. The electro deposited nickel film has a thickness of only a few micrometers.

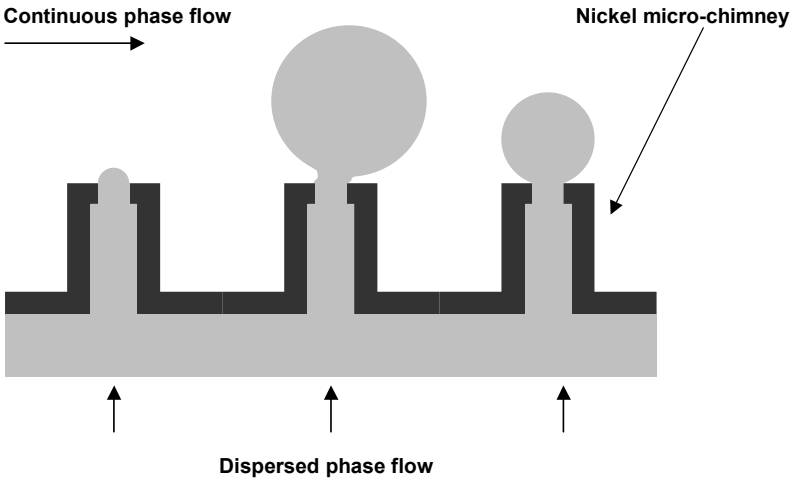

Figure 6: Schematic representation of the emulsification process with free standing micro-chimneys.

These micro-chimneys can be produced in different heights, diameters and shapes and therefore tunable to different process conditions. The purpose of the chimneys

is based on the idea that the edge of the chimney promotes the pinning of the three phase contact line (Liquid/Liquid/Soild). Therefore, the contact area is restricted to the top surface of the chimney and thus limiting the maximum interfacial tension force, which keeps the growing drop attached to the chimney. For a simple hole geometry in a flat surface the contact area can increase to a certain extent depending on the surface energy of the substrate (drop spreading). A limited interfacial tension force will lead to lower shear forces to detached a drop of a certain diameter from the chimney compared to nozzles in a flat surface.

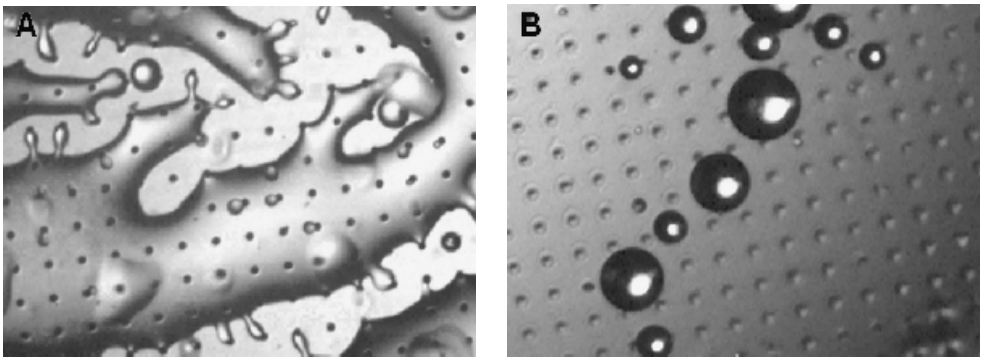

Figure 7: Emulsification of sunflower oil into water containing 1 wt% Tween 20 with a nickel micro-nozzle plate. Total spreading of the oil on an un-oxidized (A) and controlled oil drop formation with oxygen plasma treated Ni micro-nozzle plate (B).

As always, the wettability of the nickel surface has to be controlled. Emulsifying sunflower oil into water containing 1 wt% Tween20 with an untreated nickel micro-nozzle plate resulted in total spreading of the oil (Figure 7A). After a short oxygen plasma treatment the hydrophilicity of the nickel surface was improved and successful oil drop formation was achieved (Figure 7B). The hydrophobization of the nickel micro-nozzle plates according to silanization procedures used in this thesis for silicon nitride, steel and aluminum is possible as well. From literature it is known that oxidized nickel surfaces in combination with chemisorbed water forms surface hydroxyl groups [5], which are needed to covalently bond the used silanes to the surface.

8.4 Acknowledgements

The laser drilling was performed at the Laboratory of Mechanical Automation by Max N.W. Groenendijk (Applied Laser Technology, Department of Mechanical Engineering, University of Twente). The Nickel micro-nozzle plates were made by Laura D. Vargas Llona (Transducer Science and Technology, MESA+ Research Institute, University of Twente).

8.5 Abbreviations

COV	Coefficient of variations
FOTS	perfluorinated octyltrichlorosilane
OTS	Octyltrichlorosilane
PEI	Polyetherimide
PES	Polyethersulfone
PDMS	Polydimethylsiloxane
PTFE	Polytetrafluoroethylene
SDS	Sodium dodecylsulfate
SPEEK	sulfonated poly-ether-ether-ketone

8.6 References

[1] M. Womack, M. Vendam, P. Molian, Applied Surface Science 221 (2004) 99-109

[2] M. Okoshi, N. Inoue, Applied Physics A 79 (2004) 841-844

[3] J. Tong, M. Nakajima, H. Nabetani, Y. Kikuchi, Y. Maruta, J. Colloid Interface Sci. 237 (2001) 239-248

[4] H. Liu, M. Nakajima, T. Nishi, T. Kimura, Eur. J. Lipid Sci. Technol. 107 (2005) 481-487

[5] H. Guo, F. Zaera, Catalysis Letters 88 (2003) 95-104

Summary

This thesis deals with the formation of emulsions using micro-engineered devices. It covers devices made from silicon nitride, metals and polymers using different types of micro-processing tools for their fabrication. In order to produce water-in-oil emulsions, surface modifications were applied to render the surface of the metal and silicon nitride devices hydrophobic.

The first part of the thesis is dedicated to silicon nitride micro-nozzle plates used to emulsify water into oil. These nozzle plates have precisely defined pore sizes and pore-to-pore distances, fabricated by use of photolithographic and etching techniques. To generate water-in-oil emulsions the surface of silicon nitride has to be hydrophobized. In Chapter 2 different kinds of hydrophobic coatings, namely alkylsilane monolayers, plasma and dip-coated polydimethylsiloxane, are researched considering the thermal and chemical stability according to cleaning procedures used in the food industry. It was found, that the most stable one is a perfluorinated alkylsilane monolayer.

In Chapter 3, the surface energy and the wetting behavior of the mentioned coatings is discussed. The best coating, showing the highest water/hexadecane contact angle, is a coating, which has a high affinity to the continuous phase (hexadecane) and a low affinity to the dispersed phase (water). Here, an alkylsilane monolayer showed the highest water/hexadecane contact angle because of its chemical similarity to hexadecane. The measured water/hexadecane contact angles on several substrates showed a poor agreement with Youngs equation. This was explained by a stable and thin layer of hexadecane between the water and the substrates and proved theoretically by calculating the Hamaker constants of the different liquid/liquid/solid systems. In emulsifier containing systems the observed dynamic wetting behavior showed only in case of the perfluorinated alkylsilane monolayer a negative influence of the used emulsifier. In general, all observed changes of the wetting behavior on the tested substrates were rather slow compared to the usual drop formation time during emulsification.

For alkylsilane coated silicon nitride nozzle plates successful emulsification of water into hexadecane could be demonstrated. The good performance of the

hydrophobized nozzle plates was displayed by a high number of active pores (60-100 percent) and a high dispersed phase throughput (up to 4600 L h^{-1} m^{-2} bar^{-1}) at less than two times the critical pressure. Due to the relatively low cross-flow velocity the formed drops were 100 to 200 μm in diameter. The size variation ranged between 5 and 25 percent depending on the nozzle activity. A pressure dependent period of inactivity between two formed drops from a single nozzle was observed. This lag time is related to the slow adsorption kinetics of the used emulsifiers BolecMT and Span85.

In chapter 5 the emulsification with laser-drilled metal nozzle plates made from stainless steel and aluminum with nozzle diameters down to 4.4 μm is discussed. These nozzle plates were used for water-in-oil and oil-in-water emulsification. Compared to the silicon nitride nozzle plates, these plates had wider nozzle diameter distributions and less controlled nozzle shapes. Due to the deviation from the circular nozzle shape, spontaneous formed drops could be observed at some of the nozzles, which were 2.3 to 4.7 times larger than the hydraulic diameter of the nozzles. Depending on the process conditions, the shear-induced drops were 16 to 35 times larger than the hydraulic diameter of the used nozzles and had variations of the diameter between 7 and 24 percent. Here as well, a lag time during the water-in-oil emulsification using Span85 was observed. Also within emulsifying oil into water using the surfactant Tween20 a lag time was found.

The formation of polymeric micro nozzle plates using the phase separation micromolding technique and their use for oil-in-water emulsification was investigated in chapter 6. The starting point for the preparation of the polymeric nozzle plates was a standard recipe based on polyethersulfone for making polymeric microsieves for filtration applications. It was found, that changing the mold structure implies recipe optimization and adjustments of phase separation conditions. Therefore, the standard recipe was changed in order to obtain defect free and fully perforated films. The best results were achieved using a blend of polyethersulfone (PES) and sulfonated poly-ether-ether-ketone (SPEEK). The obtained micro nozzle plate had nozzle diameters of approximately 5 μm, it was defect free, almost fully perforated and showed nearly undeformed nozzles. After an additional surface oxidation using an oxygen plasma treatment, successful emulsification of sunflower oil into a 1 wt%

Tween20 aqueous solution could be performed. The formed drops had an average diameter of 68 μm and the coefficient of variation was ranging between 16 and 22 percent.

A new emulsification method is presented in chapter 7 using a porous microfluidic chip fabricated from polyethersulfone und polyimide via phase separation micromolding. The mold exhibited a structure of parallel-aligned capillaries, which were replicated as round channels embedded in the porous polymer matrix. Due to a transparent sealing layer, the drop formation could be optically observed and studied. The oil drop formation was identified to be similar compared to the dripping mode reported for flow-focusing devices. The formed oil drops were approximately 1.2 times larger than the channel diameter of 160 μm. They showed a narrow drop size distribution with a coefficient of variation of below 3 percent.

Zusammenfassung

Die vorliegende Dissertation beschäftigt sich mit der Herstellung von Emulsionen mit Hilfe von Mikroloch- und Mikrokanalstrukturen. Die Lochstrukturen, im weiteren Mikrolochplatten genannt, wurden über verschiedene Mikrostrukturierungsverfahren hergestellt. Die Fabrikation von Siliziumnitrid Mikrolochplatten erfolgte über sogenannte Reinraumtechniken (Fotolithographie und Ätzverfahren). In Metallfolien wurden Mikrolöcher mit Hilfe eines Femtosekundenlasers gebohrt. Durch Mikroabformung bei gleichzeitiger Phaseninversion einer Polymerlösung wurden polymere Mikrolochplatten und Mikrokanäle hergestellt.

Die Emulgierung von Wasser in Öl durch metallische und keramische Mikrolochplatten erfordert eine Hydrophobisierung der Oberflächen. Ein Teil dieser Dissertation beschäftigt sich deshalb mit verschiedenen Strategien zur Hydrophobisierung von Siliziumnitrid. Untersucht wurden selbstorganisierende, monomolekulare Schichten aus Kohlenwasserstoffsilanen, plasmapolymerisierte und tauchbeschichtete Silikonbeschichtungen. Die einzelnen Beschichtungen wurden hinsichtlich ihrer Benetzungseigenschaften, Oberflächenenergien und chemisch-thermischen Stabilität untersucht. Es zeigte sich, dass fluorierte Alkylsilanschichten die beste chemische und thermische Stabilität in sauren und basischen Umgebungen besitzen.

Durch die Bestimmung der Oberflächenenergien der Beschichtungen sowie der Grenzflächenspannungen zwischen den Beschichtungen und den Flüssigkeiten Wasser und Hexadekan konnte gezeigt werden, dass die optimale hydrophobe Beschichtung für die Emulgierung von Wasser in Öl eine hohe Affinität zum Öl und eine geringe zum Wasser aufweisen sollte. Nur so können hohe Wasser/Öl Kontaktwinkel realisiert werden. In der vorliegenden Dissertation wurden die höchsten Wasser/Öl Kontaktwinkel auf einer Alkylsilanschicht gemessen.

Die auf den verschiedenen Beschichtungen gemessenen Wasser/Öl Kontaktwinkel zeigten eine signifikante Abweichung von der Youngschen Benetzungtheorie. Dies konnte durch das Vorhandensein eines dünnen Hexadekanfilms zwischen den Wassertropfen und den Beschichtungen theoretisch anhand von negativen

Hamaker Konstanten der betreffenden Dreiphasensysteme (Wasser/Hexadekan/Beschichtung) erklärt werden.

Die Beeinflussung der Benetzungseigenschaften durch Emulgatoren wurde ebenfalls untersucht. Es konnte gezeigt werden, dass alle zeitlichen Veränderungen, in der Mehrzahl eine Erhöhung der Kontaktwinkel, für die Emulgierung vernachlässigbar sind, da diese Veränderungen erst nach mehreren Minuten auftraten, und damit wesentlich langsamer sind als die Tropfenbildungszeit während der Emulgierung. Diese Vernachlässigung hat aber nur Gültigkeit sofern die Adsorptionsgeschwindigkeit der verwendeten Emulgatoren gering ist.

Die Emulgierung von Wasser in Öl durch hydrophobisierte Siliziumnitrid Lochplatten zeichnete sich durch eine hohe Anzahl von aktiven Poren (60-100 Prozent) und einen Wasserdurchsatz von bis zu 4600 L h^{-1} m^{-2} bar^{-1} bei relativ geringen Emulgierdrücken aus. Die Tropfendurchmesser zeigten hier keine Abhängigkeit vom angelegtem Emulgierdruck. Dies wird der geringen Adsorptionsgeschwindigkeit der verwendeten Emulgatoren zugeschrieben. Eine weitere Auswirkung der geringen Adsorptionsgeschwindigkeit ist das Auftreten einer diskontinuierlichen Tropfenbildung. Zwischen den einzelnen Tropfenbildungen an einem Mikroloch trat eine Periode der Inaktivität auf, die in direkter Relation mit dem anglegtem Druck steht. Mit steigendem Druck verringert sich diese zeitliche Inaktiviät bis eine kontinuierliche Tropfenbildung erreicht wird. Für einen der untersuchten Emulgatoren konnte eine direkte Verbindung zwischen der zeitlichen Inaktivität und der dynamischen Grenzflächenspannung aufgezeigt werden.

Durch die Lasermikrobearbeitung von Aluminium und Edelstahlfolien konnten Mikrolochplatten mit Lochdurchmessern von minimal 4,4 μm reproduzierbar hergestellt werden. Eine erfolgreiche Hydrophobisierung durch Alkysilane konnte auf Aluminium und Edelstahl erreicht werden. Mit diesen metalischen Mikrolochplatten wurden Wasser-in-Öl als auch Öl-in-Wasser Emulgierungen durchgeführt. Wie im Falle der Siliziumnitrid Lochplatten, wurden auch hier hohe Wasser- bzw. Öldurchsätze bei geringen Drücken erzielt. Ebenfalls wurde die Tropfenbildungsinaktivität für zwei unterschiedliche Emulgatoren beobachtet.

Bei der Herstellung von polymeren Mikrolochplatten auf Basis der Phaseninversion von Polymerlösungen zeigte sich, dass die Herstellung von defekt freien und

vollständig perforierten Lochplatten stark von der Struktur der Abformvorlage, der Zusammensetzung der Polymerlösung und den Phaseninversionsbedingungen abhängig ist. Deshalb kann jede Veränderungen innerhalb dieser zu einer erneuten Anpassung und Optimierung des Herstellungsprozesses führen. Die hier hergestellten und untersuchten Polyethersulfon Mikrolochplatten konnten erst nach Zusatz eines hydrophilen, polymeren Additives und einer Oberflächenbehandlung in einem Sauerstoffplasma erfolgreich für die Emulgierung von Öl-in-Wasser eingesetzt werden.

Die Erzeugung von monodispersen Öl-inWasser Emulsionen konnte durch die Entwicklung einer Mikrokanal-Emulgiereinheit erzielt werden. Hierbei wurde die Abformung der Mikrokanäle ebenfalls über die Phaseninversion einer Polymerlösung auf einer selbst hergestellten Vorlage durchgeführt. Die so in der polymeren Matrix abgeformten Kanäle hatten einen Durchmesser von 160 μm und eine poröse und wasserdurchgänige Oberfläche. Zur optischen Beobachtung des Tropfenbildungsvorganges wurden die Kanäle mit einer transparenten Folie abgedichtet. Somit konnte die Bildung von monodispersen Öltropfen in Wasser innerhalb eines Kanals verfolgt werden. Die Tropfenbildung zeigte Ähnlichkeiten zur Bildung von Flüssigkeitstropfen beim Abtropfen von einer Kapillaren. Die so erzeugten Öltropfen hatten einen Durchmesser, der in etwa dem 1,2 fachen des Kanaldurchmessers entsprach, und eine Variation des Durchmesser von kleiner 3 Prozent.

Danksagung

Now, the work is done and I have finished my Ph.D. Thesis. In the last four years, I have counted thousands of drops and I made hundreds of drop pictures. Therefore, I can say that: “It is all about drops”.

Remembering how it started four and a half years ago, I want to thank first of all Matthias for giving me the opportunity and the challenge to make my Ph.D. Thesis within the famous Membrane Technology Group at the University of Twente and my former boss Josef from the Fraunhofer Institute UMSICHT (Oberhausen, Germany). He had the connection to this well known research group. At second, I would like say thank you to my German colleagues and friends Kirsten, Sandra, Asja, Ilka, Martin, Markus, Dirk and Maruan, which encourage me to go to the Netherlands (Holland -like the Germans say) for a Ph.D. study.

In these four years, I had two supervisors, namely Zandrie and Rob. In the beginning, Zandrie helped me a lot with his emulsification experiences to get into the topic. Nearly half way, Rob took over the supervision. With the help of his knowledge about surface and interface science many new ideas were born and I’m very grateful for his editing work, comments and ideas during the writing period, which improved this thesis to a great extend. Rob and Zandrie, it was pleasure for me and dank je well voor het geode samenwerken.

In the beginning, there was another important and extremely helpful member of the Membrane Technology Group, who helped me with all the paper work and organized a nice room in the pyramids at Witbreuksweg for me. This person was also always helping and dealing with various kinds of paper work and administrative problems during the four years. Thanks a lot Greet!

I would like to thank Lydia, Erik, Hermann, Marcel and John for their help, whenever I was facing problems with laboratory equipment or computers and Jörg for solving all the electrical problems I had.

Without the time Max Groenendijk spent with laser drilling of holes into various kinds of substrates one part of thesis would not be realized. Thanks Max!

A Ph.D. thesis is not imaginable without the helping hands of students. Therefore, I like to acknowledge Thomas for his work on the stability of the silane monolayers, Jun Liu for producing dip-coated PDMS coatings, and Christina and Nienke for getting the porous channel emulsification working. Thank to all of you for being hard and enthusiastic working students.

Part of this work was carried out under the framework of the Thames Project (QRLT 2000-01228). I like to thank all the project partners for the nice and fruitful cooperation and Jo Jansen for his excellent project coordination.

In four years it tends to happen that one has to change the office once in a while. It happened to me as well. First I shared the office with Miriam and Jörg and after we were kick-out of this office, I moved into one of the famous “Chicken Boxes”, which I shared with Joao known as the “bloody Portuguese bastard”. I hope that Miriam and Jörg enjoyed the “stupid” conversations Joao and I had, which they had to listen to through the extremely thin walls between the two “Chicken Boxes”. Thanks for your nice company.

Another group of people I like to acknowledge for making the life at Langezijds really enjoyable is the “smoker gang”. Thanks to Jens, Jutta, Hakan, Katja, Matias (core members) and all of you, who participated once in a while, for all the funny, sometimes stupid but also serious and scientific conversations during the coffee breaks. By the way the smokers were mostly in the minority.

Being a member of the Membrane Technology Group is connected with many sportive and social events. Playing football on Fridays, running the Bata Race, riding once a year with the bicycle through the neighborhood of Enschede, joining the Picture of the Month competition in the Geus, having some beers at the Friday after work borrels and traveling around Europe. Thanks to all who joined and organized these events. This makes the Membrane Technology Group to a research group, where one can really enjoy the scientific life.

Last but not least, I would like to thank my family and friends for always supporting and encouraging me through the years of studying, working and finally writing a Ph.D. thesis. Vielen, vielen, vielen Dank für alles.

Curriculum Vitae

Maik Jörn Geerken was born on 24th of May 1974 in Wilhelmshaven (Germany). He finished the high school in 1993 and started studying chemical engineering at the University of applied science Ostfriesland (Emden, Germany). In 1999 he finalized his study with a Diploma work about the use of membrane technology in diary industry. After the graduation he was employed at the Fraunhofer Institute for environmental, safety and energy technology (Oberhausen, Germany) as a researcher within the membrane technology division. In 2002 he started halftime as a Ph.D. student at the University of Twente (UT) and continued halftime working at the Fraunhofer Institute. After two years he fully joined the Membrane Technology Group at the UT and finished his Ph.D. work in June 2006. Since July 2006 he works at the European Membrane Institute associated to Membrane Technology Group as a Postdoc.